# University of Southampton Research Repository

Thesis: Sahar Mirzaei (2018) "Metamaterial-based sensor", University of Southampton, faculty of physical sciences and engineering, school of electronics and computer science, PhD Thesis, pagination.

Data: Sahar Mirzaei (2018) Metamaterial-based sensor. URI [dataset]

# UNIVERSITY OF SOUTHAMPTON

FACULTY OF PHYSICAL SCIENCES AND ENGINEERING

SCHOOL OF ELECTRONICS AND COMPUTER SCIENCE

# METAMATERIAL-BASED SENSORS

by

Sahar Mirzaei

Thesis for the degree of Doctor of Philosophy

March 2018

**UNIVERSITY OF SOUTHAMPTON**

# ABSTRACT

FACULTY OF PHYSICAL SCIENCES AND ENGINEERING

School of Electronics and Computer Science

Thesis for the degree of Doctor of Philosophy

**METAMATERIAL-BASED SENSORS**

Sahar Mirzaei

In genetic diagnostics, analysis is mostly based on fluorescent labelling of target DNA molecule and sequences. The process of labelling can alter DNA strands, is not always specific enough to make gene detection sufficiently precise and is time consuming and expensive. For Point-of-Care or benchtop diagnostics, there is a technological requirement for reading the labels, again slowing down the process and making devices more complex and expensive. To get around these shortages, this study introduces a label-free detection technique using metamaterials.

Metamaterials are synthetic composite materials, engineered to have electromagnetic properties that do not occur in nature. Metamaterials can demonstrate resonant behaviours and localize the electromagnetic field. This can be used to improve the sensitivity of surface based sensors, which respond to refractive index changes in the deposited material. In addition, the metamaterials allow for tunability of the resonant frequency, so that sensors can be targeted to specific responses, such as the THz sensitivity of DNA. This work focuses on the designs and fabrication of metamaterial structures for the purpose of sensing. The metamaterial inclusions are micrometre scale X-shaped resonators, each on a 220×220 $\mu$m square base, tuned to produce trapped-mode resonance in terahertz (THz) regime (0.4-1.2THz) to detect backbone resonances of DNA which occur in this region.

Research indicates that modification of asymmetry in the shape of resonators, causes them to resonate at two different frequencies close to one another, the trapped mode in between the two gives a sharp notch with a high quality factor (Q-factor), ideal for sensing purposes. The Q-factor of the trapped-mode resonance produced using this metamaterial is shown to be higher than the previously proposed metamaterial-based biosensors investigated by other researchers.

The fabricated metamaterials show a good agreement between the simulated and measured results. Also, fabrication results show that by adding an analyte, layered up on top of the metamaterial inclusions, the sensitivity of the structure can be calculated by examining the change in the trapped-mode resonance frequency, where a shift in the peak of resonance is observed and quantified.

# Table of Contents

# List of Tables

# List of Figures

# Glossary of Acronyms

Decibel (dB)

Cyclic Olefin Copolymer (COC)

Deoxyribonucleic acid (DNA)

De-Ionised (DI)

Electromagnetic (EM)

Fast Fourier Transform (FFT)

Finite Integration Technique (FIT)

Isopropyl Alcohol (IPA)

Microelectromechanical systems (MEMS)

Nanoelectromechanical systems (NEMS)

Printed Circuit Board (PCB)

Poly Methyl Methacrylate (PMMA)

Polyadenylic Acid (Poly-A)

Polycytidylic Acid (Poly-C)

Quality Factor (Q-Factor)

Ribonucleic acid (RNA)

Signal to Noise Ratio (SNR)

Split Ring Resonator (SRR)

Transverse Electromagnetic Wave (TEM)

Terahertz (THz)

Terahertz Time Domain Spectroscopy (THz-TDS)

Ultra Violet (UV)

# Academic Thesis: Declaration Of Authorship

I, Sahar Mirzaei declare that this thesis and the work presented in it are my own and has been generated by me as the result of my own original research.

**METAMATERIAL BASED SENSORS**

I confirm that:

1. This work was done wholly or mainly while in candidature for a research degree at this University;
2. Where any part of this thesis has previously been submitted for a degree or any other qualification at this University or any other institution, this has been clearly stated;
3. Where I have consulted the published work of others, this is always clearly attributed;
4. Where I have quoted from the work of others, the source is always given. With the exception of such quotations, this thesis is entirely my own work;
5. I have acknowledged all main sources of help;
6. Where the thesis is based on work done by myself jointly with others, I have made clear exactly what was done by others and what I have contributed myself;
7. Parts of this work have been published as:

**Mirzaei, Sahar**, Nicolas G. Green, Mihai Rotaru, and Suan Hui Pu. "Detecting and identifying DNA via the THz backbone frequency using a metamaterial-based label-free biosensor." In *Terahertz, RF, Millimetre, and Submillimetre-Wave Technology and Applications X*, vol. 10103, p. 101031I. International Society for Optics and Photonics, 2017

**Mirzaei, Sahar**, Nicolas G. Green, Mihai Rotaru, and Suan Hui Pu. “Improving the sensitivity of metamaterial-based THz biosensors, by using X-shaped resonators, *In preparation*

Signed: ..........................................................................................................................

Date: ..........................................................................................................................

# Acknowledgements

I would like to express my genuine appreciation towards my supervisors Dr Mihai Rotaru, Dr Nicolas Green and Dr Suan Hui Pu for believing in me and granting me the chance to work on this project, for the regular meetings and sharing of their knowledge, and for their guidance throughout this candidature.

Thanks also to Dr Mehdi Banakar and Dr Kian Shen Kiang for sharing their knowledge and guiding me throughout the fabrication process.

I would also like to thank, Dr Vasilis Apostolopoulos and his team, especially Jon Gorecki and Elena Perivolari in THz group, University of Southampton, for kindly carrying out the THz-TDS measurements.

I would like to thank all my PhD colleagues; with whom I have shared moments of deep anxiety but also of big excitement. A kind word for Dr Mehdi Banakar, Dr Nikolaos Matthaiakakis, Dr Benjamin lowe, Dr Christoph Riedel, Dr Jack Nonofu, and Katarzyna Grabska, to name a few.

Also, special gratitude to my **friends** for their presence and support in a process that is often felt as tremendously solitaire, especially Dr Fatemeh Tahavori.

I cannot thank my dear husband enough for his patience and encouragement during my candidature.

And lastly, I would like to thank, my parents and my brother, without whom I would not be where I am today.

# Chapter 1 **Introduction**

Biosensors are vital for disease diagnostics, investigation of biological phenomena, environmental monitoring, food safety, and so on. In biosensing, the stimulus is usually a biomaterial that interacts with the sensitive element of the sensor. This interaction can be picked up by a detector. The difference between biosensors is in the fashion that the detection takes place, either by labelling (e.g. chemical binding) or label-free (e.g. optical reading) detection [1, 2].

One of the prominent subjects of study in biotechnology is DNA and genetic testing, such as detecting changes in DNA chains [3], for early diagnosis of various diseases. Currently, DNA analysis and gene detection is mostly based on fluorescent labelling of the targeted DNA molecule [4].

Although fluorescent labelling is largely used and has been advanced in the recent years, labelling can alter the DNA strands, leading to fluctuations which make the gene detection less precise. Also, fluorescent-based biosensors, often call for lengthy sample preparations and outcome detections. Accordingly, for genetic diagnostics, the development of bench-top biosensors proves essential [3].

Researchers constantly work to advance the characteristics of DNA analysers to achieve a larger degree of flexibility, rapidity, and cost-effectiveness. One of the methods to make DNA analysis faster is Label-free detection.

Predictions from theoretical studies [5, 6], as well as measurements through terahertz spectroscopy [7] show several natural resonances within DNA backbones in the THz region (0.4 to 1.2 THz). This introduces the possibility to utilise these natural resonances for label-free detection of DNA binding state.

Label-free DNA detection is a fairly less investigated method, some studies have investigated the possibility of using split ring resonators (SSRs) [8-16] as label-free biosensors. Basically, SRRs can be modelled as LC circuits with the associated resonant frequency. The shift in the resonant frequency is observed after adding the analyte to the structure, this shift can be attributed to the change of the capacitance of the equivalent LC circuit and subsequently the change in the dielectric properties of the model, after adding the analyte.

## 1.1 Motivation

Resonant behaviour of planar metamaterials can be utilised to improve the sensitivity of surface based sensors, which respond to refractive index changes of the deposited material. In addition, the metamaterials allow for tunablity of the resonant frequency, so that sensors can be targeted to specific responses, such as the THz sensitivity of DNA.

The concept of using planar metamaterials for label-free microorganism detection in THz is relatively new, around a decade old, and there are a lot of possibilities to improve the current sensors which suffer from lack of reliability due to low quality factors [14-18]. To improve the sensitivity of planar metamaterial-based sensors, and to achieve a higher degree of selectivity, the resonance peak produced by the metamaterial must have a relatively high quality factor. This way, when an analyte is added to the sensor, the shift of the resonance peak in the frequency response would be easier to observe, and identifying different analytes based on the shift of the resonance peak would be more reliable.

To achieve this, metamaterial inclusions which are conventionally SRRs can be replaced by new structures that produce a narrower resonance peak compared to SRRs. Also, to achieve a clear resonant response, only associated with the resonant behaviour of the metamaterial, a substrate more transparent to THz must be used rather than silica which is usually the substrate of choice [10, 19] for these type of sensors and is not completely transparent in THz.

Consequently, label-based biosensors can be replaced, by label-free sensors that are as sensitive and reliable as conventional sensors but also are more user friendly, cheaper to operate and less time consuming.

*Rotaru et al.* [20] have successfully shown through simulations, that by using X-shaped resonators as opposed to SRRs, for metamaterial inclusions, high quality factor resonances can be achieved to detect the shift of resonance in the frequency response.

In this study, carrying on with *Rotaru et al*'s [20] research, the possibility of detecting and identifying the backbone resonances of DNA using metamaterial-based sensors is investigated. With the aim to advance the label-free detection in THz region by using metamaterials with higher quality factors than the ones readily available. By achieving this, a higher selectivity of the shift in the resonance frequency is accessible when a substance is added to the sensor.

## 1.2 Primary contribution of this study

The main contributions of this study can be summarised as:

- Improving the selectivity of label-free metamaterial-based sensors by introducing an X-shaped resonator for the metamaterial inclusions compared to conventionally used split ring resonator
- Proving the ability of the metamaterials with X-resonators to act as sensors, by showing the agreement of the experimental results with the simulation data
- Determining the type of analyte added to the sensor by observing the shift in the resonant frequency of the metamaterial.

This study can be advanced to ideally produce a metamaterial-based sensor that can replace the conventional label-based fluorescent DNA detection.

## 1.3 Outline of the Thesis

Chapter 2, covers the literature review, giving an insight on the history of biosensing, and the advantages and disadvantages of current state of the art.

Chapter 3 is about the fundamental of computational electromagnetics, followed by Chapter 4, which covers the basics of the THz time domain spectroscopy.

In Chapter 5, the simulation of the metamaterial is discussed, discussing how different shapes of the X-resonator can affect the frequency response and the trapped-mode resonance. And subsequently, choosing four different inclusion designs for fabrication. Followed by finding a suitable substrate for the metamaterial inclusions in the THz region, which would not attenuate the frequency response of the model.

In Chapter 6, the steps taken for fabricating the metamaterial and how the fabrication process is perfected is explained. Next, in Chapter 7, the frequency response of the fabricated metamaterials is presented and the results of the THZ-TDS measurements are detailed.

Chapter 8, concentrates on the sensing aspect of the metamaterial, where the simulated result of sensing different RNA samples is compared. Followed by a comparison between the loaded and unloaded sensor responses. To load the sensors a photoresist analyte is added to the fabricated metamaterial. The results are measured by THZ-TDS, and compared to the frequency response of the metamaterials before adding the analyte sample.

And lastly, Chapter 9 covers the conclusion to the thesis and giving an insight the possible future work.

# Chapter 2 **Literature review**

The passion of producing sensors with the ability to measure properties of biological substrates started in the middle of 20th century by *Leland C. Clark Jr*. [21] who is known as the father of biosensors for his ground-breaking developments for the heart-lung machine. Since then, various biosensors have been developed by researchers all around the world. Biosensors come in different forms and shapes, from the basic Glucose monitors all the way to the complicated cell analysers.

One of the main target analytes for biosensors is Deoxyribonucleic acid (DNA), which is the analyte of interest in this study.

## 2.1 Deoxyribonucleic acid (DNA)

DNA is a three-dimensional molecule with a double helix structure enclosing genetic features of the host. The double helix is supercoiled, made up of two individual strands known as (msDNA). Each strand is shaped as a twisted ladder with each rung formed of two nucleotides bolted to one another, adenine to thymine and cytosine to guanine. The structure linking the rungs together is called the DNA backbone. DNA backbones are based on a repeated pattern of sugar (deoxyribose) and phosphate groups [22], Figure 2-1.

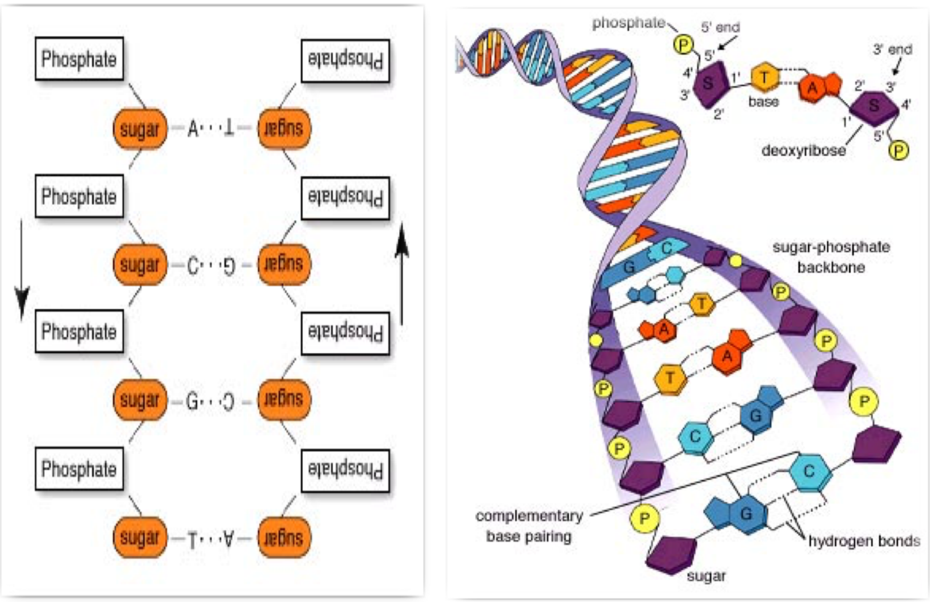

Figure 2-1 the backbone structure of a DNA molecule, made up of sugar (deoxyribose) and phosphate groups (left). The DNA molecule structure is made of the linkage of nucleotides to each other, adenine to thymine and cytosine to guanine (right) [23]

DNA, having a bendable nature, can embrace different shapes and formats such as A, B, C, D and Z-DNA. The forms differ in the length, handedness (helix rotation), the difference in the size of spaces between nucleotides and also the number of nucleotides in each turn. Each form, having a particular structural characteristic, is distinct from the others. [24] The most common type of DNA is B-DNA, found in human body and living cells.

## 2.2 Label-based detection

Currently, DNA analysis and gene detection is mostly based on fluorescent labelling of the targeted DNA molecule [4]. Although fluorescent labelling is largely used and has been advanced in the recent years, labelling can alter the DNA strands, causing fluctuations which leads to inaccurate gene detection.

Labelling not only adds an unnecessary pre-step to the process which slows down the detection progress but also adds additionally required label identifying steps; also, the technological requirement for optically reading of the labels makes these devices more complex. The disadvantages of label-based biosensors prove a necessity for development of accurate label-free biosensors [3].

## 2.3 Label-free biosensors

The label-free biosensing can be achieved by identifying the molecular composition of a bio-analyte through sensing the dielectric properties in a target frequency range [25, 26]. For larger biomolecules, like DNA, the dielectric changes within the binding state of the biomolecule are used for detection [27].

Calculations by *Van Zandt et al.* show that there are several resonances in excited backbones of DNA molecules associated with THz region [5, 6]. The occurrence of these resonances in THz region points out the possibility of exploiting THz measurements as a label-free detection method for binding states of DNA molecule, which can lead to detect the presence of genes through matching the results to pre-calculated data [3]. Studies show that DNA structural changes affect its low frequency vibrations (0-250 $cm^{-1}$, which covers THz range), so different forms of DNA in macromolecular level have different vibrational modes [28]. This knowledge can be used to distinguish between different forms of DNA through the difference in their resonance modes.

*Brucherseifer et al.*[29] and *Bolivar et al*. [30] have introduced a label-free detection method for the binding state of DNA by demonstrating the complex refractive index of DNA in THz region. The method seems promising but it requires a large amount of DNA present in the sample to return consistent outcome.

In the biosensing field, one of the main challenges is to be able to achieve high sensitivity and selectivity with the smallest amount of analyte, even as far as single cell detection [31].

To enhance the detection limit, one can place the DNA sample directly on the chip where THz signals are generated and detected, thereby increasing the interaction between the signal and the analyte, since the signal can be directed through the plane of the sample layer (even if very thin) [32].

For this type of label-free biosensing the natural resonance of the analyte is detected using a resonating structure. Most of these resonating structures are too small in size, resulting in inability to concentrate the field. Subsequently, most of the electromagnetic radiation will dissipate into the free space. Additionally, the structure, being too small, cannot provide the minimum space for the wave to scatter in (due to the fact that the structure is smaller than the wavelength of the incident electromagnetic wave).

In contrary, metamaterials show the possibility to sense even the smallest volumes of the analyte [33]. Metamaterials also enhance the localization of electric and magnetic fields in sensors, behaving as if they were much larger than their actual size, without causing great loss of power.

Label-free DNA detection through utilizing metamaterials can also overcome the labour intensive steps associated with conventional DNA sensing methods by enhancing the sensitivity and selectivity and by shortening the whole process, saving time and money.

For label-free DNA detection [34], the shift in the frequency response can be observed using the strong localization of metamaterials operating in the terahertz region of the electromagnetic spectrum.

## 2.4 Sensitivity of Label-free biosensors

Sensitivity of a Label-free biosensors depends on different characteristics of the device, such as, particle aspect ratio, surrounding environment, material, composition and configuration, etc. Also, the sensitivity of a device is affected by the resonance frequency of the resonator; the sensitivity becomes higher at the resonant frequency and less accurate in other frequency ranges.

In principal, the sensitivity of a sensor depends on changes in the surrounding environment. By changing the neighbouring materials of the sensor the refractive index changes. So, another way of enhancing the sensitivity to dielectric changes is by having a refractive index close to critical angle of the total reflection [35]. Ultimately, the sensitivity can be increased by

- Putting the analyte directly on the chip [32]
- Refractive index close to the critical angle of refraction [35]
- The resonance frequency of the sensor (functioning range) close to that of the analyte [16]

The sensitivity of a specific biosensor can be linked to the quality factor (Equation 2-1) of the resonant frequency [16], which is the method commonly picked by researchers to evaluate the sensitivity of metamaterial-based sensors [17, 18].

$$Q_{factor} = \frac{f_0}{\Delta f} \qquad 2\text{-}1$$

If a resonator has a narrower peak at 3 dBs at the resonant frequency in comparison to the other resonators, the selectivity for the model with the narrower peak is higher; this selectivity is evaluated by the quality factor of the system, (Figure 2-2).

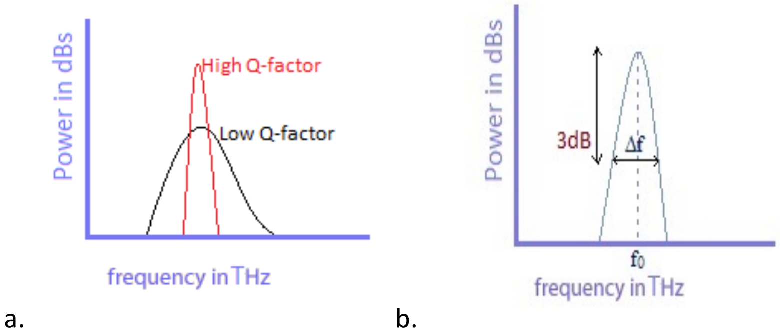

a.

b.

Figure 2-2 (a.) The quality factor for spiky and narrow curves is higher because the $(\frac{f_0}{\Delta f})$ is larger for slimmer curves. So in this figure, the red curve has a higher Q-factor in comparison to the black one. (b.) The diagram shows that $f_0$ is the maximum frequency response and $\Delta f$ is the bandwidth of power curve at 3dB of the resonant peak (half power). Quality factor is then obtained using $Q = \frac{f_0}{\Delta f}$, which gives the ability of comparing curves.

The resonant frequency is given by

$$f_0 = \frac{c}{2L\sqrt{\varepsilon_r}} \tag{2-2}$$

, where $c$ is the speed of light in the free space, $\varepsilon_r$ is the permittivity of the material and L is the length of the resonator.

## 2.5 Metamaterial biosensors

It is believed that metamaterials were initially introduced in the late 1890s by *Jagadis Chunder Bose* [36]. He did some experiments on artificial chiral elements which were called twisted structures at the time. *Karl F. Lindman* extended the extraordinary characteristics of metamaterials in 1910s by embedding some randomly directed wire helices in an artificial chiral media [37]. Later in 1940’s *Winston E. Kock* tailored conducting strips periodically in an artificial media, in a way that the inclusions would be arranged in a pattern beside one another, not to be just randomly scattered on the medium [38].

These new materials were originally defined as “Macroscopic composites having a synthetic, three-dimensional, periodic cellular architecture designed to produce an optimized combination, not available in nature, of two or more responses to specific excitation” [39]. Later, the term “Metamaterial” was introduced by Rodger M. Walser, University of Texas at Austin, in 1999 [40].

Ever since, there has been a great deal of improvement in artificial material science and different types of metamaterials have been proposed, produced and tested [41]. The exotic properties of a metamaterial is strongly dependant on the geometry of metamaterial sub-structures along with their composition [42]. A wide range of applications are proposed using this exclusive characteristic of metamaterials, such as sensing [1], optical switching [43], slow light [44], data storage [45], cloaking [46] etc. These applications are proved to be achievable in a wide range of electromagnetic spectrum, from far-infrared to optical frequencies [47, 48].

### 2.5.1 Planar metamaterials used for sensing

Planar metamaterials are artificially manufactured through layering specifically engineered inclusions on a substrate (Figure 2-3). The inclusions are ideally made smaller than the wavelength of the incident electromagnetic wave. These manmade materials are mostly popular for their unusual properties that cannot commonly be found in the nature.

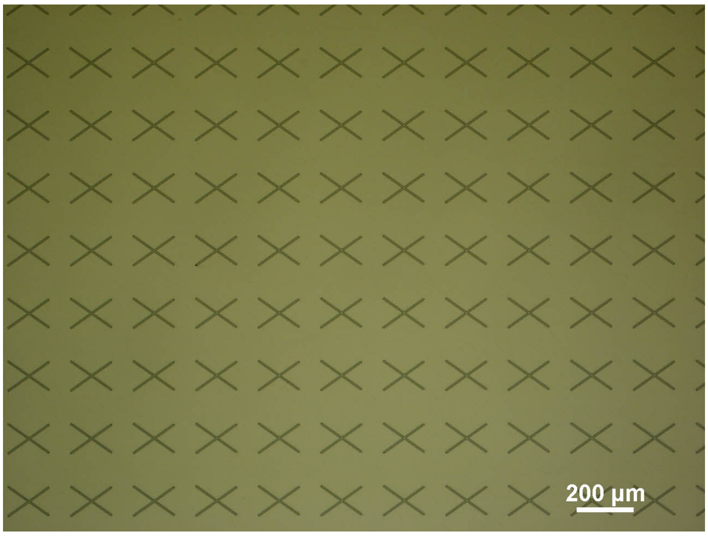

Figure 2-3 Optical microscope image of a metamaterial with X-shaped resonators as inclusions on a COC substrate

Metamaterial inclusions being smaller than the wavelength of external stimulus, in a sense, represent the atoms and molecules of conventional materials. In turn, the metamaterial as a whole, replicates a homogenous material in the macro scope [49]. Professor N I. Zheludev, one of the pioneers in the field of metamaterials, suggests that “Conventional materials derive their electromagnetic characteristics from the properties of atoms and molecules, metamaterials enable us to design our own atoms” [41].

#### 2.5.1.1 Sensing with metamaterials

One of the well-recognized applications of planar metamaterials is sensing, where planar structures that produce narrow resonances can be used for detection of low-concentration analytes [41].

Development of small resonant sensors probably became essential when necessities such as small sensors with ability to provide a high concentration of electrons arose. One of the first sensors developed for this purpose was at 1939 by *Hansen et al.* [50] who produced re-entrant cavities suitable for klystron oscillators.

A few decades later, at 1981, *Hardy et al.* [51] showed that split-ring resonator can be used for magnetic resonances, where ordinary cavities were generally too bulky. Later in 1999 and 2000, *Pendry et al.* [52] and *Smith et al.* [53] continued with the same subject, studying magnetism from conductors and composite mediums [54].

In 2002, Marques *et al.* [55] simplified the properties of split ring resonator by lumped elements and approximated them by

- Ignoring the gap capacitance on the basis that they are small and unlikely to have a major influence on the flow of currents.
- Ignoring the mutual inductance of the split ring.
- Taking the self-inductance equal to the average self-inductance of the two rings.
- Considering the two inter-ring capacitances between the splits as being connected in series.

This simplified physical picture lead to an excellent approximation of metamaterials and was widely used to study, the way metamaterial inclusions interact with external stimuli [56].

These studies have been advanced in the recent years [35, 57, 58],and show that the ability of metamaterials in localization of the field can make them very good candidates for bio-sensing, by improving the sensitivity and resolution of current sensors. For instance, *Papasimakis et al.* [59] have shown that a single molecular layer of carbon can induce a change in the frequency response of a metamaterial, when in close range with an external stimuli.

## 2.6 THz Metamaterials

### 2.6.1 THz region of the electromagnetic spectrum

In the past few decades, terahertz spectroscopy has become more and more popular. For the first time, the term terahertz was allocated to this gap in the electromagnetic spectrum in the mid-1970s, but it was not until the mid-1980s when through the development of ultra-fast optoelectronics, THz pulses were generated and discovered [60]. Before that, such radiations were referred to as sub-millimetre or far-infrared waves. This discovery led to a huge interest in exploring this specific region of the electromagnetic spectrum. Primary researchers in this area were mainly concentrated on creating THz waves which are detectable and manageable. Since then after invention of the first pulsed THz system, the researchers' focus is altered to find practical and feasible applications for THz radiations, as there are many vibrational modes of biological cells in the THz region. [60]

### 2.6.2 Sensing with metamaterials in THz

One of the first planar metamaterials to demonstrate magnetic resonance behaviour in THz region was proposed by *Yen et al.* [61] in 2004. They used an array of nonmagnetic, conducting, split-ring resonators with periodicity of one seventh of the wavelength of the excited field at resonance frequency. They showed that the structure is resonant at 300 µm wavelengths, which is much larger than its physical dimensions.

In 2007, Yoshida et al. [62], introduced a label-free detection method in THz region by using a thin metallic mesh. They observed a shift in the transmittance frequency response, when the metallic mesh loaded with the analyte (horseradish peroxidase) was in presence of THz radiation and. This shift occurs due to the change in the refractive index of the model, by adding the horseradish peroxidase sample. [27]

Later on in 2008, planar wallpaper-based metamaterials with hexagonal and square inclusions were utilized for protein detection [63] to be used for biochemical hazard detection, as well as electromagnetic signature control. Since then, several studies have been carried out for label-free detections of biomolecules in THz [64-68] and to advance the ability of metamaterial-based THz sensors to achieve a higher degree of sensitivity and reliability.

### 2.6.3 **Recent advances in metamaterial-based sensors**

*Tao et al.* [69], presented a planar metamaterial with SRR-based inclusions for glucose detection in THz frequency range (0.5–2.5 THz). The metamaterial with minimum features of less than 5 µm was fabricated on a paper substrate using a photoresist-free shadow mask deposition technique. According to their study, the amount of D-glucose added to the sensor is identified by the drop in the intensity of the resonance peak. They also report the ability of their sensor to distinguish between D-glucose and urea, by comparing the drop in the intensity and shift in the frequency of the resonance peak. One of advantages of the sensor proposed by *Tao et al.* [69] is that paper is almost transparent in THz, is inexpensive, abundant and could be more accessible to the average user [11]. However, paper, being disposable, eliminates the possibility of reusing the sensor. Also the surface roughness of the paper substrate affects the quality of the metamaterial patterned on it, and affects the sensitivity of the sensor. Another disadvantage to paper substrates is the inability of achieving well-defined patterns with high resolution. This is due to porosity of paper which makes it impossible to use conventional photolithography-based microfabrication techniques where chemical solutions are commonly used and result in distortion and degradation of paper [69]. Furthermore, although the results reported by *Tao et al.* [69] suggest the possibility of distinguishing between D-glucose an urea; the prospects of multiple analyte discrimination is not readily accessible with this sensor, due to short resonance peaks and low Q-factor.

In 2007, *Fedotov et al.* [17] reported the ability to achieve a sharp trapped-mode resonance by using asymmetric copper double split rings as metamaterial inclusions in mm range. They showed that by patterning asymmetrically split rings on an IS620 PCB (printed circuit board) substrate, the two asymmetric parts of the split rings are excited in antiphase, with currents of almost the same amplitude. This results in a trapped-mode resonance risen from the interference between two high-quality resonances. The trapped-mode occurred at ~6 GHz with the quality factor of ~20.

*Lahiri et al.* [10], tried to replicate *Fedotov*'s results in the mid-infrared region for DNA detection by downsizing the metamaterial cells from 15×15 mm$^2$ to 2.5×2.5 µm$^2$. In their model they patterned asymmetric gold resonators on a silica substrate. The transmission results were in agreement with Fedotov's [17], in terms of successfully producing a trapped-mode resonance when the metamaterial was in close range with external stimulus. However the trapped-mode resembled a gentle slope rather than a narrow peak, which resulted in a low Q-factor of ~7, which would not be high in selectivity to discriminate between different analytes.

Another study was carried out *by Wang et al.* [70], who modelled a metamaterial with 70 × 70 $\mu m^2$ inclusions containing vertical double split ring resonators. The structure was designed on a polyimide substrate and produced a resonance in THz region (0-2 THz). The idea behind the vertically placing of split ring resonators on the substrate, was to reduce the dielectric losses resulting from the substrate by reducing the contact area of resonators with the substrate and alternatively surrounding them with air, which has a relative permittivity close to unity. Although their simulation suggests a higher Q-factor (~20) compared to Lahiri's, the Q-factor is not high enough for accurate track of resonance frequency shift for sensing purposes. Also, fabricating the resonators vertically on the substrate, can be difficult and complicated.

Numerous other studied have been reported for sensing in THz region using planar metamaterials, which mostly use metamaterials with split ring inclusions [9], and silica substrate [10, 19] (not completely transparent in terahertz) with quality factors achieved between 10 and 20 [11-16, 18]. Although the method used in the aforementioned studies is promising, the sensitivity of the sensor is not reliable. This is because, resonance curves with a gentle slope do not have an accurate selectivity when it comes to detecting the shift in the frequency response as opposed to resonances with steep peaks.

As a result, there is a room for improving the sensitivity and selectivity of the metamaterial-based biosensors, by introducing new resonator geometries for metamaterial inclusions, patterned on a substrate which is inert to organic compounds, has a high transparency in THz and can be used in common microfabrication techniques. This all can result in achieving higher quality factors and increasing the sensitivity for multiple analyte discrimination.

Later in Chapter 7, we show that, the proposed metamaterial-based sensor in this study, exceeds the selectivity and sensitivity of the current models [12, 13, 15, 18], by improving the Q-factor of the resonance peak, using X-shaped resonators on a COC substrate.

# Chapter 3 (Literature Review) Introduction to Computational Electromagnetics

Electromagnetic field theory helps with understanding the way the metamaterials interact with electromagnetic radiation and the surrounding environment by means of Maxwell's equations. [71]

Maxwell's equations can be analytically incalculable in case of numerous irregular geometries. However, Computational Electromagnetics, can overcome extensive analytical calculations by utilising boundary conditions and constitutive equations.

One method is to divide the geometry under study into grids (discretising), then Maxwell's equations can be solved for each point of every grid separately. There are different techniques used in computer simulators, either solving differential or integral form of Maxwell's equations. Throughout this study, CST Microwave studio suite [72] is used. CST microwave studio suite, uses Finite Integration Technique (FIT) to solve the wave equations.

## 3.1. Maxwell equations

Maxwell's equations are set of four differential equations (Eq.3.1_3.4) that describe the electromagnetic fields and their connection to the currents and charges.

$$\nabla \cdot \bar{D} = \rho \tag{3-1}$$

$$\nabla \cdot \bar{B} = 0 \tag{3-2}$$

$$\nabla \times \bar{H} = \bar{J} + \frac{\partial \bar{D}}{\partial t} \tag{3-3}$$

$$\nabla \times \bar{E} = -\frac{\partial \bar{B}}{\partial t} \tag{3-4}$$

, where $\bar{E}$ is the electric field ($V/m$), $\bar{H}$ is the magnetic field ($A/m$), $\bar{D}$ is the electric flux density ($C/m^2$), $\bar{B}$ is the magnetic flux density ($Wb/m^2$), $\rho$ is the electric charge density ($C/m^3$) and $\bar{J}$ is the electric current density ($A/m^2$).

In free space, electric flux density is the product of permittivity of free-space ( $\varepsilon_0 = 8.854 \times 10^{-12} F/m$) and electric filed density. Correspondingly, magnetic flux density is the product of permeability of free-space ($\mu_0 = 4\pi \times 10^{-7} H/m$) and electric filed density. [73]

$$\bar{B} = \mu_0 \bar{H} \tag{3-5}$$

$$\bar{D} = \varepsilon_0 \bar{E} \tag{3-6}$$

These general equations describe the electromagnetic problem irrespective of its frequency. For practicality, where a specific frequency band is involved, the Electric Flux Density ($\bar{D}$) is given by equation (3-7), where $\overline{P_e}$ is the *electric polarization vector* [73].

$$\bar{D} = \varepsilon_0 \bar{E} + \bar{P}_e \qquad 3\text{-}7$$

For linear materials (like a metamaterial inclusion), the electric polarization vector is given by,

$$\bar{P}_e = \varepsilon_0 X_e \bar{E} \qquad 3\text{-}8$$

, where, $X_e$ is the *electric susceptibility.* Substituting $\bar{P}_e$ in equation (3-7), gives,

$$\bar{D} = \varepsilon_0 \varepsilon_r \bar{E}\ ;\ \varepsilon_r = \varepsilon' - \mathrm{j}\varepsilon'' = \varepsilon_0(1 + X_e) \qquad 3\text{-}9$$

, where $\varepsilon_r$ is the epsilon relative of a material. In reality, materials exhibit loss mechanisms, where the oscillation of the charges which form the dipole moments are damped. This appears in the complex permittivity as the imaginary part ($\varepsilon''$). As a result, a material with zero loss has only the real part [73].

For anisotropic materials, e.g. metamaterials, the electric flux density ($\bar{D}$) cannot be easily assumed to be in the same direction as the direction of the electric field ($\bar{E}$). It has a more complex relation and can be shown as a dyad tensor (Equation 3-10)

$$\begin{bmatrix} D_x \\ D_y \\ D_z \end{bmatrix} = \begin{bmatrix} \varepsilon_{xx} & \varepsilon_{xy} & \varepsilon_{xz} \\ \varepsilon_{yx} & \varepsilon_{yy} & \varepsilon_{yz} \\ \varepsilon_{zx} & \varepsilon_{zy} & \varepsilon_{zz} \end{bmatrix} = [\varepsilon] \begin{bmatrix} E_x \\ E_y \\ E_z \end{bmatrix} \qquad 3\text{-}10$$

The same relation applies to the electric polarization ($\bar{P}_e$) and electric field ($\bar{E}$) for nonlinear media [73].

## 3.2. Electromagnetic wave equations

The Maxwell's equations for an isotropic and source free region can be written as,

$$\nabla \cdot \bar{E} = 0 \qquad 3\text{-}11$$

$$\nabla \cdot \bar{H} = 0 \qquad 3\text{-}12$$

$$\nabla \times \bar{E} = -j\omega\mu\bar{H} \qquad 3\text{-}13$$

$$\nabla \times \bar{H} = j\omega\varepsilon\bar{E} \qquad 3\text{-}14$$

By taking the curl of the equation (3-13) and substituting (3-14), equation (3-15) is given.

$$\nabla \times \nabla \times \bar{E} = -j\omega\mu\ \Delta \times \bar{H} = \omega^2 \mu\varepsilon\bar{E} \qquad 3\text{-}15$$

Using vector identities, the equation (3.15) can be simplified to,

$$\nabla(\nabla . \bar{E}) - \nabla^2 \bar{E} = k^2 \bar{E}\ ; k = \omega\sqrt{\mu\varepsilon} \qquad 3\text{-}16$$

, where $k$ is the wave number.

$\nabla.\mathrm{\overline{E}} = 0$, as a result, equation (3-16) can be modified, and the *Electromagnetic wave equations* is given by:

$$\nabla^2\bar{E} + k^2\bar{E} \ = 0\ ;\ k = k_0\sqrt{\mu_r\varepsilon_r} \qquad 3\text{-}17$$

, where $k_0$ is the free-space propagation constant, equal to $2\pi/\lambda_0$ ($\lambda_0$ is the free space wavelength).

For the transverse mode of electromagnetic radiation (Figure 3-1). The polarization is in the direction which electric-field is oscillating.

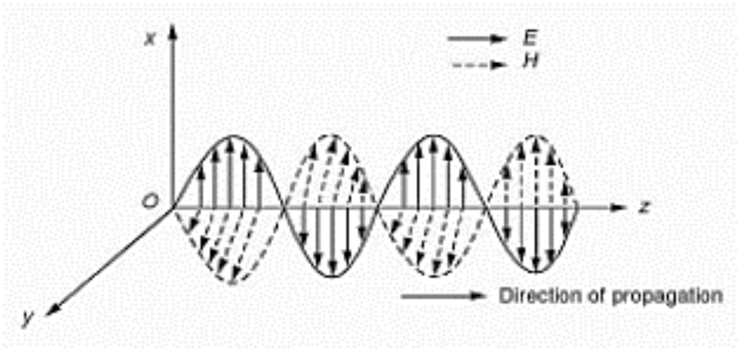

Figure 3-1 A Transverse electromagnetic (TEM) wave, showing the propagation direction, and the direction of electric and magnetic fields. [74]

## 3.3. Finite integration technique (FIT)

FIT is a discretisation method for integral form of Maxwell equations (Equation 3-18 to 3-21) using orthogonal dual grids (Figure 3-2). The method can be applied to either hexahedral or tetrahedral grids. However, in CST microwave studio simulator, it is recommended to use Frequency domain solver and tetrahedral mesh for resonant structures to achieve an approximation closer to the reality [72] .

$$\int \bar{D}.d\bar{A}=\int_V \rho.dV \qquad 3\text{-}18$$

$$\int \bar{B}.d\bar{A}=0 \qquad 3\text{-}19$$

$$\oint_a \bar{H}.d\bar{s}=-\int_A (\frac{\partial\bar{D}}{\partial t}+\bar{J}).d\bar{A} \qquad 3\text{-}20$$

$$\oint_a \bar{E}.d\bar{s}=-\int_A \frac{\partial\bar{B}}{\partial t}.d\bar{A} \qquad 3\text{-}21$$

For simplicity, the steps for discretization are explained for hexahedral grids. But these can also be applied to tetrahedral grids, with no difference.

To be able to set the Maxwell's equations, the program defines a three dimensional space comprising the electromagnetic field.

Spatial discretisation is achieved by using suitable mesh system and breaking down the continuous space to a number of finite volumes (grids cells) [75]. In this manner, Maxwell equations are transformed to algebraic analogues (Maxwell's grid equation) for discrete space, maintaining the physical properties of the field [76].

In *CST STUDIO SUITE*, a secondary, dual mesh is created internally orthogonal to the primary grid. Then, the Maxwell's grid equations are applied to these orthogonal mesh structures. [72] This is achieved by allocating electric voltages on the edges and magnetic fluxes on the faces of the primary grid, and magnetic voltages on the edges and electric fluxes on the faces of the dual grid [76].

Maxwell equations are written for every side of every grid. This way, the topological matrix of C is created, which is the equivalent of the curl operator in the continuous form of Maxwell's equations.

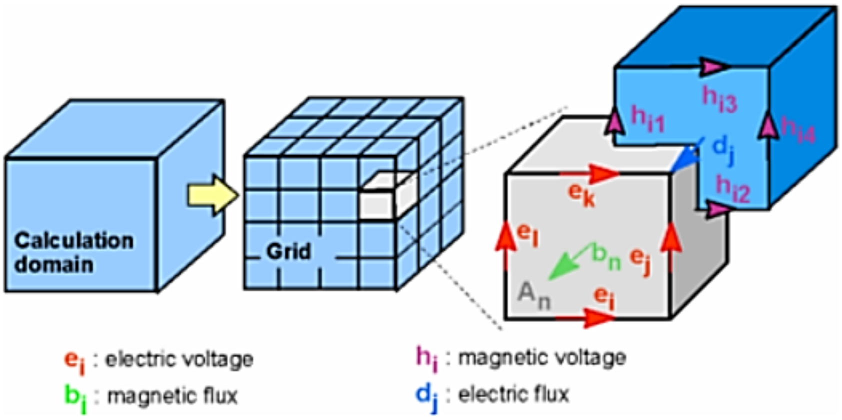

Figure 3-2 Dual grid technique for FIT [72]

The integral of the voltage and fluxes relations is approximated, and is dependant on the material properties.

The discrete Maxwell equations can be written as:

$$\bar{B} = \mu_0 \bar{H} \Rightarrow \mathrm{b} = \mathrm{M}\mu\, \mathrm{h} \qquad 3\text{-}22$$

$$\bar{D} = \varepsilon_0 \bar{E} \Rightarrow \mathrm{d} = \mathrm{M}\varepsilon\, \mathrm{e} \qquad 3\text{-}23$$

Next, the electromagnetic wave equations are solved using the boundary conditions and grids.

## 3.4. Boundary conditions

In order to solve the Maxwell equations for the model, boundary conditions need to be set. Solutions to these conditions provide an answer to differential equations for particular specifications.

In this study, boundary conditions are set as either open or periodic:

### 3.4.1. Open boundaries

Open boundaries are set so the wall performs as the free space. This boundary condition is especially designed let the waves to pass with zero reflection.

### 3.4.2. Periodic conditions and Bloch-Floquet theorem

When a periodic boundary condition is set, the calculation domain is extended to the equivalent direction of the boundary by changing the opposite boundary to a periodic wall periodically. This way the coupling effect of each metamaterial inclusion with the neighbouring inclusion will be taken into account.

For solving periodic linear differential equations in a two dimension boundary, floquet ports are used. Floquet ports engage the Bloch-Floquet theory. The theory shows that waves can travel in a periodic structure without being scattered. This behaviour can be governed as a “periodic envelope function multiplied by a planar wave”[77].

The field is explained as a plane field with an envelope

$$\overline{H}(\mathrm{r}) = e^{jkr}.\bar{\mathrm{u}}(\mathrm{r}) \qquad 3\text{-}24$$

, where $\overline{H}$ is either the magnetic or electric field vector and $\overline{u}$ is the periodic envelope function [77].

In the simulation, by applying Floquet ports in X and Y directions, the periodic system is transformed to linear.

## 3.5. Frequency Domain Solver

In the Frequency Domain calculations, simulations are repeated for every sample frequency, solving the Maxwell’s grid equations. The sample frequencies are chosen over the frequency range that is chosen by the user. The results for the whole frequency range can be seen by plotting the S-parameters [72].

## 3.6. Scattering parameter (S-parameters)

To visualise the behaviour of a system in response to an electromagnetic stimuli and the properties of an electrical network, S-parameter results are derived. In the current model, a two-port network, the S-parameters are defined as the ratio of the reflected wave over the incident wave at port one ($S_{11}$) when port two is terminated in a matched load [73]. Similarly, the ratio of the reflected wave from port two back to port one, ($S_{21}$) (Figure 3-3), when port one is terminated in a matched load. $S_{11}$ is the reflection coefficient ($\Gamma$) and is used to show how much power is reflected from the structure. Therefore, if $S_{11} = 0\ dB$, it shows that all the wave is bounced back and nothing has passed through port two. In the same manner, $S_{21}$ represents the amount of wave received at port two relative to port one, so $S_{21} = 0\ dB$ implies that all the power has passed through or absorbed at port two.

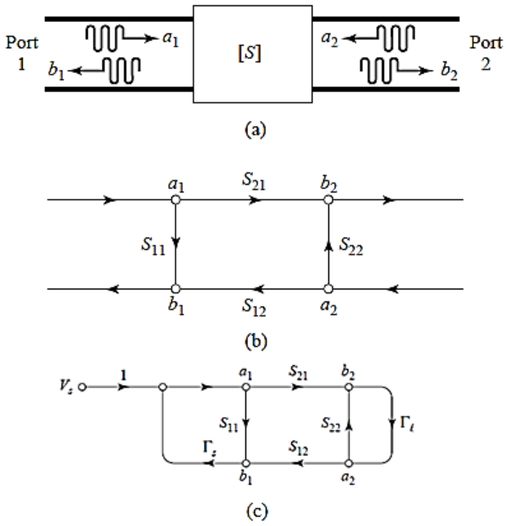

Figure 3-3 Two-port network (a) Incident and reflected waves (b) The wave interaction with the device under test is characterised by scattering parameters $s_{11}$(the reflection coefficient) and $S_{21}$(the scattered wave) in the form of a signal flow graph (c) The same flow graph as represented in part b plus a general source and load impedance [73]

## 3.7. Material properties

Wave equations will have different solutions depending on the material through which the wave is propagated. Hence, a good understanding of the material properties is very important. Different material models have been developed in order to properly mimic the material properties. These models are based on mathematical calculations and since all of the material characteristics are frequency dependent, the models are constructed based on the frequency response of materials to electromagnetic radiation for finding the parameters specific to the materials [37].

One of the material models that is proposed based on the electrical conductivity of a substance (movement of charged particles in a material) is the Drude model. Drude model was introduced by *Paul Drude* in 1900 [78], he presented the model in order to explain the act of polarization in the metals by assuming that the movement of electrons can be seen as a pinball machine as the electrons spring back and force in different directions in the hosting material (this movement of electrons happens harmonically while under the influence of harmonic electric or magnetic fields) while the atom nucleus (positive charges) remain still [78]. In 1905 *Hendrik A. Lorentz* [79] expanded the model by assuming that the restoring force is not always negligible. The new model was named after him, Lorentz model, and often is called Drude-Lorentz model [79].

### 3.7.1. Drude and Lorentz models

The Lorentz model, which describes the temporal response of the structure, is one of the most recognised material models. As explained, Drude and Lorentz models are created as a result of the description of the harmonic oscillation of electrons. For the simplification of the model it is assumed that the electrons are moving in the same direction of the present field (e.g. electric field).

The polarization of the material to the presence of an electric field, equals to the acceleration of the charges plus the damping mechanism of the system plus the restoring forces (with frequency response of $P_i$ damping coefficient of $L$, natural frequency of $f_0 = \omega_0/2\pi$, permittivity of $\varepsilon_0$, coupling coefficient of $\chi_L$ and, electric field of $E_i$ [37].

$$\frac{d^2}{dt^2}P_i + \Gamma_L\frac{d}{dt} + {\omega_0}^2 = \varepsilon_0 X_L E_i \qquad \text{3-25}$$

The electric susceptibility of the Lorentz model can be specified as

$$X_{e,lorentz}(\omega) = \frac{P_i(\omega)}{\varepsilon_0 E_i(\omega)} \qquad \text{3-263-27}$$

And by extracting the frequency response from the equation (3-25) [ $P_i(\omega) = \frac{X_L}{-\omega^2+j\Gamma_L\omega+{\omega_0}^2}\varepsilon_0 E_i(\omega)$] and substituting in (3-26), the $X_{e,lorentz}(\omega)$ is given by

$$X_{e,lorentz}(\omega) = \frac{X_L}{-\omega^2 + j\Gamma_L\omega + {\omega_0}^2} \qquad 3\text{-}28$$

As a result the permittivity ($\varepsilon_0$) can be calculated from the equation (3-28). [80]

$$\varepsilon_{\text{Lorentz}}\,(\omega) = \varepsilon_0\,[1 + \ X_{e,\text{Lorentz}}\,(\omega)] \qquad 3\text{-}29$$

As previously mentioned, Drude model is a simpler version of the Lorentz model, where the restoring force is assumed to be negligible, (Equation 3-29).

$$X_{e,Drude}(\omega) = \frac{X_D}{-\omega^2 + j\Gamma_D\omega} \qquad 3\text{-}30$$

Similarly, equations for Lorentz and Drude models can be obtained for magnetic properties of the material, with $H_i$ representing the magnetic field, $X_m$ representing the magnetic susceptibility and $\mu_0$ representing the permeability of the free space. Via equation (3-30), $\mu(\omega)$ is obtained,

$$\mu_{\text{Lorentz}}\,(\omega) = \mu_0\,[1 + \ X_{m,\text{Lorentz}}\,(\omega)] \qquad 3\text{-}31$$

### 3.7.2. Refractive index

The refractive index of a material defines the way that wave propagates through a material. The refractive index can determine how the wavelength of the radiation is changed in respect to the vacuum, when passing through a material.

Refractive index of a material ($n$) is calculable using equation (3-31)

$$n = \frac{K}{K_0} = \sqrt{\mu_r \varepsilon_r} \qquad 3\text{-}32$$

### 3.7.3. Skin depth

For resonating structures in frequencies around 1 THz, a thin coating of a low loss conductor (e.g. gold) is enough [73]. This is due to characteristics depth of penetration, or as often called, Skin depth of e metal

$$\delta = \sqrt{\frac{2}{\omega\mu\sigma}} \qquad 3\text{-}33$$

, with $\sigma$ denoting the conductivity. The field amplitude decays by 36.8%, after one skin depth, which is a small distance for THz frequencies. For example at 1THz for gold the skin depth is 0.0753um.

### 3.7.4. Material properties in CST Microwave Studio

CST has a range of predefined materials parameters for certain mediums. However, it is possible to add a new material or to add the dispersion of an existing material in a specific frequency rang. This can be done by adding the complex permittivity of the material at a given frequency range.

*Yasuda et al.* [81] measured the complex refractive index of gold experimentally. The complex relative permittivity of gold in the THz region was calculated using (Equation 2.32), for frequencies between 0.6 and 1.2 THz and was fed to the dielectric dispersion model of gold in the simulation.

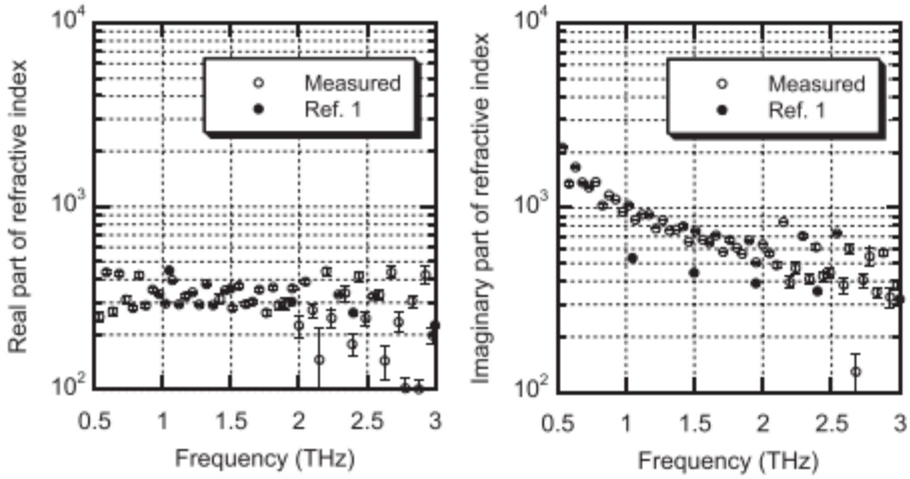

Figure 3-4 Complex refractive index of gold, measured for frequencies between 0.5 and 3 THz by *Yasuda et al.* [81]

# Chapter 4 Literature Review (Introduction Terahertz Time Domain Spectroscopy)

## 4.1 Introduction

Terahertz region of the electromagnetic spectrum (Figure 4-1) with the frequency band of 0.3 to 3 terahertz (wavelength of 1 to 0.1 mm) occupies a small gap between the microwave and the infrared regions (Figure 4-1). THz band is usually known as the terahertz gap, as it is a less explored region, compared to its neighbouring frequencies. As well, since the wavelength in the THZ region starts from 1 mm, the region is sometimes also referred to as the sub-millimetre band.

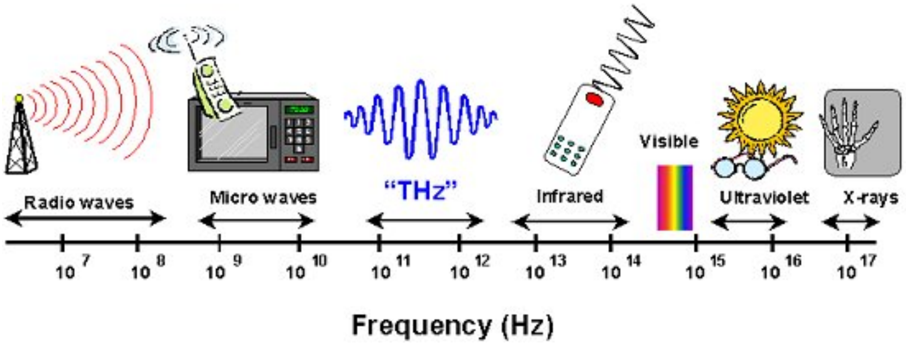

Figure 4-1 Electromagnetic spectrum and the proposed application for each region. [82]

Although, being located between the two of relatively well-explored regions of electromagnetic spectrum, (microwave and infrared regions) terahertz region is still a less explored region with lots of possibilities. As there are lots of promising applications proposed in the THz region such as biosensing [47-49].

There are few elements and materials found in the nature with high quality factors and electronic properties between 1 and 3 terahertz [50]. This is because generally magnetic materials show resonances in the radio frequencies and metallic compounds have resonances in the infrared region [51]. As a result, it is important to investigate the possibility of producing new structures, which have electromagnetic characteristics in the THz region.

For this, metamaterials can be considered vital, because they can be tailored to produce electromagnetic properties, tailored to a specific frequency range [52].

In the current study, the sensor is tailored to perform in the THz region as numbers of practical and theoretical studies have shown several resonances associated with DNA binding state in the THz region [1].

## 4.2 THz time domain Spectroscopy (TDS)

THz spectroscopy is the act of generating and detecting THz pulses. This can be done with an ultrafast or near-infrared [83] laser. One of the approaches for THz spectroscopy is Terahertz time domain spectroscopy (generally known as THz-TDS).

The main advantage of THz-TDS is enabling to directly measure the electric field of the radiation, whereas most spectroscopy methods only measure the intensity of the radiation [83]. This results in the determination of both absorption and refractive index of the sample through THz-TDS. Therefore, the output contains both the magnitude and the phase of the field [82].

In Benchtop THz-TDS, short pulses are generated by femtosecond lasers. The pulses, ranging from 100-10 femtoseconds in width, allow for time-resolved spectroscopy [83].

## 4.3 THz-TDS setup

The setup (Figure 4-2) uses a Titanium Sapphire (Ti:Sapphire) femtosecond (fs) laser with a continuous wave power of approximately 1.2 (Watt). When mode is locked through a lock-in amplifier (used to improve signal detection), the laser produces pulses of approximately 60 (fs) duration at 800nm wavelength. The beam is split into two paths, one sent to the THz emitter and one sent to a computer controlled delay stage and then into the THz receiver.

The THz pulse is generated by a 'photoconductive antenna' which consists of a GaAs semiconductor substrate with two metallic electrodes held at a voltage bias (~12V). When the laser pulse hits the emitter it generates charge carriers in the GaAs which are accelerated in the electric field of the voltage difference creating a current.

The current created evolves over a number of picoseconds, and because of accelerating electrons there will be emission of electromagnetic radiation proportional to the temporal derivative of the current.

The THz pulse is emitted linearly polarized (horizontally) in a wide cone. The THz cone is passed through a parabolic lens to collimate. Another lens focuses the beam onto the sample, the next lens collimates, and the final lens focuses the beam onto the receiver.

The detector works on a similar principle to the emission method except there is no voltage difference applied between the metallic electrodes. The laser pulse creates charge carriers in the GaAs substrate and the electric field of the THz radiation accelerates the carriers. Subsequently, the current between the electrodes is measured.

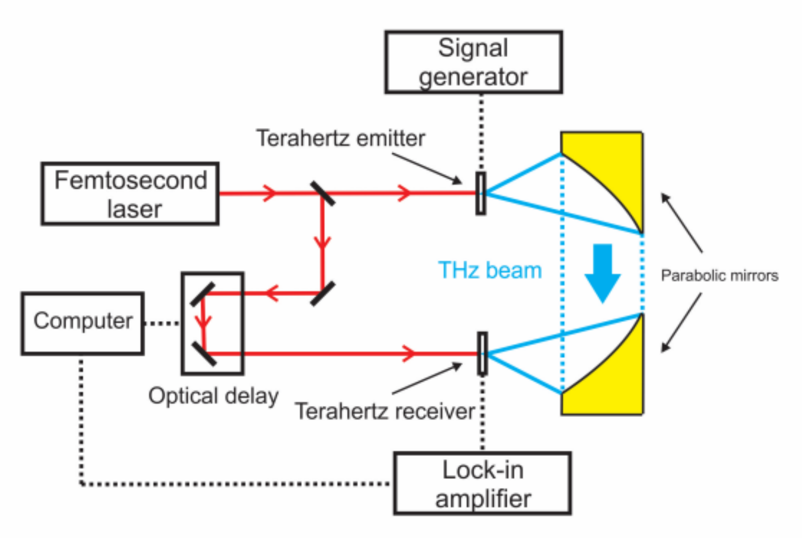

Figure 4-2 Schematic of a typical Ti:sapphire Terahertz time domain spectrometer. [84]

It would be ideal to measure the current at sub-picosecond timescales allowing to see directly how the current changes over the length of the THz pulse, but electronics are not fast enough for this. Instead the measurement is done over a number of milliseconds with many thousands of terahertz pulses and femtosecond pulses being generated and measured. On the lock-in amplifier a constant current is observed.

To determine how the current changes in time the delay stage can be used to increase the beam path to the detector; this means the charge carriers will be created slightly later and therefore the current is measured at a slightly delayed time. The beam path is slowly increased so that the current is probed at all times across the pulse length.

## 4.4 Data Analysis for THz-TDS

The amplitude and the phase of spectra are measured in time domain, using THz time domain spectroscopy. The data recorded is simply a long list of time and current values in time domain .The amplitude of the spectra is shown as a current over time plot, showing the THz pulse ( Figure 4-3). A Fast Fourier Transform (FFT) is performed on the data to transform it into the frequency domain.

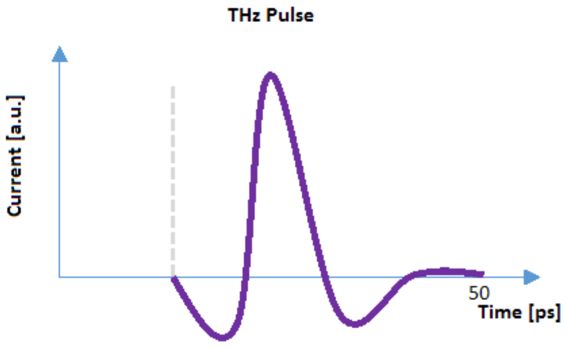

Figure 4-3 Time domain scans of the THz electric field, resulting in the time-domain THz pulse

The Fourier transform outputs a frequency dependant complex number ($r + \ i\ \varphi$). This complex number is transformed from Cartesian to polar coordinates ($r.\, e^{i\ \varphi}$) (Figure 4-4).

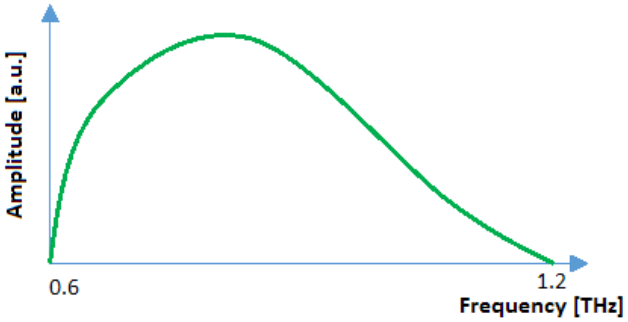

Figure 4-4  Amplitude of the spectra in the frequency-domain

The angle $\varphi$ is 'wrapped' which means it oscillates between 0 and 2π (when the phase makes one full rotation the angle goes back to zero so its history is lost). To recover the history of the phase the unwrapping function is used, which essentially counts the phase and when it makes one full rotation the value does not jump back to zero but instead keeps increasing (Figure 4-5). This is achieved by detecting the cut-offs in the phase that are greater than 1.4 π (where the 2π steps in the phase occur in frequency). The function then adds −2pπ to a section of the phase that is in between the steps.

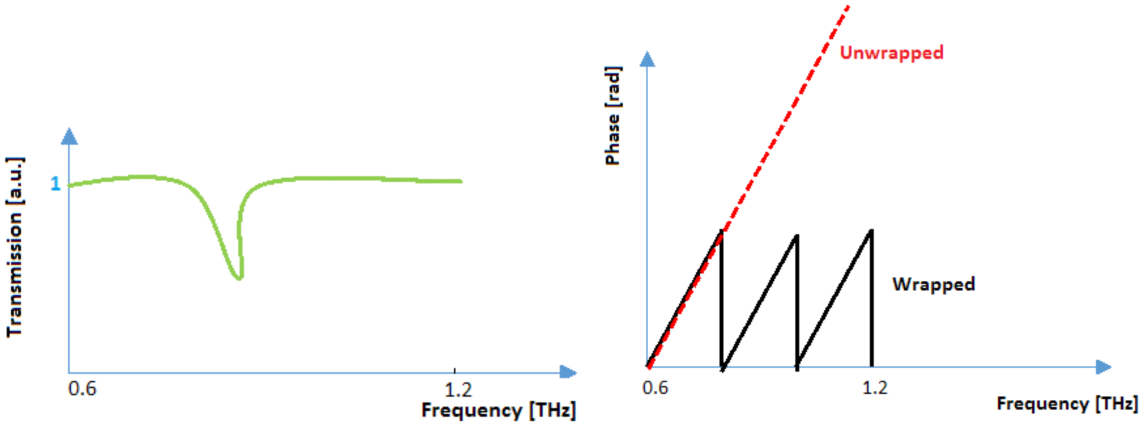

Figure 4-5 Transmission and phase spectra of the sample

### 4.4.1 Scan frequency resolution ($f_s$):

The data is measured in the time domain and converted to the frequency domain via a Fourier transform. As a result, the resolution in frequency ($f_s$) will be given by

$$f_s = \frac{1}{\Delta T \times nfft} \tag{4-1}$$

, where *T* is the resolution in time and $nfft$ is the number of points measured.

### 4.4.2 Extracting the material properties

By measuring the amplitude and the phase of the THz electric field using the Terahertz time-domain spectrometer, the direct calculation of the real and imaginary parts of the material constants of a material in the THz region is possible. This makes it possible to determine the complex refractive index of a material.

$$\tilde{n}(w) = n(w) + i(w) \tag{4-2}$$

The real part of the refractive index is dependent on the speed of the radiation and the imaginary part is dependent on the amplitude of the spectra. ($w$, is the extinction coefficient of the material).

The complex refractive index of the material is achieved by fitting the theoretical transfer function into the experimental transfer function.

The experimental transfer function $H(w)$ is calculated by dividing the sample FFT by the reference FFT resulting in the transmission spectra. The result is a frequency dependant complex number.

The amplitude of the sample (the metamaterial) scans is divided by the amplitude of the reference (substrate of the metamaterial) scans. This way, the effects of the THz propagation before it hits the sample, and once it has passed through the sample, is divided out of the data.

$$H(w) = \frac{r_{samp}\, e^{i\varphi_{samp}}}{r_{ref}\, e^{i\,\varphi_{ref}}} = \frac{r_{samp}}{r_{ref}}\, e^{i\,(\varphi_{samp} - \varphi_{ref}\,)} \qquad \text{4-3}$$

The theoretical transfer function is created and a fitting algorithm, to vary the frequency dependant complex refractive index in the theoretical transfer function until it is a good fit with the experimental transfer function [84].

Here, the *Newton – Raphson method* (Equation 4-4) is used as the fitting algorithm. First, $x_i$ chosen randomly in Equation 4-4. The equation is solved until the change in the $H_i$ is close to zero.

$$x_i + 1 = x_i - \frac{f(x_i)}{f\prime(x_i)} \qquad \text{4-4}$$

In the case of the theoretical transfer function, the function that is solved by the *Newton – Raphson method* is defined as [84]:

$$f(\omega, \tilde{n}) \;=\; \ln(H_{theo}(\omega, \tilde{n}(\omega))) \;-\; \ln(H_{exp}(\omega)) \qquad \text{4-5}$$

The result of solving the fitting algorithm for each frequency is a graph of frequency dependant complex refractive index.

# Chapter 5 **Design and Simulation**

## 5.1 Introduction

Compared to single resonators, metamaterials show strong coupling to an electromagnetic field. Each cell of the metamaterial is designed in a scale smaller than the wavelength of the incident electromagnetic wave. Resulting in stronger localization of the electromagnetic field, because the cells, all together, act as a homogenous material.

A single resonator was modelled with all the physical characteristics of a metamaterial inclusion (Figure 5-2), to compare its frequency response with that of the metamaterial. The waveguide ports were set at $\pm Z$, and a Gaussian pulse was set as the excitation signal. The boundary condition at X and Y directions was set to open, in oppose to the periodic condition for the metamaterial.

Figure 5-1, shows the trapped-mode resonance of the single-cell resonator compared to the trapped-mode resonance of the metamaterial, in response to a plane electromagnetic wave. Distinctly, the resonance produced from the metamaterial is considerably steeper, and easier to use for sensing small changes in response to an analyte.

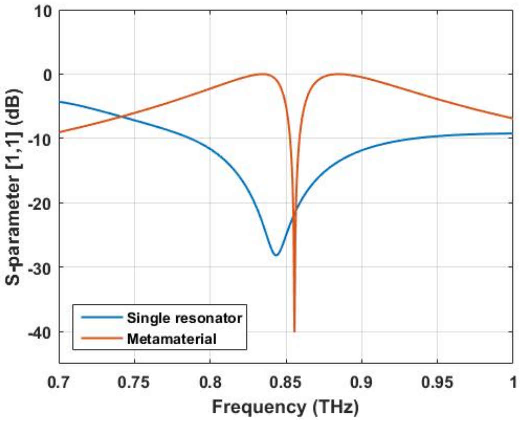

Figure 5-1 The trapped-mode resonance of a single-cell resonator vs the trapped-mode resonance of a metamaterial

Conventionally, these type of metamaterials use split ring resonators as their inclusions [17, 18]. To increase the quality factor of the resonances and in turn to increase the sensitivity of the sensor, Rotaru et al. [20] accustomed X-shaped resonators. X-resonators consist of two dipole-like structures connected in mid-section, (the left and the right side on the X-Y plane in Figure 5-2). InChapter 7, it is shown that the quality factor of the metamaterial using X-resonators can be higher than the quality factors of metamaterials with split ring resonators as inclusions.

The material for the resonators is made of gold, which is a non-magnetic metal with a high conductivity.

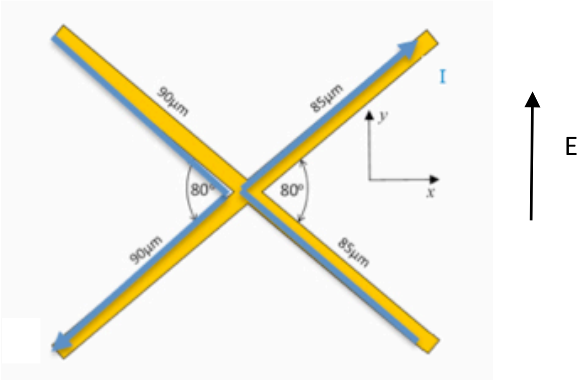

Figure 5-2 The specification of the X structure size are given as: length of the left half: 180 µm, right half 170 µm, the angle of separation for each half 80 degrees, the width and the thickness of each arm 5 and 0.4 µm, respectively. The currents induced on the two unequal sides of the structure are inequivalent, almost equal in amplitude and 180 degree out of phase).

Several resonant frequencies for DNA are reported between 0.4THz and 1.2 THz [5, 6, 85]. To be able to detect these resonances, the metamaterial must produce a resonance in the mentioned frequency range.

The structure acts as a half-wavelength dipole. Each half of the resonator (left and right in the Figure 5-2), with the lengths of around λ/2, produce a resonance at the midsection of the intended frequency range (at around 0.8 THz), because its physical length (L) is close to half the wavelength at the frequency of interest (Equation 1.2). If both halves of the X-resonator are the same length and resonate at the same resonance frequency, the two symmetric currents would cancel one another and the result is a flat frequency response Figure 5-3 (a).

Recent studies, report that by introducing asymmetry to the structure of the resonator it is possible to achieve a higher quality factor by having two resonances occur close to one another and giving rise to a trapped-mode resonance (the space between the two resonances) [17].

For the X-resonator, to achieve two resonances, with two asymmetric currents that would not cancel out each other, (Figure 5-2) the left half is kept slightly longer than the right side(180 µm vs 170 µm), two asymmetric currents are induced, resulting in two different resonances that occur very close to one another. The space between these resonances produces a trapped-mode resonance. This only happens if the Electric field is polarized in the direction orthogonal to the mirror line of the resonator, in this case, in line with the Y-axis (Figure 5-2).

By observing the reflection plot in Figure 5-3 (a), it is noticeable that the trapped-mode resonance of the asymmetric structure, would be sensitive to very small changes in the frequency response compared to the single resonance of the symmetric structure. Also, if the study is concerned with the transmission results, Figure 5-3 (b) shows that, an asymmetric structure adds a second peak to the frequency response, which makes the total of 2 peaks. This way, for sensing, there are three main factors to compare when changes take place in the frequency response.

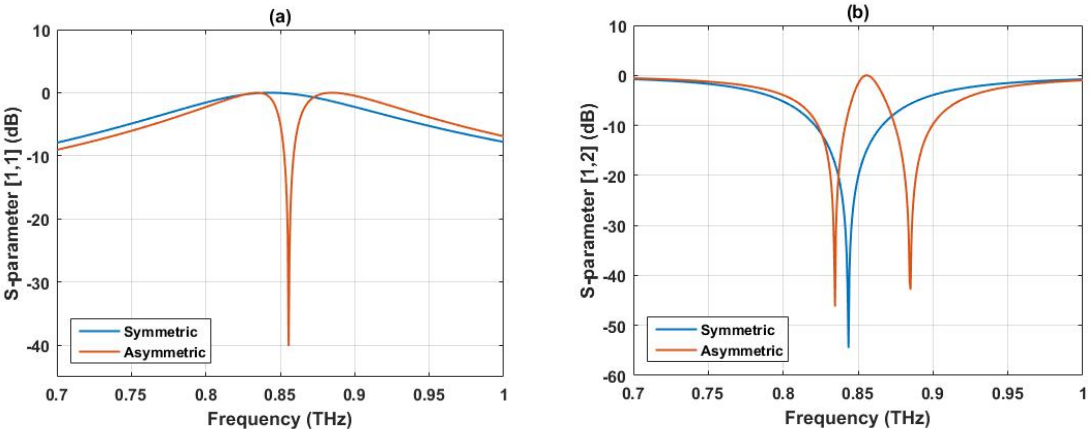

Figure 5-3 Symmetric vs Asymmetric X-resonators frequency response. (a) Reflection (b) Transmission

## 5.2 Simulating the metamaterial

CST microwave studio has a special section for simulating metamaterials. Where the user specifies the geometry of one metamaterial inclusion and the desired spacing between the inclusions. Afterwards CST, generates an infinite array of the inclusions in the direction of the periodicity (in this case, X and Y directions).

The X geometry is modelled on the X-Y plane with the characteristics of: length of the left side: 180 µm, right side 170µm, angle of separation for each half 80 degrees, the width of each arm 5 µm and 0.4 µm thickness (Figure 5-2). As the proper substrate for the sensor under study would be chosen later, for now the substrate is assumed to be vacuum with relative permittivity and permeability of unity, to prevent any unaccounted for effects on the frequency response of the resonator.

Each inclusion is set to be 110µm apart from the neighbouring inclusion, from the centre of the inclusion, in X and Y directions, with the boundary condition at X and Y set as periodic. Floquet ports are added to the model on the X_Y plane, with port 1 at z=110µm and port 2 at z=-110µm.

Since the model is linear, frequency domain solver is chosen as the study step for the computation of the frequency response of the system. The excitation signal is a Gaussian pulse, 0.012(ns) in width, for the frequency range of (0.6-1.2THz).

The frequencies are sampled over the 0.6-1.2 THz range (1001 samples) and can be visualised by plotting the scattering parameters over frequency (Figure 5-4).

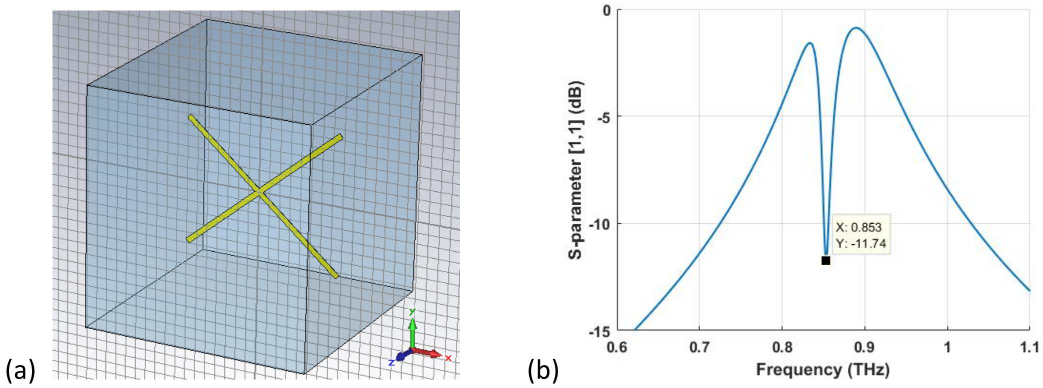

Figure 5-4 (a) a single cell of the metamaterial (b) the Scattering parameter from port1 back to port 1. The resonant frequency of the structure has taken place at 0.853 THz, which is inside the desired frequency range.

### 5.2.1 **Mesh properties**

The model uses a normal sized tetrahedral mesh. To make sure that the X-resonators are properly discretized, a maximum mesh step width is set to 1 µm, 10 µm and 0.5 µm in X, Y and Z directions, respectively. This means that for example, in the Z direction the mesh size for the X-resonator would not exceed 0.5 µm.

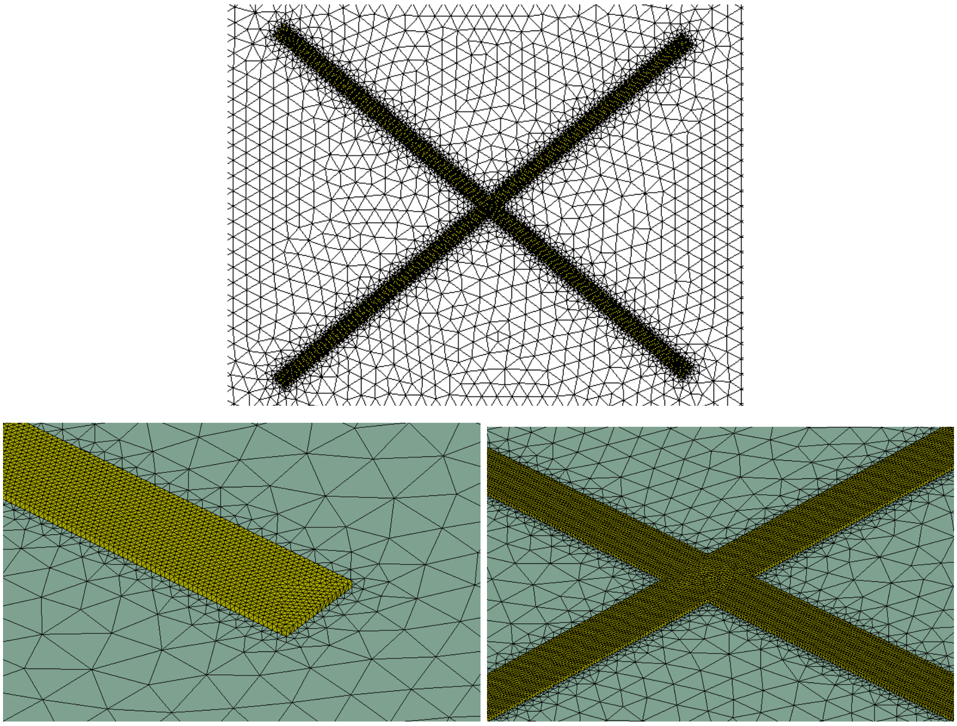

Figure 5-5 Mesh view of the X-resonator is shown

To reduce the possibility of distortion of the mesh, during the simulation, the mesh is adapted to the centre frequency of the working frequency band (in this case 0.85 THz). The wavelength of the centre frequency is sampled at a rate of at least 10 mesh cells per wavelength for the X-resonator. For the background, the rate is, at least one mesh cell per wavelength. This minimises the chances of numerical dispersion.

The solver is repeated and each time the adaptive mesh refinement, detects the changes with respect to the previous simulation and changes the mesh density based on the shape of the structure, which usually refines the mesh around the edges of the structure, inside and outside of the shape (Figure 5-5). This insures a better matched mesh for a specific model, adapting mesh to the physics, which helps the linearization of the calculations. After each solution, an estimated error is calculated at the adapted frequency, subsequently the mesh is refined where the estimated error is the highest. This is repeated until the convergence conditions are met.

The convergence criteria for each solution is set to pass at least three times until the convergence could be considered met. The convergence criteria for the S-parameter is set as “Delta S”. Delta S, is the highest deviance of the absolute value of the difference between the S-parameters of two subsequent passes.

### 5.2.2 **Material properties**

Setting the right material properties in the simulation plays an important role, making sure that the simulation results represent the experimental, real life results. The wrong material properties can lead to achieving wrong scattering parameter results, and deviation from the reality. For this, it is important to find the frequency dependent permittivity and refractive index of materials in the targeted frequency range either through calculation or extraction from the experimental data and set it as the material properties in the simulation.

Next, to find the best composition of the resonator for achieving the highest selectivity and sensitivity, different physical variations of the X shape are investigated.

## 5.3 Simulation for different configuration of metamaterial inclusions

Here, the sensitivity analysis for different configuration of the X-shaped resonators is discussed.

To investigate the best configuration of the X-resonator that gives rise to the highest quality factor, within the frequency range of interest, different aspects of the shape of the X structure has been varied and analysed. Assuming that the material for resonators is gold, suspended in vacuum.

To be able to vary different aspects of the X-resonator shape and configuration, a basic set of parameters is set, to be able to vary the parameters one at a time and read the changes in the frequency response, based on only one varied parameter.

There are a number of parameters related to the shape of the resonators that might affect the resonant frequency of the metamaterial. Different angles between the arms of each half of the X-structure, the Length of the arms, the size of the asymmetry in the resonator, the width of the arms and last but not least the thickness of the resonators.

The models, are simulated in CST Microwave studio suite. The quality factor for each model is calculated to put a figure on the capability of the model to focus the electromagnetic field and to differentiate between the models.

The tables, comprising the quality factor, bandwidth and the resonant frequency for each parameter is available in Appendix A.

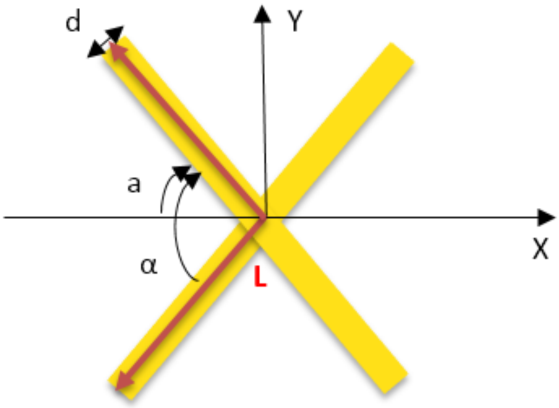

Figure 5-6 Diagram of the X-resonator. “a” is the value of the angle in degrees in respect to the X-axis. “d” is the width of the resonator arms and “L” is the length of the half of the resonator (Figure 5-2)

## 5.3.1 Angle effect over the “X” resonator response

In the current model, the separation angle between the two arms of the resonator in each half is assumed to be 80 degree (Figure 5-7). To investigate the effect of different angles on the resonant frequency, angles of 2 to 179 were tested.

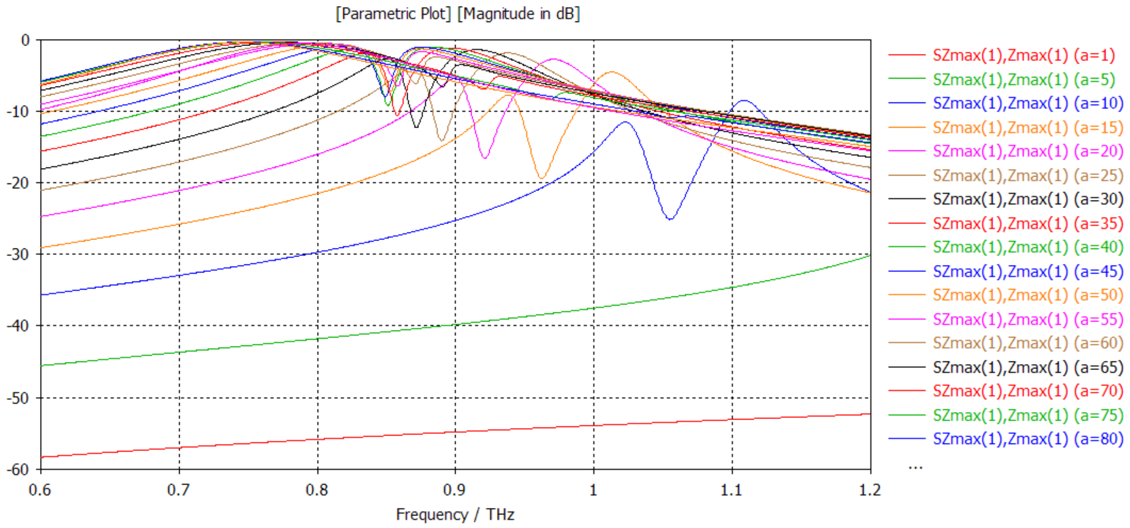

Figure 5-7 Magnitude of S11 for the different angles between 2<α<179 degrees. (a= α /2)

The quality factor $Q_{factor} = \frac{f_0}{\Delta f}$ for each angle is obtained from dividing the peak of frequency of resonance ($f_0$) by the bandwidth of S-parameter curve at half power, 3dB of the peak, ($\Delta f$) for every model (Figure 5-8). (The trapped mode resonance for α> 120 occurred outside the intended frequency range, hence, not included)

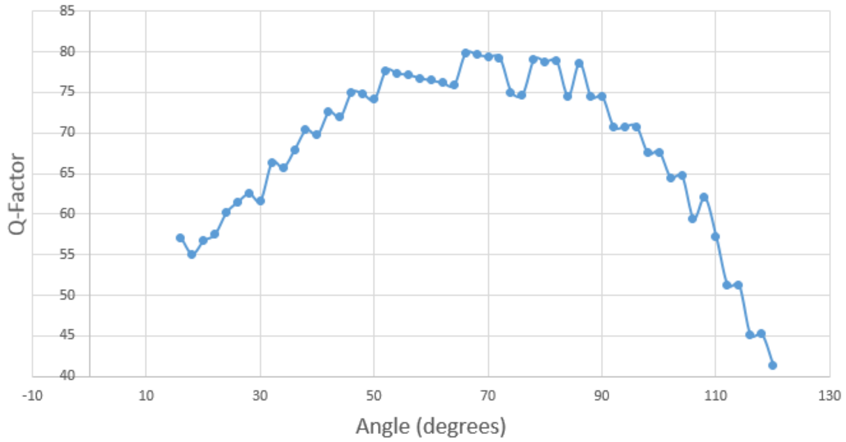

Figure 5-8 Quality factor plot for the different angles between the arms of X-resonator

Consequently, to rule out the effect of the resonance frequency, assuming that all of the resonances happen at one single frequency, the bandwidths at 3dB is compared. This way, it can be understood which X-resonator produces the narrowest resonance at 3dB. As long as the frequency is within the 0.6-1.0 THz bandwidth, the outcome is relevant.

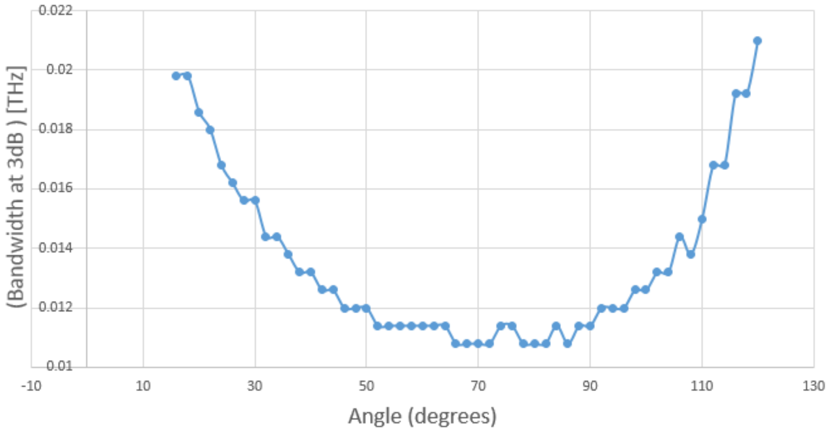

Figure 5-9 Bandwidth for the different angles between the arms of X-resonator

The bandwidths for the angles between 50 and 80 degrees seems to be the lowest, indicating a narrower resonance, hence higher selectivity.

### 5.3.2 The arm length variation effect of the "X" resonator response

The effects of asymmetry and how the length differences between the halves of the resonator can change the quality factor was tested.

The Q-factor, band width (*Δf*) and peak of resonance ($f_0$) for the difference (*ΔL*) of 2 to 37 µm is available in Appendix A. (The trapped mode resonance for 6 µm < *ΔL* < 74µm occurred outside of the intended frequency range, hence, not included)

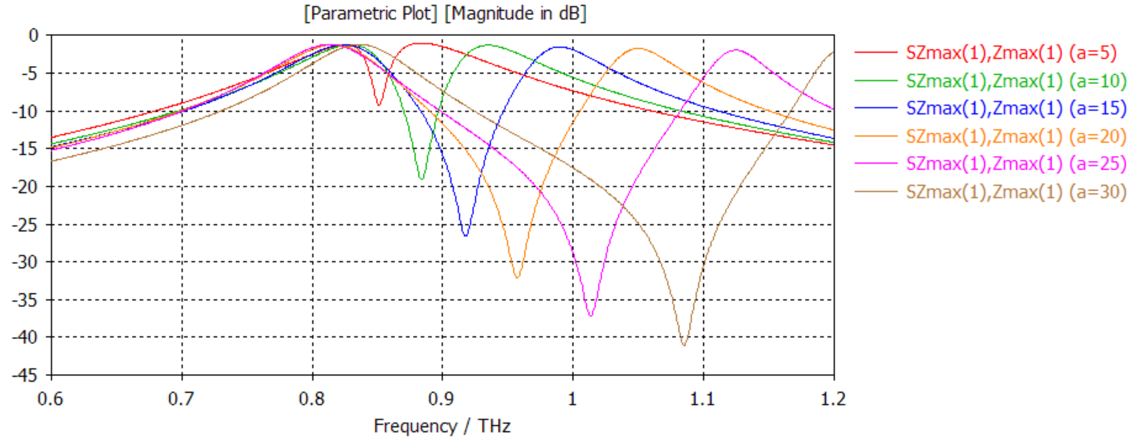

Figure 5-10 The S-parameter (S11) Graph for different length-differences between the halves of the X-resonator (*a* in the legend represents half the size of *ΔL*)

The Quality factor increases when the difference between the lengths of the halves of the resonator is increased (Figure 5-11). The quality factor of the trapped-mode resonance is calculated at the 3db of the full power. Looking at the bandwidth (Figure 5-11), at *10< (ΔL) [µm] <30* range, the bandwidth looks consistent. So in the stage of fabrication, achieving a (*ΔL ≈ L/18*), would make sure on getting bandwidth consistent with minor fluctuations.

However, looking at the bandwidth of the trapped-mode resonances at lower magnitudes, it is visible that the bandwidth is increasingly becoming larger. Later in Chapter 7, it is explained that by increasing the asymmetry between the two halves of the X-resonator the two resonances that contribute to the trapped-mode resonance become further apart, resulting in a widen trapped-mode resonance.

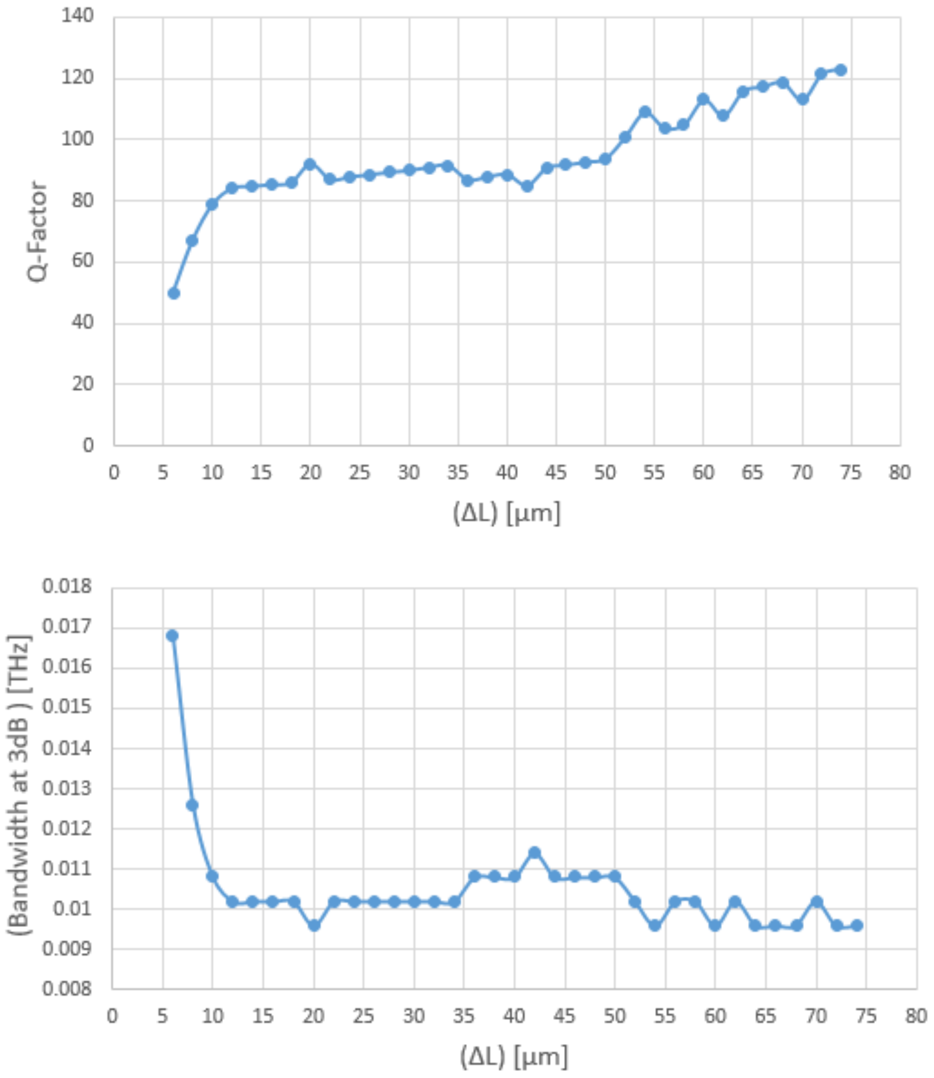

Figure 5-11 Quality factor and Bandwidth plot for the difference between the lengths of the X-resonator halves.

### 5.3.3 Length of each half of the X-resonator

In this section, the effect of the different length of the halves of the resonator on sensitivity of the device is studied (Figure 5-12).

To keep a steady outcome, and keeping the asymmetry consistent, for different lengths of the half of the X, the left half was kept 1/18 longer than the other. This way $L_1$ (the length of the left half of the resonator) is increased from 130 to 240 µm and the length of the $L_2$ (the length of the left half of the resonator) is increased from 123 to 226 µm.

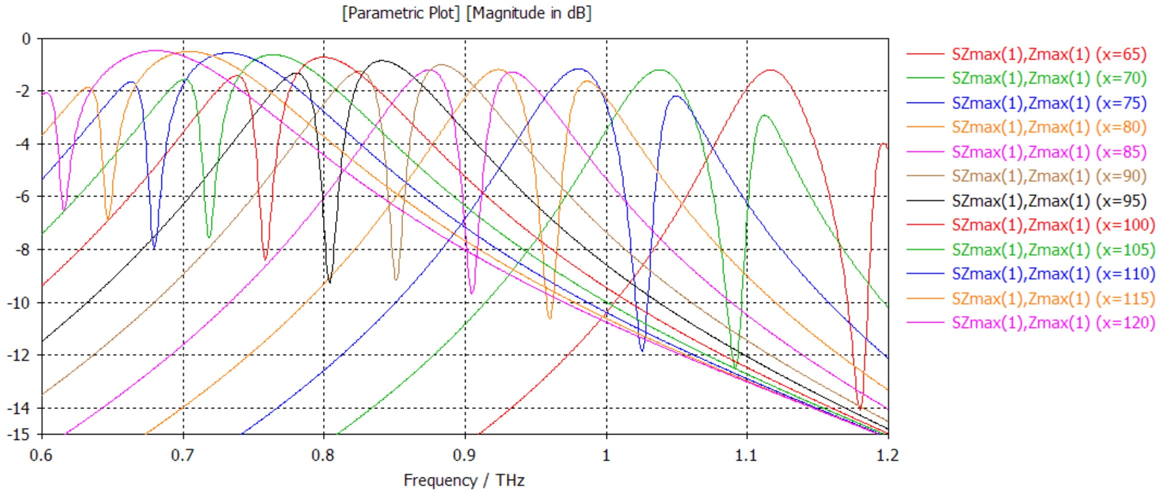

Figure 5-12 Magnitude of S11 variation with the length of the left side ($L_1$) of the X-resonator increasing from 130 to 240 µm. (The x in the legend represents $L_1/2$)

The bandwidth, resonant frequency and the Q-factor is measured.

For different length of X-resonator halves, by comparing the Q-factors (Figure 5-13), it is visible that shorter arms produce higher Q-factor.

To overlook the effect of the resonant frequency on the selectivity of the resonance, the bandwidth graph is plotted (Figure 5-13). The bandwidth is proving to be consistent for 170<L<200.

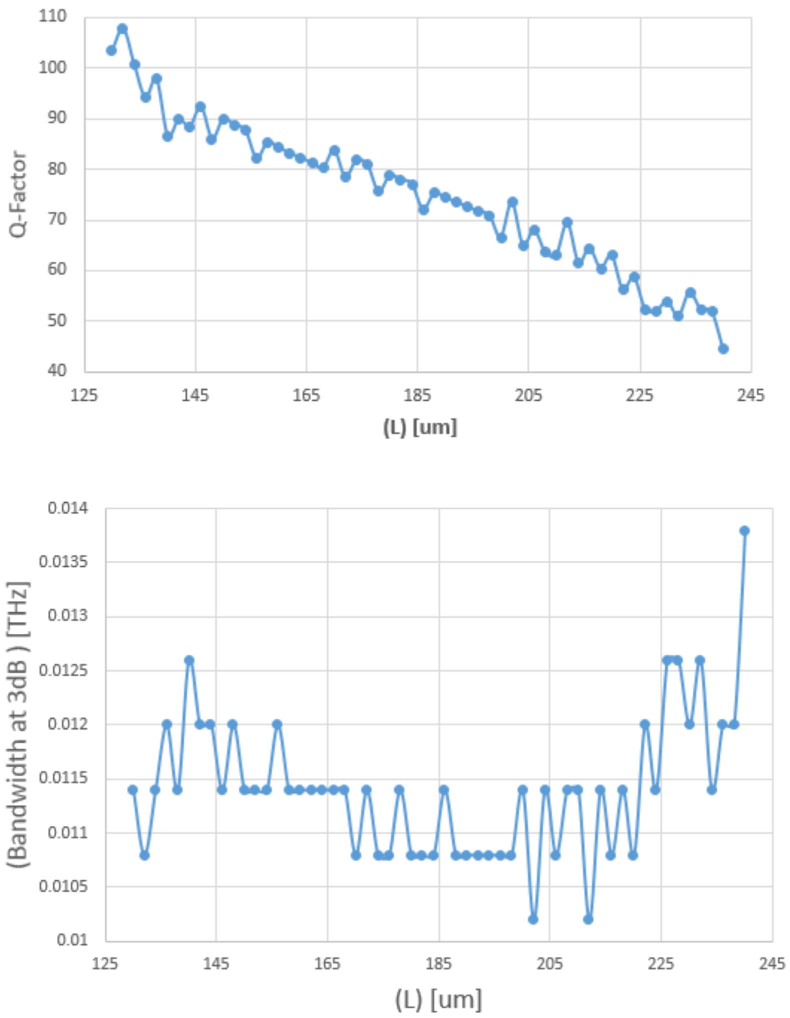

Figure 5-13 Quality factor and the Bandwidth of the metamaterial for different Length of the X-resonator halves.

### 5.3.4 Different width of X-resonator arms

Originally, the width of the arms of the X-resonator is set to be 5 µm.

The structure with different width were simulated (Figure 5-14). The quality factor of the resonance for the widths over 110 µm was zero as their resonant frequency is smaller than 3 decibels.

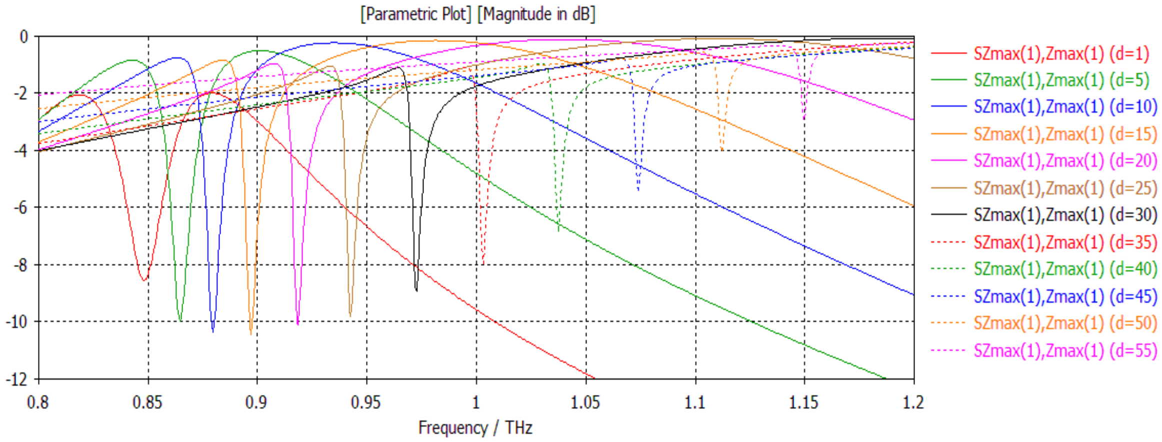

Figure 5-14 Magnitude of S11 shown for the width of arms (d) increasing from 2 to 110 µm. d, in the legend represents half the width of the X-resonator arms.

The quality factor (Figure 5-15) seems to be highest for the width between 30 and 80 µm and decreases when the ratio between width and length of the resonator becomes lower than ~1.12. As the resistance is inversely proportional to the cross section of the conductor, for wider arms, the resistance is smaller hence less loss, and subsequently deeper resonances are expected.

Although, the quality factor increases by increasing the width of the resonator, peak of the resonance becomes lower (according to Figure 5-14). This can be problematic if the dynamic range and signal to noise ratio (SNR) of the frequency response is low.

The Bandwidth at 3 dB (Figure 5-15), is consistent and at its lowest for widths of 10 to 90 µm.

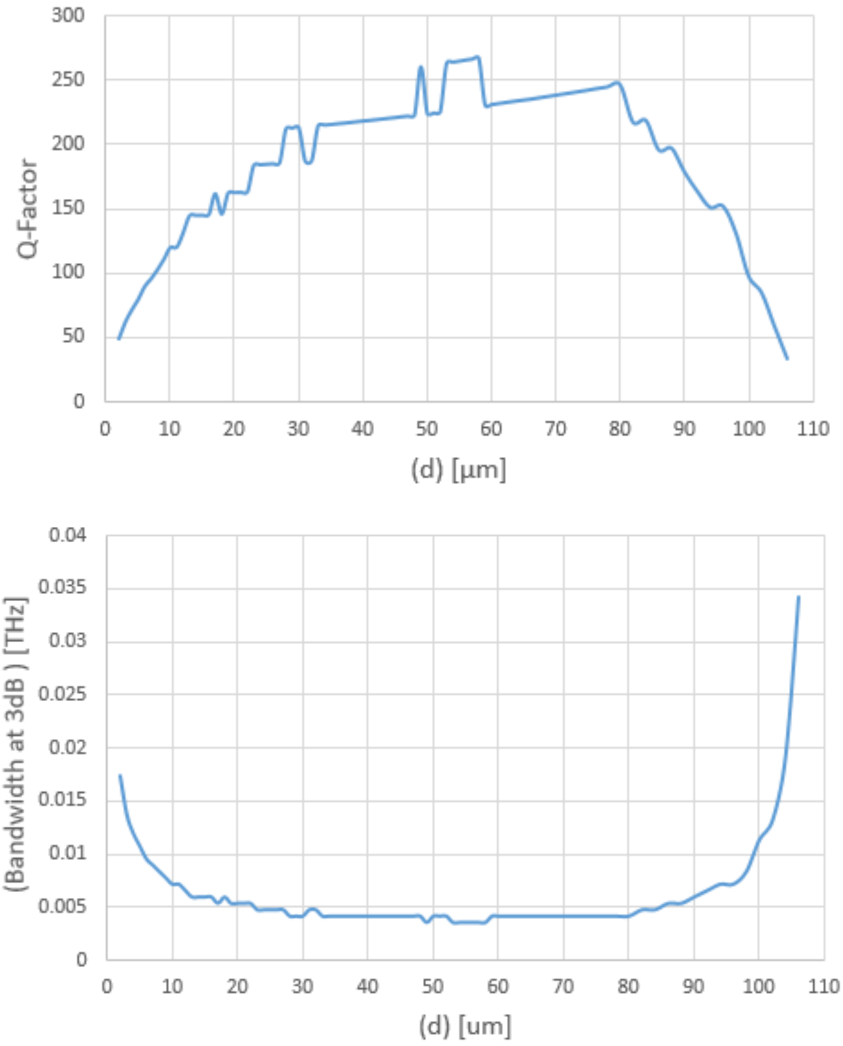

Figure 5-15 Quality factor and the Bandwidth of the metamaterial for the different widths of the X-resonator arms.

### 5.3.5 Different thickness for the X resonator

Originally, the thickness of the arms of the X-resonator is set to be 0.4 µm. The structure with different widths were simulated.

To increase the sensitivity of the simulation to the different thicknesses of the X-resonator, the maximum mesh step width was decreased from 0.5 µm to 0.1 µm in the Z-axis. This way the program can compensate for the low increase rate in the thickness of the model, by increasing the mesh volume.

As shown in Figure 5-16, changes in the thickness of the resonators does not seem to change the shape and the quality factor of the resonant frequency considerably.

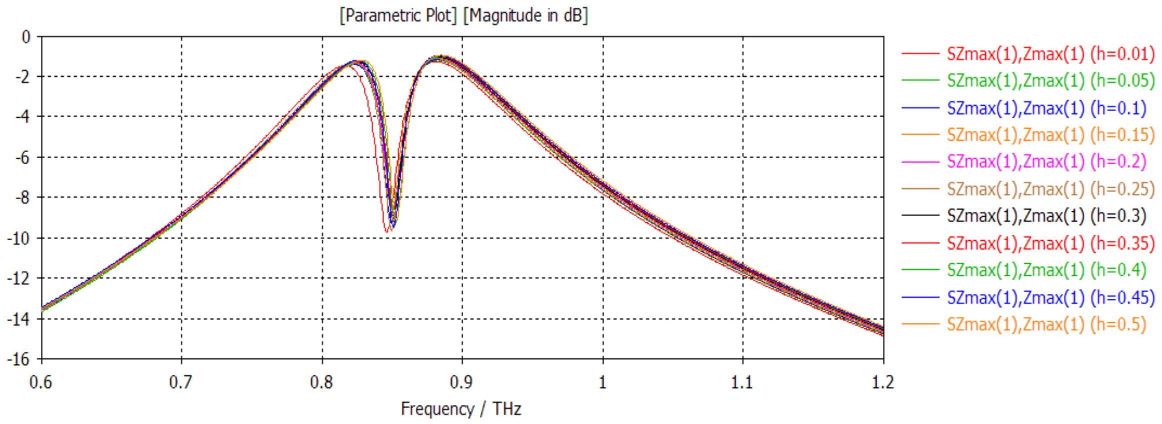

Figure 5-16 Magnitude of S11 is shown for the thicknesses of X-resonators (h) increasing from 0.01 to 0.5 µm.

Figure 5-17 shows the quality factor and bandwidth for different thicknesses of the X-resonators (0.01-5µm). The bandwidth has only dropped from 0.01 to 0.014 (µm) by increasing the thickness of the resonators, which is not precisely distinguishable. The increase in the thickness of the resonator is not comparable to the size of the structure. As a result, the characteristics of the trapped-mode resonance and its Q-factor, change in a very slow rate, close to none.

Also, in the THz region (0.6-1.2THZ), the skin depth of gold is between 0.0972 µm and 0.0688 µm. As a result the signal cannot penetrate gold for thicknesses higher than the skin depth, hence not much change would occur in the frequency response. The slight increase in the magnitude of the resonances by increasing the thickness of the gold layer is due to reduction of the resistance of the resonator because of the thicker gold layer.

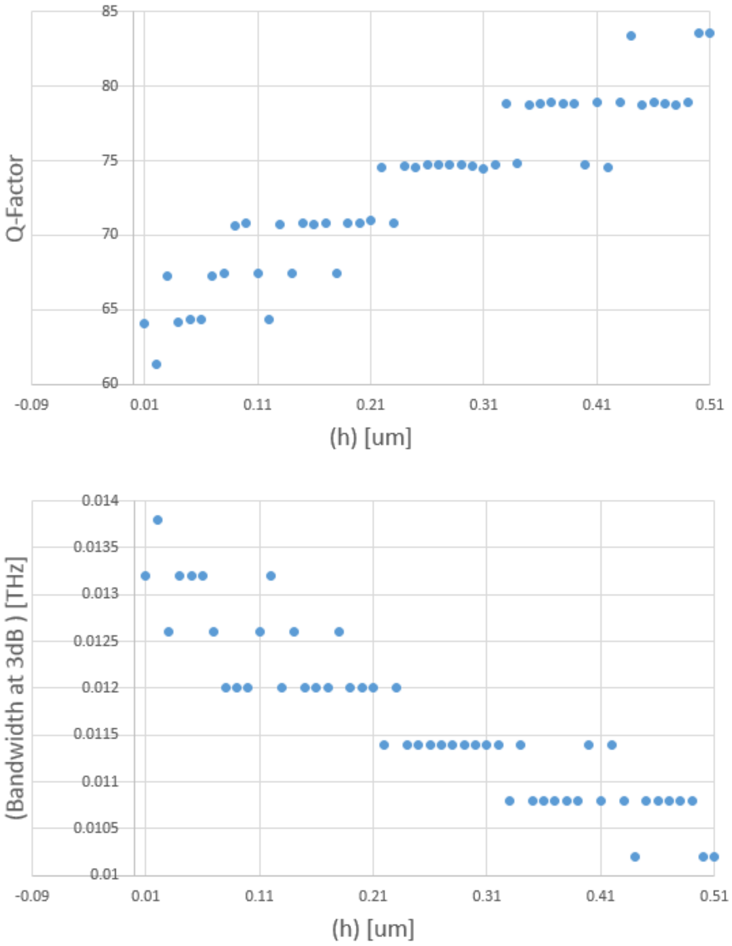

Figure 5-17 Quality factor and the Bandwidth of the metamaterial for different thicknesses of the X-resonators.

Next, the practicality of the device is examined by introducing substrate to the model with information on the types of substrates and their model behaviour, followed by simulation of the metamaterials with different substrate materials. Substrate is usually a semiconductor or an electrical insulator, used as a base for wide range of applications such as ICs (integrated circuits). A suitable substrate would ideally be loss-free, not affecting the frequency response of the model. Keeping in mind that the fabrication requirements restrict the choice of the substrate material.

## 5.4 **Substrates (wafers)**

In Microelectromechanical systems (MEMS) and Nanoelectromechanical systems (NEMS), substrate (wafer) is usually a base for metal deposition [86].

A substrate material cut into discs are called wafers. Wafers are typically cut and polished flat forms of the order of 1 to 3 mm thickness and circular diameters between 25 and 450 mm.

A key factor for the design and simulation in this project is to investigate the substrates which could be used in practical devices and then to choose a substrate with a high transparency to EM waves in the THz frequency range or with a grain size ~ twenty times smaller than the wave length of the incident wave, where the scattering is negligible [87].

## 5.5 **Substrate material**

Usually substrates are made of silicon, polymer, glass or other insulating materials, depending on the application.

For this study, Silicon, A glass substrate (quartz) and a polymer substrate (Cyclic Olefin Copolymer) were studied and simulated as possible candidates. To mimic the material properties of the simulated substrates, a material model of each substrate was made using the permittivity, electric conductivity, and the density of the material.

### 5.5.1 **Silicon Substrates**

Silicon is widely used as a substrate for optical devices as it is a semiconductor and its electrical conductivity can be controlled by doping. Also, silicon being an abundant element on earth, makes it affordable and hence more sought after. Silicon is also, available in the university cleanroom, as it is commonly used in microfabrication, microsystems, MEMs and metamaterials, which makes fabrication straightforward.

The challenge is to develop a model structure with a similar trapped mode resonant frequency spectra as vacuum. However, silicon is highly polarizable (dielectric constant around 12) in THz region and would considerably attenuate the frequency response of the system. To visualise how introducing silicon as the substrate to the metamaterial in this study, can alter the results, silicon wafers of different sizes were modelled.

#### 5.5.1.1 Modelling with silicon substrate

Silicon wafers are commercially available in different thicknesses and diameters. The most common sizes are as shown in Table 5-1:

Table 5-1 Different sizes of widely available silicon wafers [88]

| wafer diameter ($inches$) | 2″ | 3 ″ | 4 ″ | 6 ″ |
|---|---|---|---|---|
| wafer thickness ($\mu m$) | 275 | 375 | 525 | 675 |

The beam size for the measurement device used in Chapter 7 is 1 inch in diameter, so the diameter of the wafer does not play an important role in this design as long as it is larger than 1 inch.

Having the different thicknesses of commercially available silicon in mind, for one metamaterial inclusion, the substrate is modelled as a $110 * 110 * (Different\ Thickness)\ \mu^3$ cuboid and is placed underneath the X-resonator (Figure 5-18).

The first substrate that was introduced to the model is a 6-inch silicon wafer (675 µm-thick) for its ease of commercial access. The model and its frequency response is available in Figure 5-18.

The material properties use to model silicon is as followed: Density of 2330.0 (kg/m$^3$), relative permittivity of 12, relative permeability of 1 and electric conductivity of $2.5\times10^{-4}$ (S/m) [72].

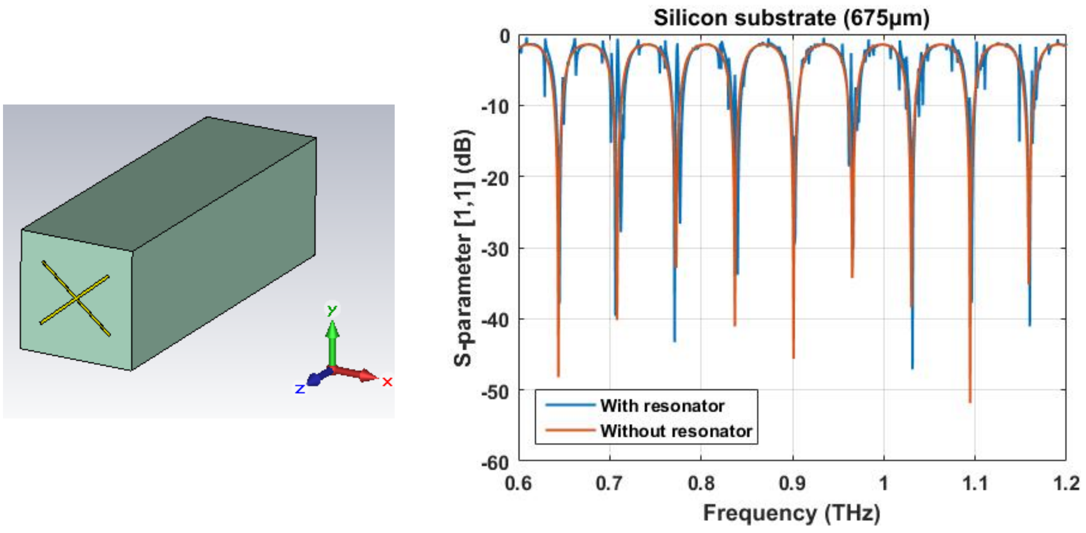

(a) (b)

Figure 5-18 (a) One cell of the metamaterial with a 675µm-thick silicon substrate (b) The graph shows the frequency response for the silicon wafer with and without the X-resonator. The modes as a result of standing waves of silicon are too recurrent in the frequency region of interest.

(a) (b)

Figure 5-18 shows that Silicon as a substrate (without the X-resonator) has large and adjacent dips in the frequency response in THz region as always seen with standing waves. When the structure is modelled with resonators mounted on top of the silicon, superposition of the fields happen due to the currents induced in the arms of the X-resonator and the standing waves within the substrate. Hence, the ideal frequency response is lost.

In order to lessen the effect of the silicon substrate in the frequency response and to eliminate the unwanted modes, thinner slabs of silicon (wafer) may be used. For this reason, the simulation was done again using 525, 375 and 275µm silicon wafers. Results are presented in Figure 5-19.

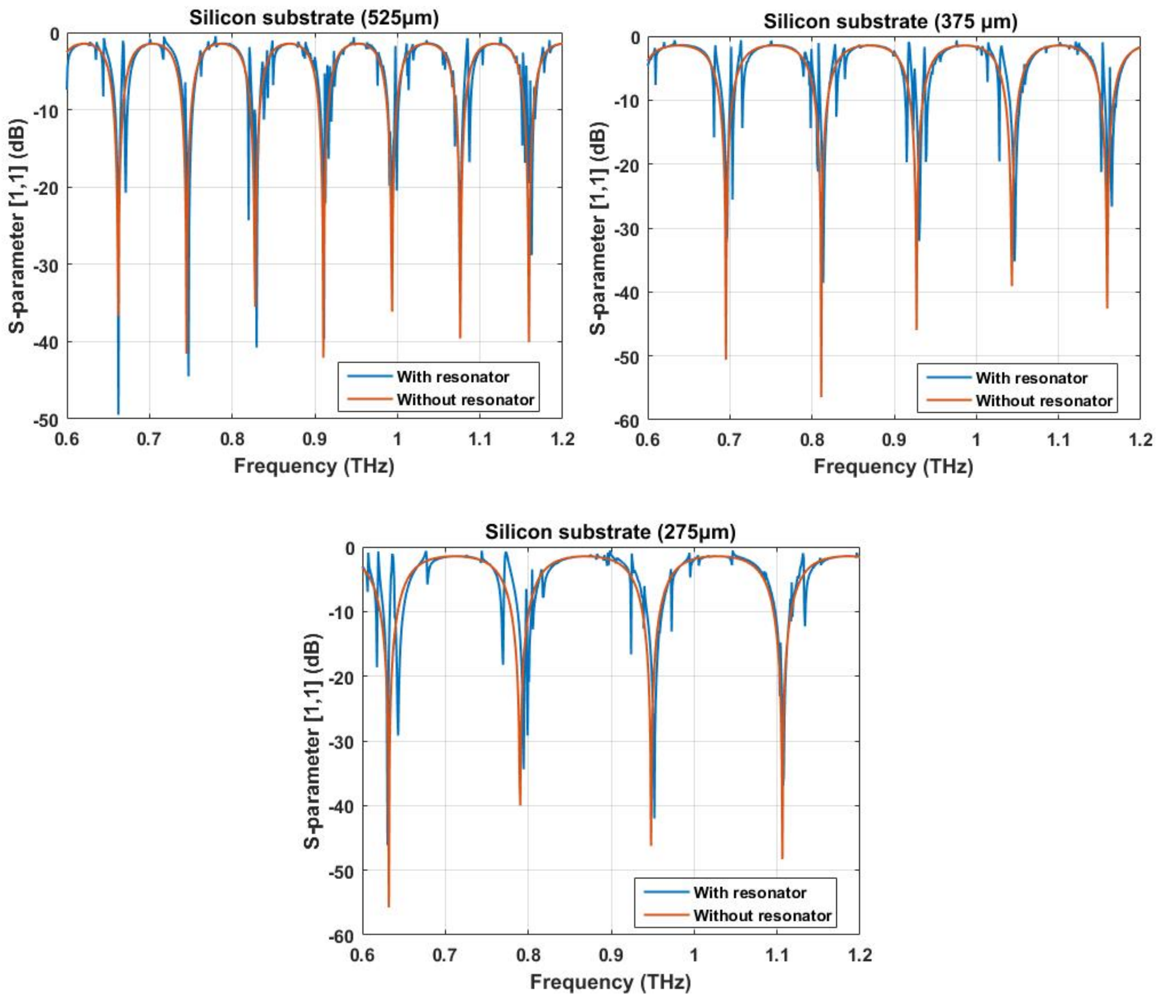

Figure 5-19 Silicon with different thicknesses is used as the substrate in the simulation and the frequency response for each thickness is presented with and without the X-resonator. The frequency response of the substrate shows a steep continuous resonance and the frequency response when a resonator is available shows the same resonance added to the reflections from the resonator.

As it is expected, the results show that by decreasing the thickness of the substrate the absorption and reflection modes from the silicon substrates shift and become wider apart. It can be seen that the less thick the substrate is the less unwanted modes will appear in the frequency region of interest. Therefore, the thinner the wafer, the better for the purposes of our model.

But thinner wafers can be much more expensive than a common 6-inch silicon wafer, with the 2-inch wafer being the most expensive one. Also, the 2-inch wafer, is only one inch larger than the diameter of the beam size used for the spectroscopy, which leaves a very low chance for error in the production.

As a result, the best option seems to be 3-inch silicon wafer (375 µm-thick), which is less expensive than a 2-inch wafer and has a larger diameter and has less prominent standing waves compared to a 6 or a 5-inch silicon wafer.

To try to reduce the change in the frequency response, caused by silicon, it is best to reduce the volume of silicon, to reduce the overall permittivity of the device. This can lead to achieving results as close to the results accessible with vacuum.

Thinner silicon wafers were modelled and showed that only reducing the thickness is not enough.

In order to remove layers from the surface of a substrate for the purpose of thinning the wafer or for introducing a pattern to the surface of the substrate, etching can be done.

One way to reduce the amount of silicon is by etching cubic shapes all the way through each resonator, at the back side of the substrate. This can reduce the amount of substrate material and make less surface contact with the incident rays.

To insure that etching through the silicon would not disturb the positioning of the X-resonators a layer of silicon dioxide (1 micron thickness) is patterned on the silicon surface. It is shown in Figure 5-20 that the silicon dioxide layer doesn’t disturb the frequency response of the X-structure greatly, because of its low permittivity and thickness.

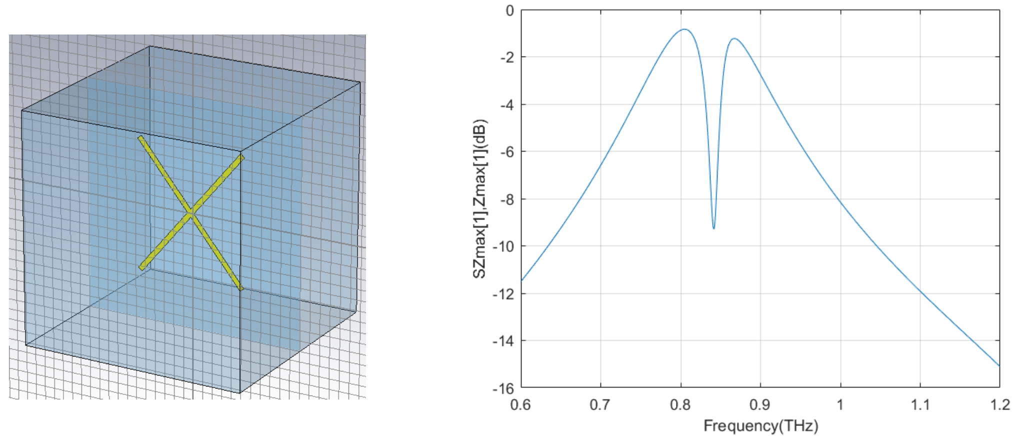

Resonator floating in Vacuum

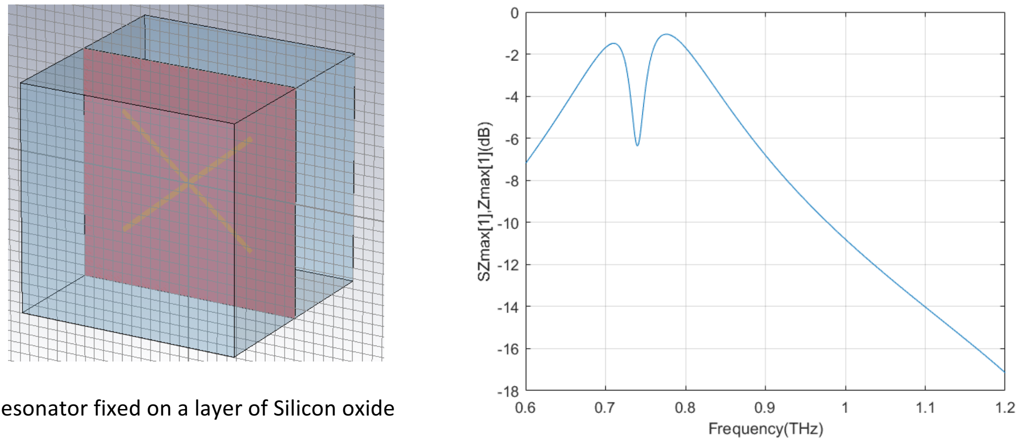

Resonator fixed on a layer of Silicon oxide

Figure 5-20 The difference in the frequency response between the cases where the resonating structure is floating in the Vacuum compared to when it is fixated on a 1µm thick layer of silicon dioxide.

As shown in Figure 5-21, the chosen wafer (375 µm-thick silicon) has gone through different dimensions of etching windows. The size of the first etch is a 40 × 40× 375 $\mu m^3$ cuboid, etched from the back of every inclusion of the metamaterial. The etched window is increased by 80, 100, 120 and 130 cubic micrometres to see the effect on the frequency response.

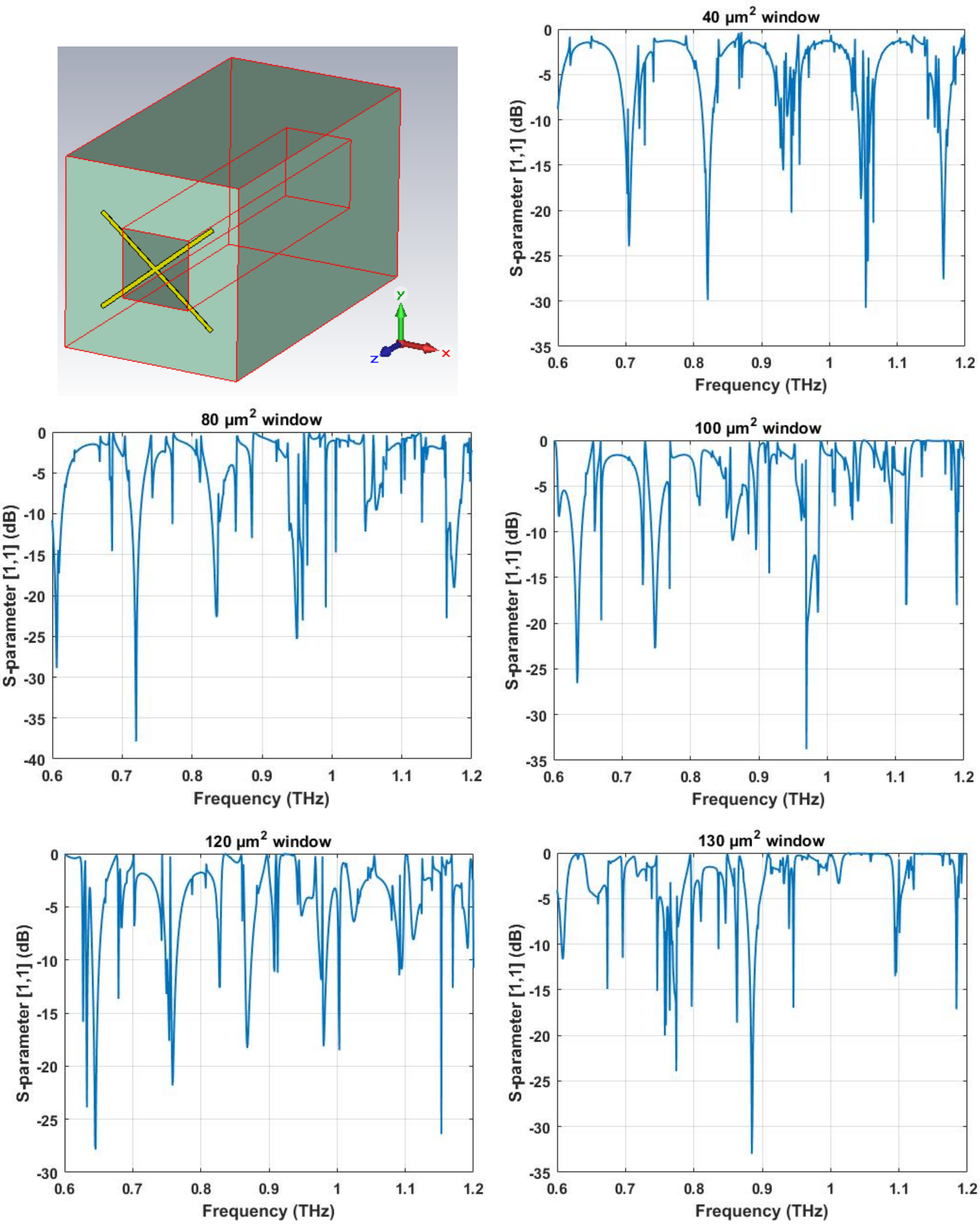

Figure 5-21 The figure on the top left shows a 375 μm-thick Silicon wafer with 40 × 40× 375 μm$^3$ cuboid etch window underneath an X-resonator. The frequency response for different etch window sizes is shown in the graphs.

Etching the substrate affects the positioning and the distance between the nodes of standing waves that arise from the substrate. It also affects the overall mass of the structure, which results in reduction of the permittivity of the substrate. Figure 5-21 shows that by etching through the substrate it is possible to reduce the appearance of the standing waves. The larger the size of the etch window gets, the less apparent the effects of the waveguide structures becomes. However, this reduction of the modes is not very apparent until the etched cuboid is bigger than the size of the X-resonator and increasing the volume of the etching beyond this size will significantly weaken the physical integrity of the structure.

For silicon, even for the largest etch window simulated, the frequency response is a complicated and confusing mixture of responses.

### 5.5.2 **Quartz substrate**

Fused quartz, having amorphous form, does not scatter the incoming electromagnetic wave [87], which is an important factor for microfabrication when a transparent substrate is required. Fused quartz can be made by melting pure quartz (found in nature) or silica sand at 2000°C. [89]

Quartz has a low refractive index (~2) in the THz band [83], with the implication that this is a better candidate to be used as the substrate material compared to silicon in THz applications.

Quartz substrate, similar to silicon, can be commercially found in different diameters and thicknesses. Here for comparison, substrates with the same thicknesses and diameters as silicon are modelled, represented in Figure 5-22.

The material properties use to model quartz is as followed: Density of 2200.0 (kg/m$^3$), relative permittivity of 3.75 and relative permeability of 1.

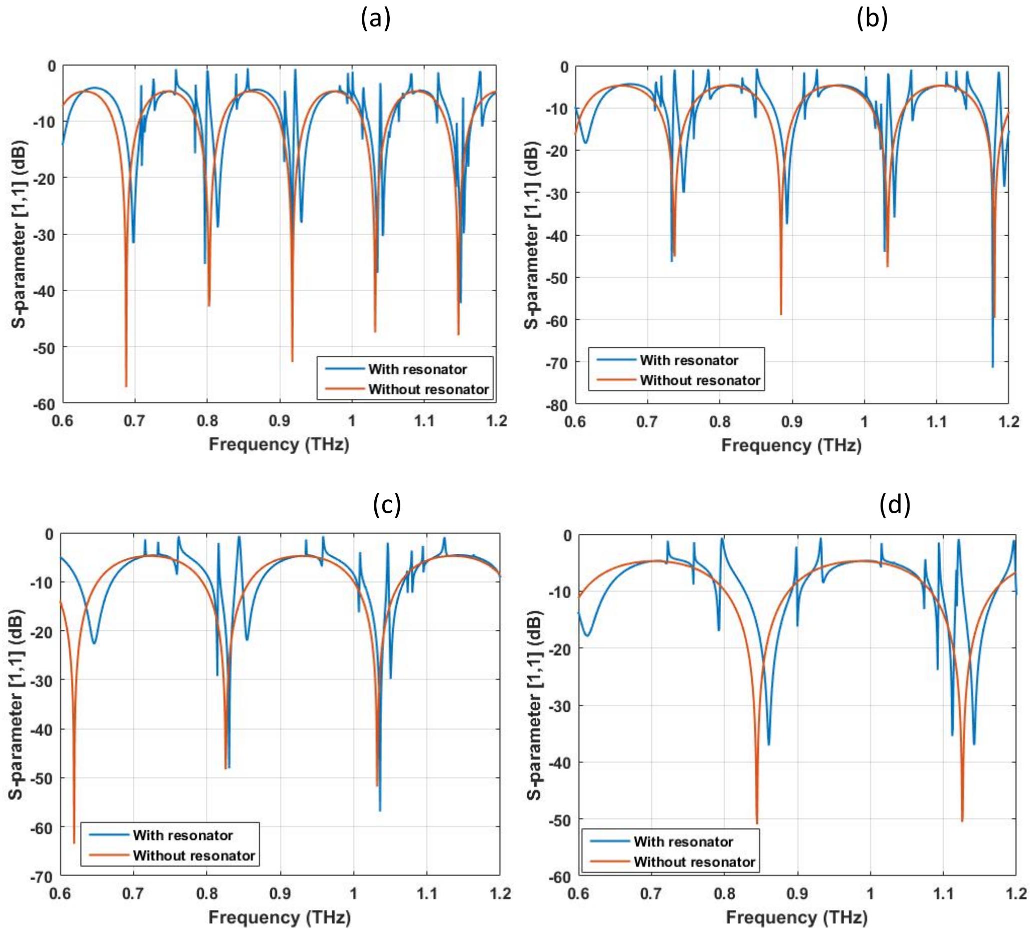

Figure 5-22 Quartz with different thicknesses is used as the substrate in the simulation and the frequency response for each thickness is presented with and without the X-resonator. (a) 675µm-thick quartz wafer substrate, (b)

525µm-thick quartz wafer substrate. (c) 375µm-thick quartz wafer substrate. (d) 275µm-thick quartz wafer substrate.

As shown in Figure 5-22, the frequency response of the substrate shows the modes from the standing waves. When the resonator is added to the model, the superposition of the modes happen. However, the resonant modes from the substrate decrease by using thinner substrates. The same effect happened with silicon but with quartz, the modes are even further apart, which makes it a better candidate for THz applications.

Again, to try to eliminate the effects of standing waves from the substrate, cubic etch, with 100. 110 and 120 µm$^2$ in diameters, is modelled on a 375µm- thick quartz substrate, Figure 5-23.

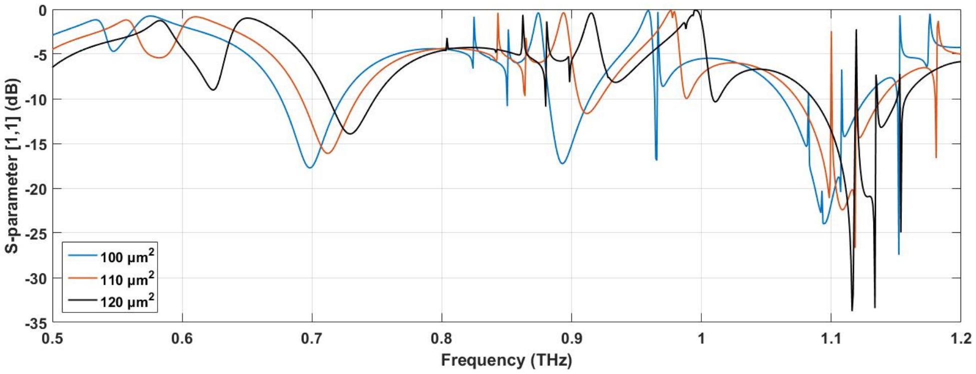

Figure 5-23 375µm-thick Quartz substrate with different size of etching window at the back of the X-resonator is shown.

As seen in Figure 5-23 the bigger the etching window, the less the modes (standing waves) from the substrate is present. However, the results are not reliable and the resonance from the metamaterial is not distinguishable from the unwanted modes until the etching almost the size of the X-resonator is made (Figure 5-24).

In Figure 5-24, the 375µm-thick quartz substrate with a $130\times130\times375\ \mu m^3$ cuboid etch is shown. The standing modes from the substrate are almost disappearing and the trapped-mode resonance of the metamaterial is visible. Still, the trapped-mode is different in magnitude and resonant frequency, compared to the resonance that occurs in vacuum. This is due to the change in the overall dielectric constant of the model after adding the quartz substrate, as the resonant frequency is dependent on the permittivity of the whole model.

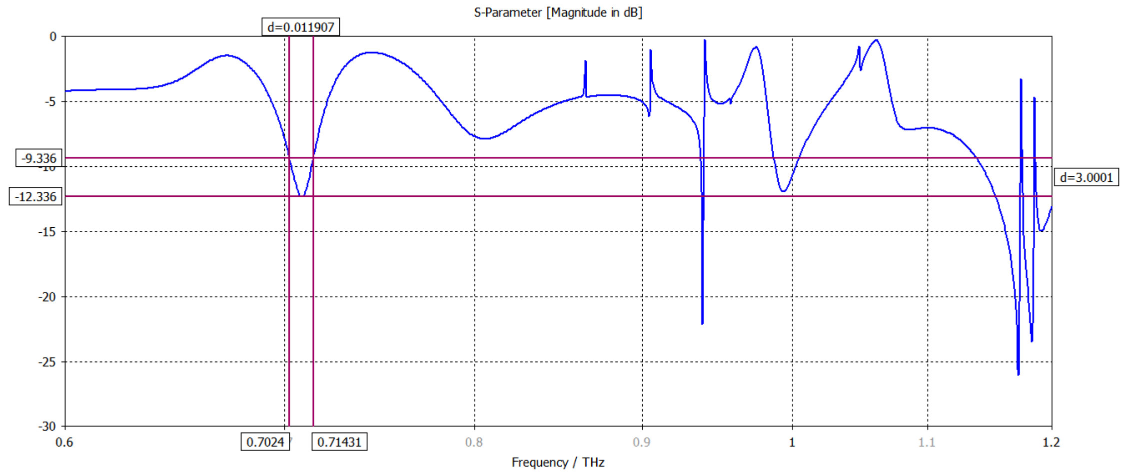

(a) 375µm-thich Quartz substrate with 130 $\mu m^2$ etch underneath each X-resonator, $Q = \frac{0.7086}{0.011907} = 59.5$

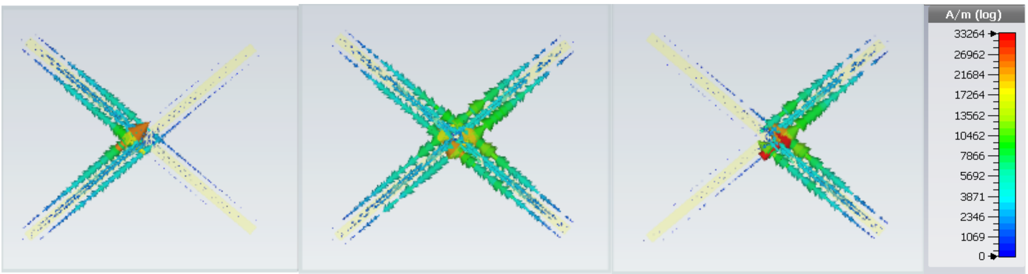

(b1)$F = 0.6724\ THz$ (b2)$F = 0.7086\ THz$ (b3) $F = 0.7321\ THz$

Figure 5-24 the frequency response of the 375µm-thick quartz substrate (a) 375µm-thick quartz wafer substrate with a 140-micron cube etched in the middle of it. (b) Induced currents at the arms of the resonator, before, at and after the resonance.

To check if the resonant mode at $0.7086\ THz$ is the trapped-mode resonance of the metamaterial, the surface current before, at and after the resonant frequency was compared, shown in Figure 5-24 (b). This shows the surface currents on either side of the X-resonator before and after the resonant frequency, confirming the trapped mode resonance.

In Figure 5-25, the 375μm-thick quartz substrate with a $130{\times}130{\times}375\ \mu m^3$ cuboid etch is shown. The standing modes from the substrate are almost disappearing and the trapped-mode resonance of the metamaterial is visible. Still, the trapped-mode is different in magnitude and resonant frequency, compared to the resonance that occurs in vacuum. This is due to the change in the overall dielectric constant of the model after adding the quartz substrate, as the resonant frequency is dependent on the permittivity of the whole model.

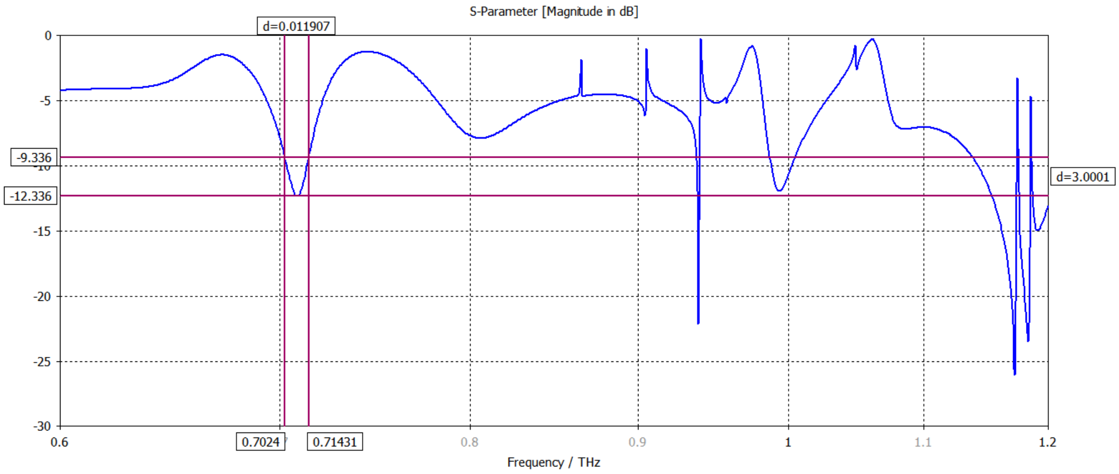

(a) 375μm-thich Quartz substrate with 130 $\mu m^2$ etch underneath each X-resonator, $Q = \frac{0.7086}{0.011907} = 59.5$

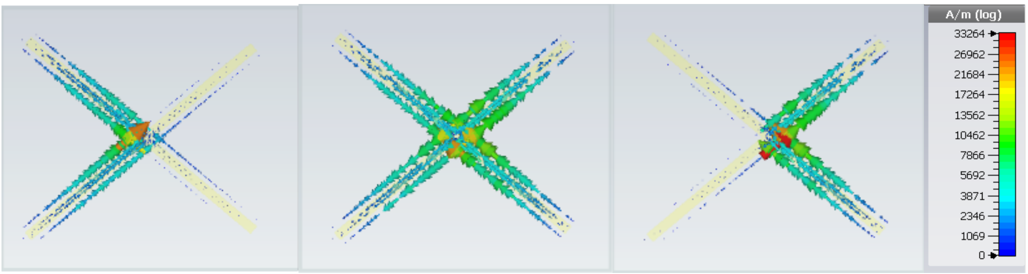

(b1)$F\ = 0.6724\,THz$ (b2)$F = 0.7086\,THz$ (b3) $F = 0.7321\,THz$

Figure 5-25 the frequency response of the 375μm-thick quartz substrate (a) 375μm-thick quartz wafer substrate with a 140-micron cube etched in the middle of it. (b) Induced currents at the arms of the resonator, before, at and after the resonance.

To check if the resonant mode at $0.7086\,THz$ is the trapped-mode resonance of the metamaterial, the surface current before, at and after the resonant frequency was compared, shown in Figure 5-25(b). This shows the surface currents on either side of the X-resonator before and after the resonant frequency, confirming the trapped mode resonance.

### 5.5.3 **Cyclic Olefin Copolymer, COC or Topas Substrate**

Cyclic Olefin Copolymer is a polymer compound that has become popular in MEMS owing to its chemical and physical characteristics. COC, has a chemical resistance to organic polar solvents such as acetone and isopropyl alcohol (IPA) due to its olefinic properties [90]. This makes it a good candidate as a substrate, as in microfabrication usually cleaning and lift-off is done using acetone and IPA.

Compared to the other polymer substrates like Poly Methyl Methacrylate (PMMA), COC has a higher transparency in near UV regions, being completely transparent to light for wavelengths higher than 300 nm [90].

COC, by having a low refractive index of (≈1.52) and low absorption coefficient in the THz region (Figure 5-26), shows low refraction and significantly more transparency to THz rays compared to silicon and quartz [91]. COC also has low electromagnetic losses, but the main advantage of COC compared to silicon and other mainstream substrates is the ability to support direct sputtering, avoiding the use of intermediate materials that encourage adhesion (e.g. chromium). [92]

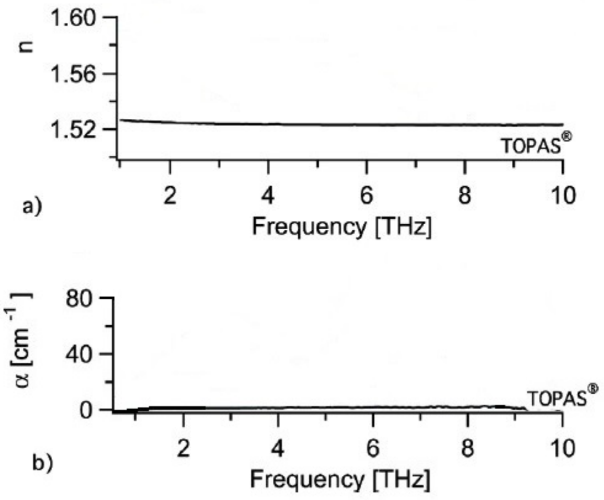

Figure 5-26 (a) Refractive Index of COC (Topas) in THz spectrum b) Absorption coefficient of COC (Topas) in THz spectrum [91]

### 5.5.3.1 COC of different thicknesses

COC substrates come in different sizes compared to Silicon and quartz wafers. However, for the sake of comparison, metamaterials with COC as the substrate were modelled with the same sizes as Silicon and quartz wafers (Figure 5-27).

The material properties use to model COC is as followed: Density of 1200.0 (kg/m$^3$), relative permittivity of 2.31 and relative permeability of 1.

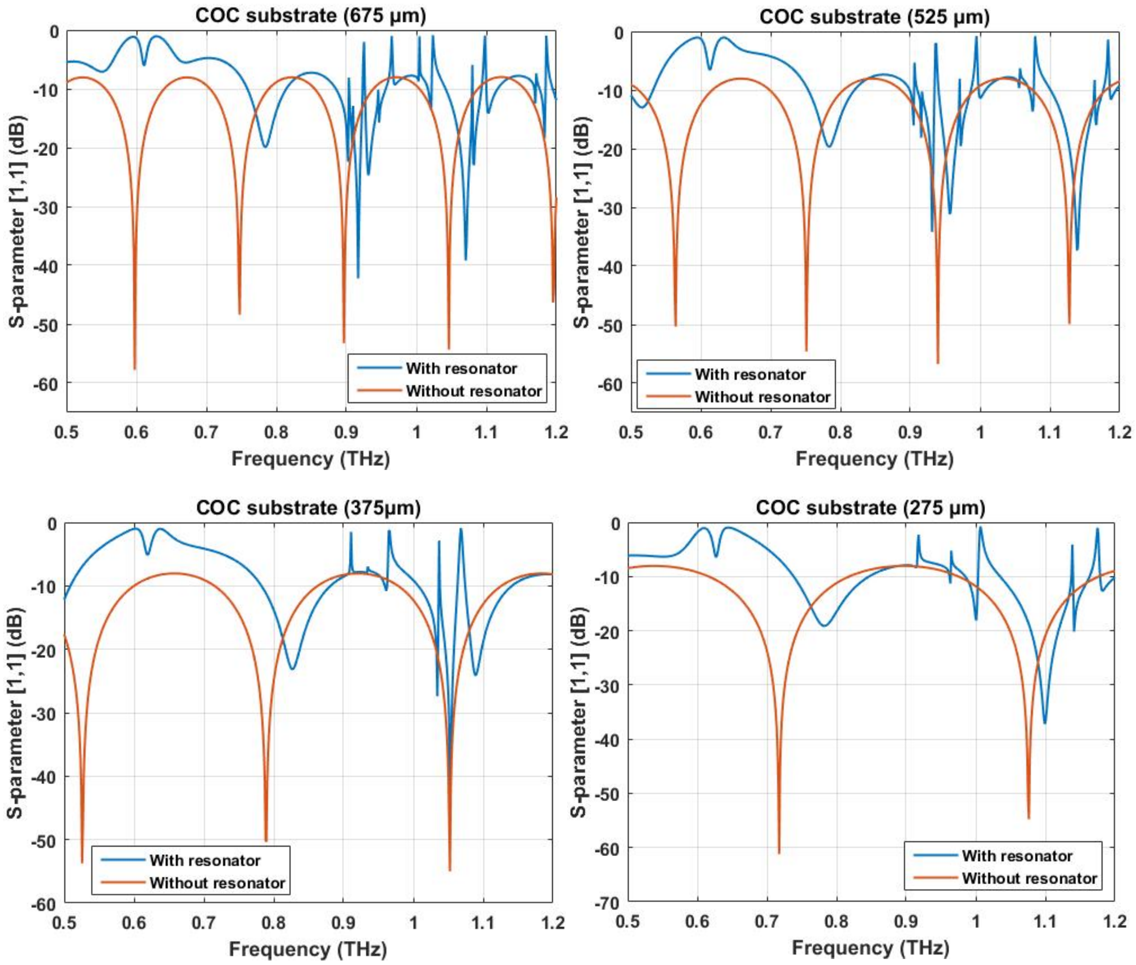

Figure 5-27 COC of different thicknesses is modelled with and without the metamaterial inclusions on top; and the frequency response for each thickness is presented.

As COC has a low refractive index and absorption coefficient in THz, it is almost transparent to THz rays and as is shown in Figure 5-27, no matter how thick the COC substrate is, the resonant mode is visible in all the models at around 0.6 THz. There is a slight shift in the frequency and magnitude of the resonance visible with different thicknesses of the COC substrate, which is as a result of the superposition of the modes from the substrate and the metamaterial.

## 5.6 Summary and discussion

The primary metamaterial with X-shaped resonators was simulated. To find the best configuration of the X shape, a range of different physical properties of the shape such as angle, length and width, was modelled and their trapped-mode resonance was compared.

To quantify the simulation results, different forms of the X-resonator is fabricated and their frequency response is measured in Chapter 6 and Chapter 7, respectively. Because of the fabrication limitations, only four different designs were chosen for fabrication, which are referred to as metamaterial model A, B, C and D throughout the report. Metamaterial A, was chosen because it gives one of the highest quality factors compared to other configurations of the X-resonator. For the other three models, only one physical aspect of the X shape (angle, length or width) was changed in respect to model A.

A. $L_1$= 180µm, $L_2$=170µm, α=80˚, d=10µm

B. $L_1$= 180µm, $L_2$=160µm, α=80 ˚, d=5µm

C. $L_1$= 180µm, $L_2$=170µm, α=80 ˚, d=5µm

D. $L_1$= 180µm, $L_2$=170µm, α=70 ˚, d=5µm

, where $L_1$ is the length of the left half of the resonator, $L_2$= is the length of the right half of the resonator, α is the angle between the two arms of each half and d is the width of the resonator arms, (based on Figure 5-6).

After the analysis without considering the effects of the substrate on the resonate behaviour, to make the model more realistic, the effect of the substrate on the resonance response is considered. For this, different substrates were investigated to find the most proper one for this application.

The metamaterial was simulated with a silicon substrate, as it is widely used in the industry, being accessible and inexpensive. However, because silicon is not transparent in THz region, refraction and reflection of the incident signal will result in several unwanted modes in the frequency response. Consequently, the trapped-mode of the resonator may not be distinguishable from the unwanted modes.

Next, the structure of the metamaterial was simulated on a quartz substrate, which is made of fused quartz and is one of the highly used glass substrates. However, standing waves generated from the interaction of the substrate and the incoming wave, made it unsuitable for this application.

It is possible to etch cubic cut-outs at the back of quartz substrate to eliminate the effects of the standing waves and achieving a better frequency response from the metamaterial.

Finally, for a polymer substrate, COC (also known as Topas) was modelled. COC has a very low refractive index of ≈1.52 in THz region, which makes it a suitable choice for the metamaterial substrate. COC has smaller standing waves compared to silicon and quartz which result in less coupling effect between the substrate and the resonators. This can make COC a better choice of substrate compared to silicon and quartz, even without etching pores on its back.

### 5.6.1 Choosing the optimum substrate based on simulation results

Usually thinner COC substrate (films) have a low transition temperature (around 70 degrees Celsius) which makes them unsuitable to be used for photolithography. Therefore, a 4-inch, 1mm thick substrate from microfluidic ChipShop (© 2005-2018 microfluidic ChipShop GmbH) was chosen as the substrate in this study, which has a glass transition temperature of around 140 degrees.

To achieve an accurate electromagnetic simulation, the refractive index of the COC substrate was measured in frequencies between 0 to 1.2 THz (explained in Chapter 7) and used as the dispersion model in the material properties of COC in the simulation.

The frequency response for the metamaterial on a 1mm-thick COC substrate is shown in Figure 5-28.

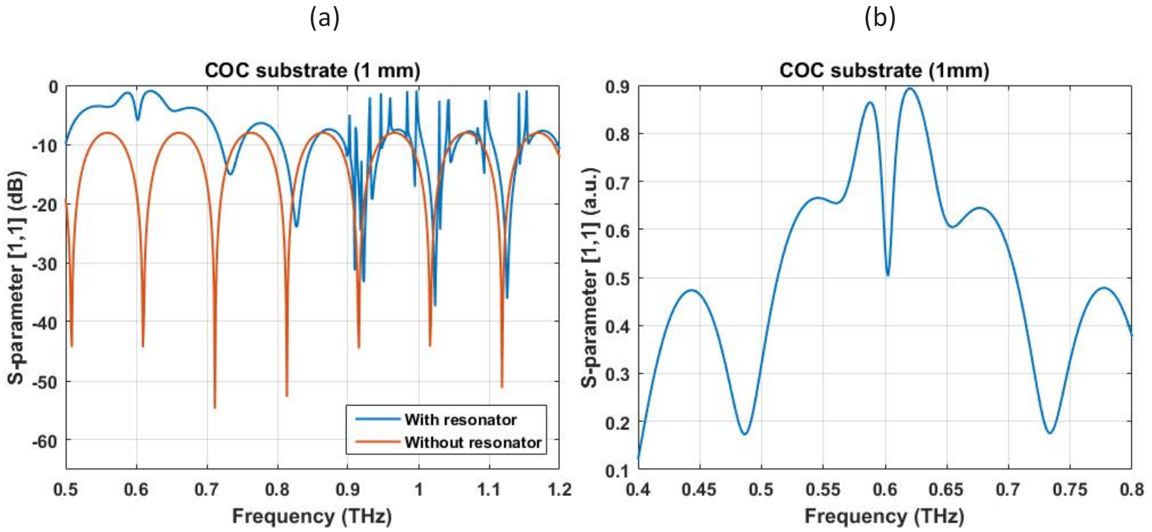

Figure 5-28 the frequency response for the metamaterial on a 1mm-thick COC wafer. (a) Shows the difference in the frequency response of the COC wafer with and without the metamaterial present. (b) Shows the same resonance in arbitrary units (linear) with the Q-factor of 56.8

*Lahiri et al.* [18], reported a quality factor of 20 for a similar optical metamaterial (asymmetric double split ring resonators on a silica substrate), this model with quality factor of ~56, proves to be more sensitive, in detecting small shifts in the frequency response.

# Chapter 6 Fabrication of X-shaped resonators

In Chapter 5, different configurations of the X-resonator, with different angles between the arms, different length of the arms and different width of the arms was explored. To be able to quantify the simulation results and to compare the different simulation results, four of the different X-resonators shapes were picked for fabrication.

For fabrication, the design of the metamaterial that is modelled using computer simulation must be transferred to the substrate. In this study, photolithography is used to imitate the design on the substrate.

The patterns were modelled using **Tanner L-edit** by *©2015 Mentor Graphics Corporation.* Afterwards, the design was sent to a third-party company for fabricating the photomask using Electron-beam lithography.

In this section the fabrication of the prototype sensors and the steps for reaching the final design is explained.

## 6.1 **Photolithography**

Here a bright-field mask is used with chrome patterns on a soda lime glass. With four different metamaterials with X-resonator as inclusions (Figure 6-1), chosen based on the results in section 5.3 of Chapter 5.

The characteristics of the X-resonators for the four metamaterials (A, B, C and D) are as followed:

A. Bottom left design on the mask Metamaterial A ($L_1$= 180µm, $L_2$=170µm, α=80 ˚, d=10µm)
B. Bottom right design on the mask Metamaterial B ($L_1$= 180µm, $L_2$=170µm, α=70 ˚, d=5µm)
C. Top right design on the mask Metamaterial C ($L_1$= 180µm, $L_2$=170µm, α=80 ˚, d=5µm)
D. Top left design on the mask: Metamaterial D ($L_1$= 180µm, $L_2$=160µm, α=80 ˚, d=5µm)

Where $L_1$ is the length of the left half, $L_2$= is the length of the right half, α is the angle between the two arms of each half of the X and d is the width of the X arms, (based on Figure 5-6). For the metamaterials, the inclusions are 110 µm apart from their neighbouring inclusions, from the centre of the resonator in X and Y directions.

Each design resembles a separate metamaterial with different resonators as its inclusion.

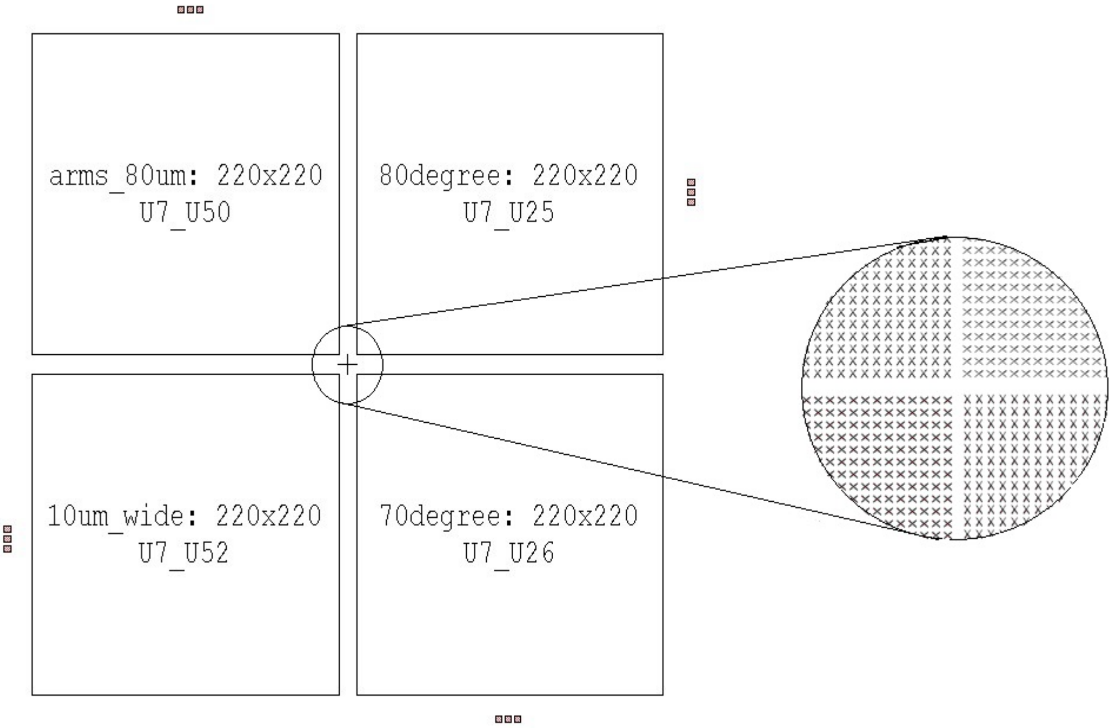

Figure 6-1 The design of the photomask. Comprising four different metamaterials. Bottom left design on the mask is **metamaterial A** with $L_1$= 180µm, $L_2$=170µm, α=80 ˚, d=10µm. Bottom right design on the mask is **metamaterial B** with $L_1$= 180µm, $L_2$=170µm, α=70 ˚, d=5µm. Top right design on the mask is **metamaterial C** with $L_1$= 180µm, $L_2$=170µm, α=80 ˚, d=5µm. Top left design on the mask **is metamaterial D** with $L_1$= 180µm, $L_2$=160µm, α=80 ˚, d=5µm

The wafer used in the fabrication of this sensor is a 4-inch, 1 mm-thick COC (Cyclic Olefin Copolymer) wafer from microfluidic ChipShop (© 2005-2018 microfluidic ChipShop GmbH), commercially known as Topas.

## 6.2 Process Flow

The process flow that was used to fabricate the samples is presented in Table 6-1, followed by the illustration in Figure 6-2.

Table 6-1 Optimized Process details for microfabrication of metamaterials

| **Step Number** | **Process Details** |
|---|---|
| 1 | Ultrasonic cleaning for 15 minutes followed by spin drying |
| 2 | Dehydrating on the hotplate at 110˚c for 180 seconds |
| 3 | Spinning on negative photoresist (AZ2070) with 7 µm thickness |
| 4 | Soft-Baking on the hotplate at 110˚c for 180 seconds |
| 5 | Exposure to UV light using mask aligner for 6.5 seconds |
| 6 | Post exposure bake on the hotplate at 110˚c for 180 seconds |
| 7 | Developing (using AZ726 developer) for 90 seconds |
| 8 | Gold deposition Using LAB700 Evaporator (100 and 350 nms) |
| 9 | Lift off using acetone |

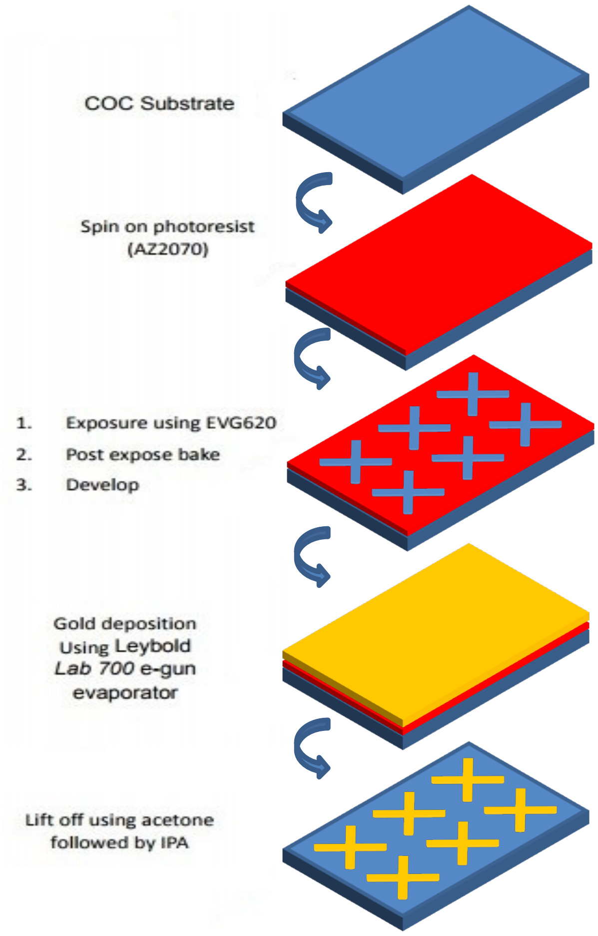

Figure 6-2 Fabrication steps taken during fabrication of the proposed metamaterial

The main challenge in the process flow is to get straight side walls and exact dimensions of the photomask pattern. To achieve this, a mask with simple square patterns (520×520 $\mu m^2$) was used to find out the best timing and temperatures to be used in the process flow, to reach the best fabrication results.

The optical microscopic images of the fabrication results using the preliminary process flow is shown in Figure 6-3. The Figure 6-3 (a) shows the fabricated pattern, which is approximately 60 µm larger in size compared to the pattern on the mask, which could be a sign of over UV exposure. To resolve this, the exposure time was reduced from 7 seconds to 6 seconds. Figure 6-3 (b) shows that side walls of the pattern are not straight, which showed to be as a result of the combination of under exposure and under baking, to resolve this, the exposure time was increased from 6 to 6.5 seconds and the baking time for each step was increased from 60 seconds at 110 °C to 180 seconds at 110 °C. The result is shown in Figure 6-3 (c).

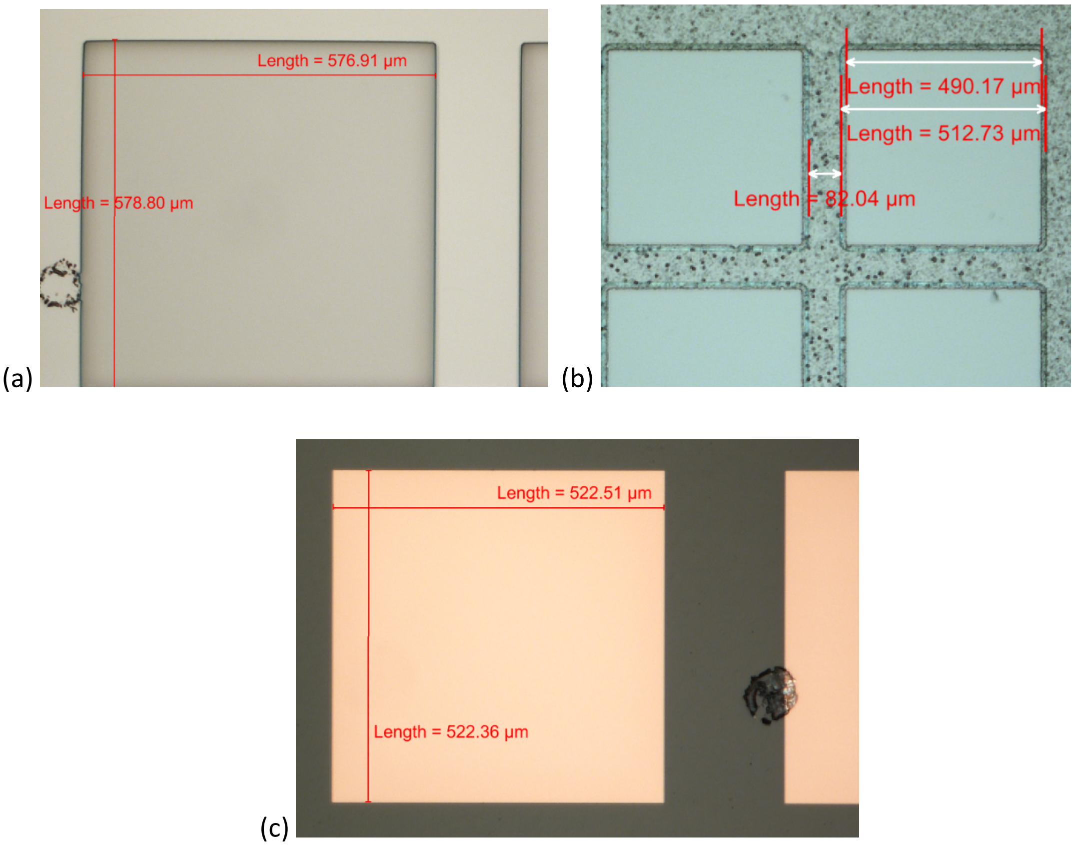

Figure 6-3 Optical microscopic images of the square patterns (520×520 µm$^2$). (a) shows the result of over UV exposure. (b) shows the result of the lack of baking time and also under exposure. (c) is the outcome of optimised process flow.

The optimised process flow is explained in detail in the following sections.

### 6.2.1 Ultrasonic cleaning

In order to clean the wafer of any organic substances, the sonication method was used. The wafer was put in a beaker filled with acetone, in ultrasonic water-bath for 5 minutes. Then the procedure was repeated with IPA (Isopropyl Alcohol) and DI (deionised water) simultaneously for 5 minutes each. (IPA removes Acetone residue and DI water removes IPA residue).

Afterwards, the wafer is spun-dried to dispose of water on the surface of the wafer.

### 6.2.2 Dehydrate

Post cleaning, in order to eliminate any remaining moisture on the wafer and to encourage resist adhesion, the wafer was dehydrated on a hot plate for 180 seconds at 110 °C.

### 6.2.3 Spin on photoresist

In order to transfer the pattern from mask to the wafer, a thin layer of a photosensitive polymer (photoresist) is spun on the wafer. The photoresist is sensitive to UV light which is used to transfer the optical mask pattern on to the wafer, when exposed to UV.

In order to apply the photoresist onto the wafer surface, spinning method (spin coating) is used. The thickness of the resist is dependent on the spinning speed and viscosity of the resist.

As the photomask used here is a bright-field mask, a negative photoresist, AZ nLOF 2070, is used, producing empty X-shaped sections on the wafer when the resist is developed. The resist is spun at 2500 (rpm) for 30 seconds, to achieve uniformity. Achieving, 7 µm thickness.

### 6.2.4 Soft-bake

After spinning the resist, in order to dispose of any remaining solvent, a pre-exposure bake is performed for 180 seconds at 110 ° C on the hot plate.

### 6.2.5 Exposure

For exposure of UV light, the EVG 620TB mask aligner is used.

The exposure is only supposed to react with the photoactive compound of the photoresist, but in negative resists, the base resin will react and absorb the wavelength below 350 nm. To eliminate any absorbance of UV by the resist compound, an I-line filter (365 nm) is used, not to pass wavelengths below 365 nm.

Next, the photomask (5 inch) is inserted using a 5 inch chuck holder into the aligner, then the wafer is inserted using a 4 inch wafer chuck.

Because alignment is not necessary in this case (one layer pattern), a basic zero level alignment is performed. Then the photomask and the wafer were brought to hard contact mode (vacuum contact), and the uncovered sections of the wafer were exposed to UV light.

The optimal exposure time in this work is found to be 6.5 seconds, as the resist is thick and takes time for UV rays to penetrate the underlying layers.

### 6.2.6 Post-exposure bake

For case of AZ2070 after exposing with UV rays it is necessary to post bake the sample to finish the photo-polymerisation process. [93] The post- exposure bake was done on the hot plate for 180 seconds at 110 ° C.

### 6.2.7 Develop

Next the wafer was immersed in a beaker part-filled with AZ 726 developer for 90 seconds to strip the exposed parts. Right after, the wafer is completely washed with DI water to stop the development process, then spun dried. As no etching is done after development in this procedure, hard baking was not necessary.

### 6.2.8 Metal deposition

As gold adheres to the surface of the COC, no adhesion layer is required.

The next step is the metal deposition. Leybold Lab 700 e-gun evaporator was used to deposit gold on the substrate, with the deposition rate of one angstrom per second. To achieve different thicknesses for the X-resonators, two wafers were prepared, one with 0.1µm and one with 0.35µm gold layer (an extra one with 350 nm-tick resonators was prepared for the purposes of Chapter 8).

### 6.2.9 Lift-off

After metal deposition, the same steps as explained in section 6.2.1 sonication, is done to lift off the remaining resist and metal, leaving the X-shaped gold resonators only. This process can be done by leaving the wafer in acetone overnight, to make sure a complete lift off of the unwanted gold is achieved.

## 6.3 Results

As mentioned in 6.2.8, two wafers (0.1µm and one with 0.35µm gold thickness) each comprising of four metamaterial designs, the total of 8 different designs were fabricated. The main concern was to achieve straight sidewalls and an almost exact size of the resonators as on the photomask. This was achieved by adjusting the baking temperature, baking time and the exposure time. For example in this case, if the resonator arms, were wider than expected, it could be fixed by reducing the exposure time. Or where the side walls were faded and devious rather than straight, would be resolved by adjusting the baking and exposure times as explained.

Figure 6-4 shows the optical microscope images of the fabricated metamaterial with $L_1$= 180µm, $L_2$=170µm, α=80µm, d=5µm dimensions for the X-resonator. Figure 6-5 shows a close up of the cells for different dimensions of the X-resonator. These microscopic images confirm a good imitation of the resonators to the ones on the photomask. The length of the fabricated resonators were all ~500 nm smaller than the simulated models, which is a 3% discripency. The thickness of the resonators for the two different models with the intended thickneses of 100 and 350 nms were measured at 101 nm and 358 nm, respectively.

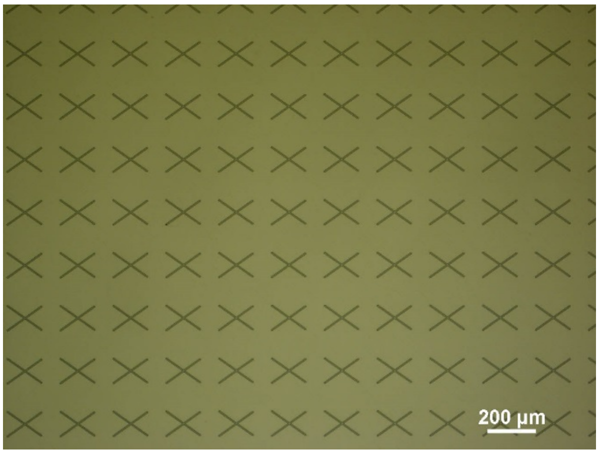

Figure 6-4 Optical microscope image of metamaterial C with $L_1$= 180µm, $L_2$=170µm, α=80µm, d=5µm dimensions of the X-resonator.

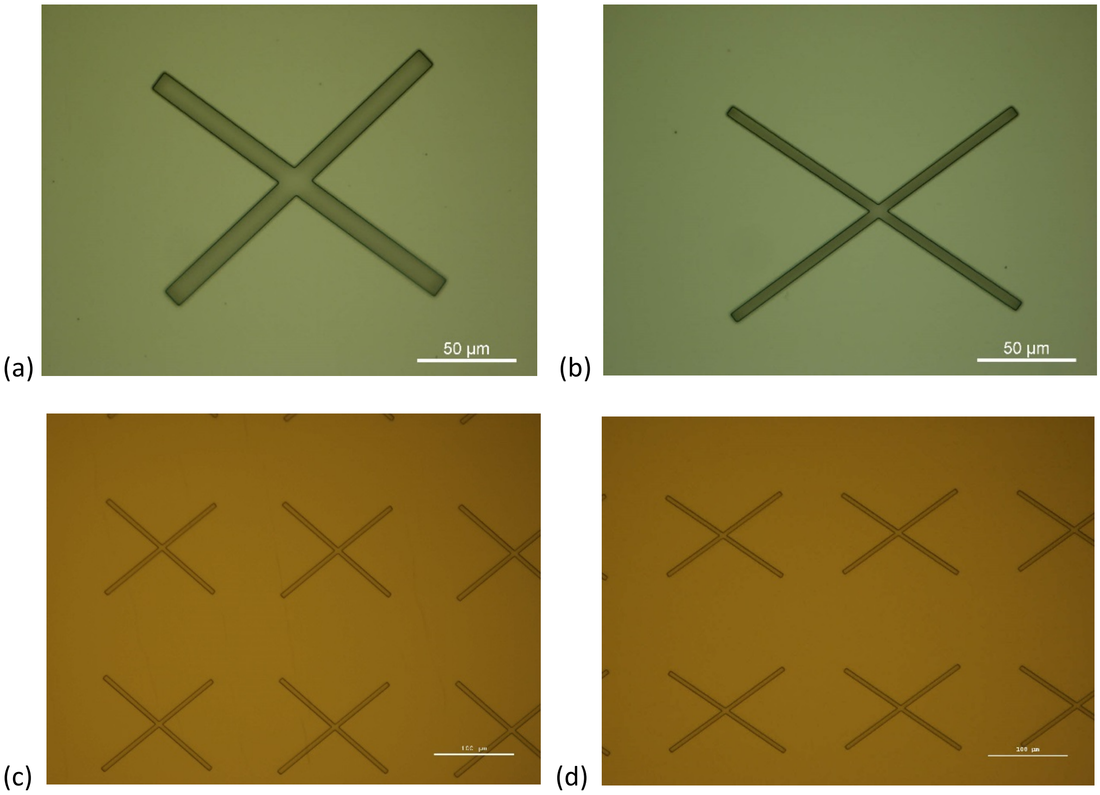

Figure 6-5 Optical microscopic images of the fabricated metamaterials with different dimensions of the X-resonator. (a) Metamaterial A (b) Metamaterial B (c) Metamaterial C (d) Metamaterial D, the resonators in the models are ~500 nm smaller than the simulated models, which is a 3% discrepancy

# Chapter 7 **Measurement (Terahertz-TDS)**

In this chapter, the steps to measure the frequency response of the prepared metamaterial-based sensors are discussed.

Dr Vasilis Apostolopoulos and his team in THz group, University of Southampton, carried out the measurements of the sensors, using Terahertz time-domain Spectroscopy (THz-TDS).

The THz-TDS setup customs a Titanium Sapphire femtosecond (fs) laser with a continuous wave power of approximately 1.2 W. The data is measured over a 50 picosecond range (Time domain) and converted to frequency domain using Fourier Transform.

## 7.1 Experimental measurement results

The experimental setup customs a Titanium Sapphire femtosecond (fs) laser with a continuous wave power of approximately 1.2 W. The data is measured over a 50 picosecond range (Time domain) and converted to frequency domain using Fourier Transform.

According to equation (4.1), the scan frequency resolution ($f_s$) is calculated by reversing the total length of the time domain ($f_s \ = \frac{1}{\Delta T * nfft}$). In this setup, the total length of the time domain is 50 picoseconds, which gives rise to the resolution frequency of 0.01 THz.

The resolution can be increased by artificially increasing the length of the time domain (Figure 7-1). In practice, the data is only measured over a 50 picoseconds range, but then modified to add a large region of zero intensity at the end of the THz pulse. In this case, the resolution is increased to fs= 0.0003 THz, growing by a factor of 100.

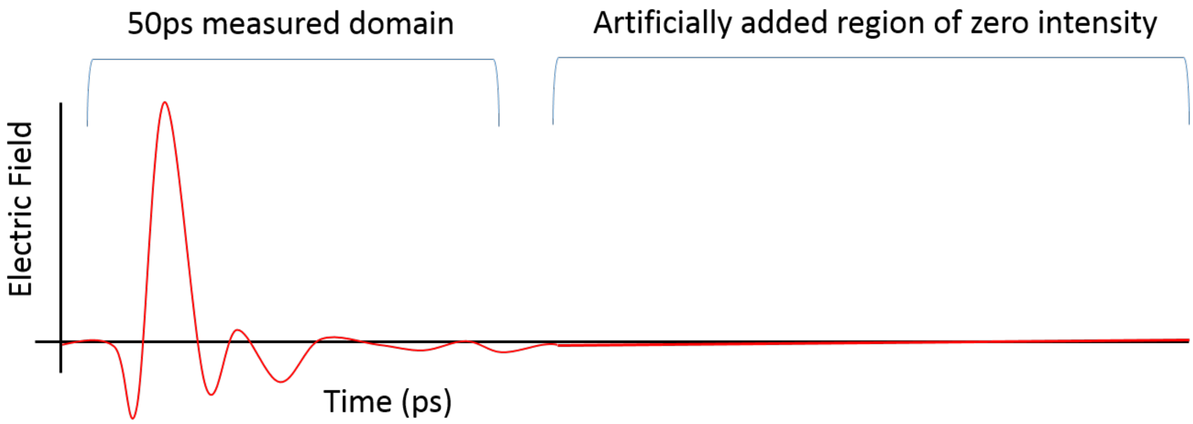

Figure 7-1 zero intensity region, artificially added to the THz pulse.

This only works for the peaks with a frequency width smaller than the 0.01 THz resolution. For peaks with a frequency width higher than the 0.01 THz resolution, the artificial region has only worked to smooth out the data rather than increasing the resolution. Figure 7-2 shows that after the time domain has been artificially extended the data has been smoothed out.

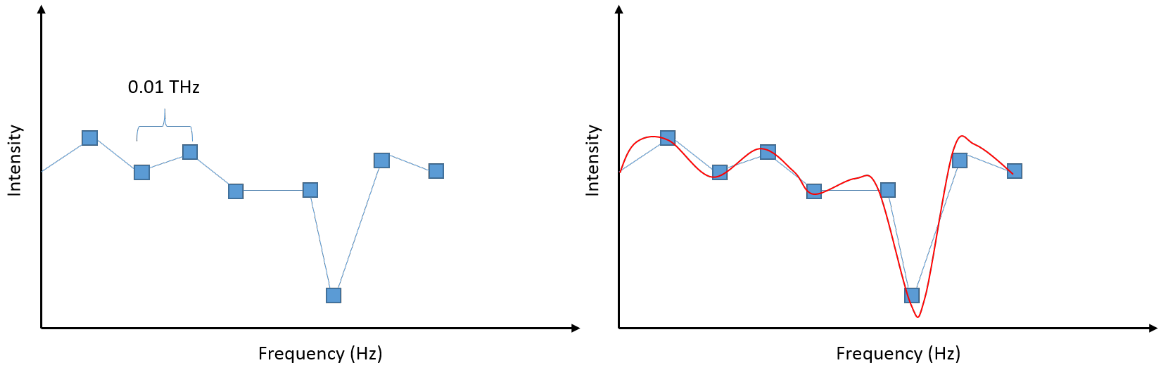

Figure 7-2 the data has been smoothed out by adding the artificial zero intensity region

### 7.1.1 **COC measurements**

The transmitted THz radiation in the air chamber compared to when a 1 mm-thick COC wafer is shown in Figure 7-3.

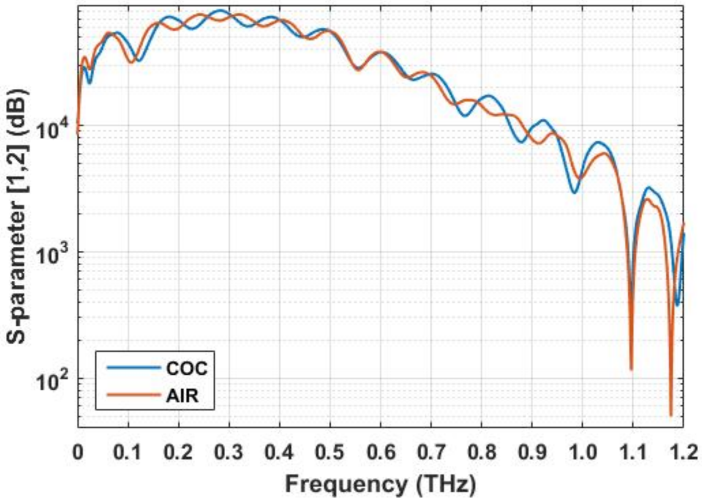

Figure 7-3 THz transmission detected using the Titanium Sapphire femtosecond laser in air chamber versus the transmitted power when a 1 mm-thick COC wafer is present.

The transmitted power of a clean COC wafer was measured to determine the complex refractive index of COC in THz and also is used as the reference in the following measurements. The COC sample changes the THz pulse as shown in Figure 7-4.

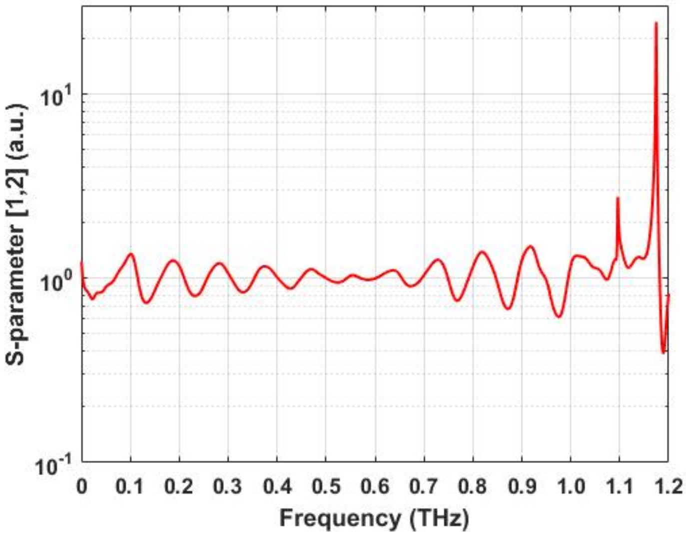

Figure 7-4 Transmission measurement result for 1mm-thick COC wafer in reference to air.

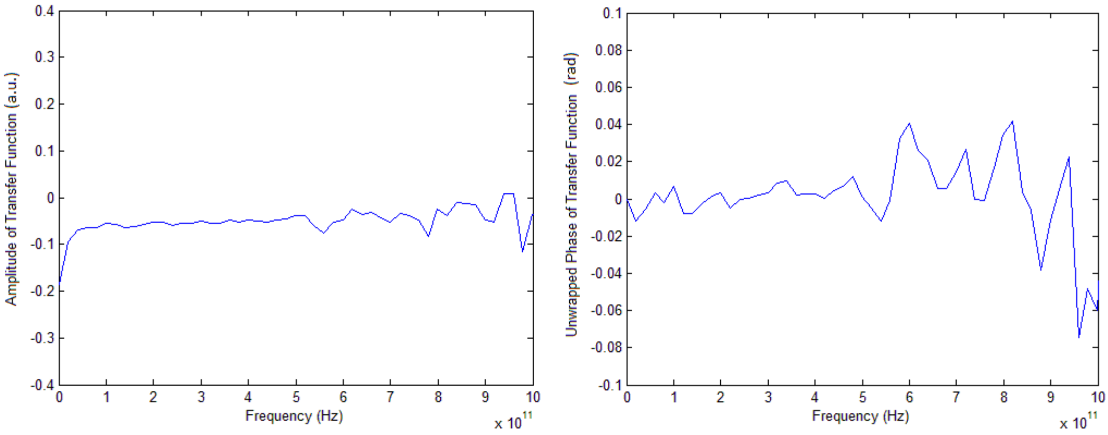

Figure 7-5 Amplitude and phase of the transmitted signal through the 1mm-thick COC sample

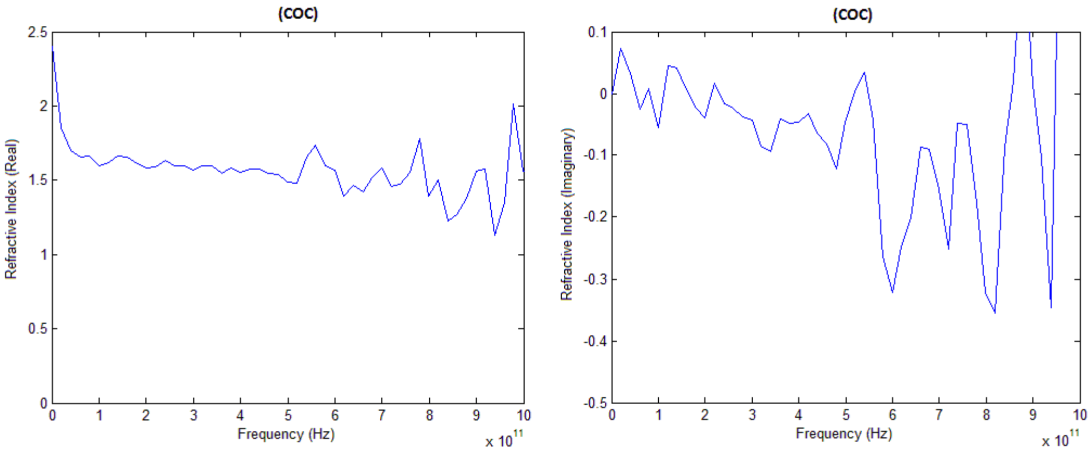

Figure 7-6 Complex refractive index for COC substrate determined experimentally.

The magnitude and phase spectra were calculated using the transfer function, which is the quotient of the Fourier Transformation of time domain signal of the sample (COC) and of the reference (Air). Subsequently, the phase spectra is unwrapped to get a continuous function (Figure 7-5). Next, the complex refractive index is determined using material parameter extraction method by fitting the theoretical transfer function to the experimental transfer function as explained in 4.4.2 (Figure 7-6).

The results show noise at high and low frequencies where the SNR of the THz scans becomes low, due to finite bandwidth. There are also oscillations seen on the frequency response of COC and Air samples, which are a result of the etalon produced by the setup which causes the infinite reflections of the theoretical transfer function.

This refractive index is used to model the dielectric dispersion model of COC in the computer simulation (in Chapter 5), to get a more accurate dielectric model of the material for simulation.

### 7.1.2 Metamaterial measurements

Next, the transmission of the metamaterials were detected.

As explained in 6.3, two wafer were prepared. First one with 100 nm and the second one with 350 nm gold-thick resonators, each comprising of 4 different metamaterials. The metamaterials are referred to as A, B, C and D. The dimensions for the X-resonator (Figure 5-6), of each metamaterial is given below, changing the length of the left ($L_1$) and right ($L_2$) side of the resonator, the angle between the arms (α) and the width of the arms (d), one at a time for each model.

A. $L_1$= 180µm, $L_2$=170µm, α=80˚, d=10µm
B. $L_1$= 180µm, $L_2$=170µm, α=70 ˚, d=5µm
C. $L_1$= 180µm, $L_2$=170µm, α=80 ˚, d=5µm
D. $L_1$= 180µm, $L_2$=160µm, α=80 ˚, d=5µm

The transmission for each model is presented by plotting the magnitude vs. frequency in reference to the reference sample (a COC wafer) in Figure 7-7.

As shown in Figure 7-7, for all of the different metamaterials, the trapped-mode resonance happen at a close range in the expected bandwidth of 0.4 to 1.2 THz. The trapped-mode frequency of resonance ($f_t$) and quality factor for each model is shown in Table 7-1.

Table 7-1 Experimental quality factor and resonant frequency of the trapped-mode resonance of metamaterials, A, B, C and D.

| **Metamaterial model** | | **Model A** | **Model B** | **Model C** | **Model D** |
|---|---|---|---|---|---|
| **100nm-thick resonators** | $F_t$ *(THz)* | 0.664 | 0.6606 | 0.655 | 0.6784 |
| | Q-factor | 49.5 | 31.16 | 50.02 | 12.63 |
| **350nm-thick resonators** | $F_t$ (THz) | 0.664 | 0.6634 | 0.6575 | 0.6818 |
| | Q-factor | 48.12 | 31.29 | 45.57 | 17.22 |

Changing the thickness of the resonators does not seem to have a drastic effect on the shape or quality factor of the trapped-mode resonance. This is due to a very low skin depth of gold (0.0972 µm to 0.0688) in the THz region (0.6-1.2THZ). The thickness seems to mostly affect the amplitude of the resonance, introducing slightly steeper resonances for thicker resonators. This result is in confirmation with the simulation results in section **Error! Reference source not found.Error! ference source not found.** for different thicknesses of the resonators. This is mostly due to the effect of skin depth, having a thicker gold layer reduces the resistance of the resonator, hence the steeper resonance.

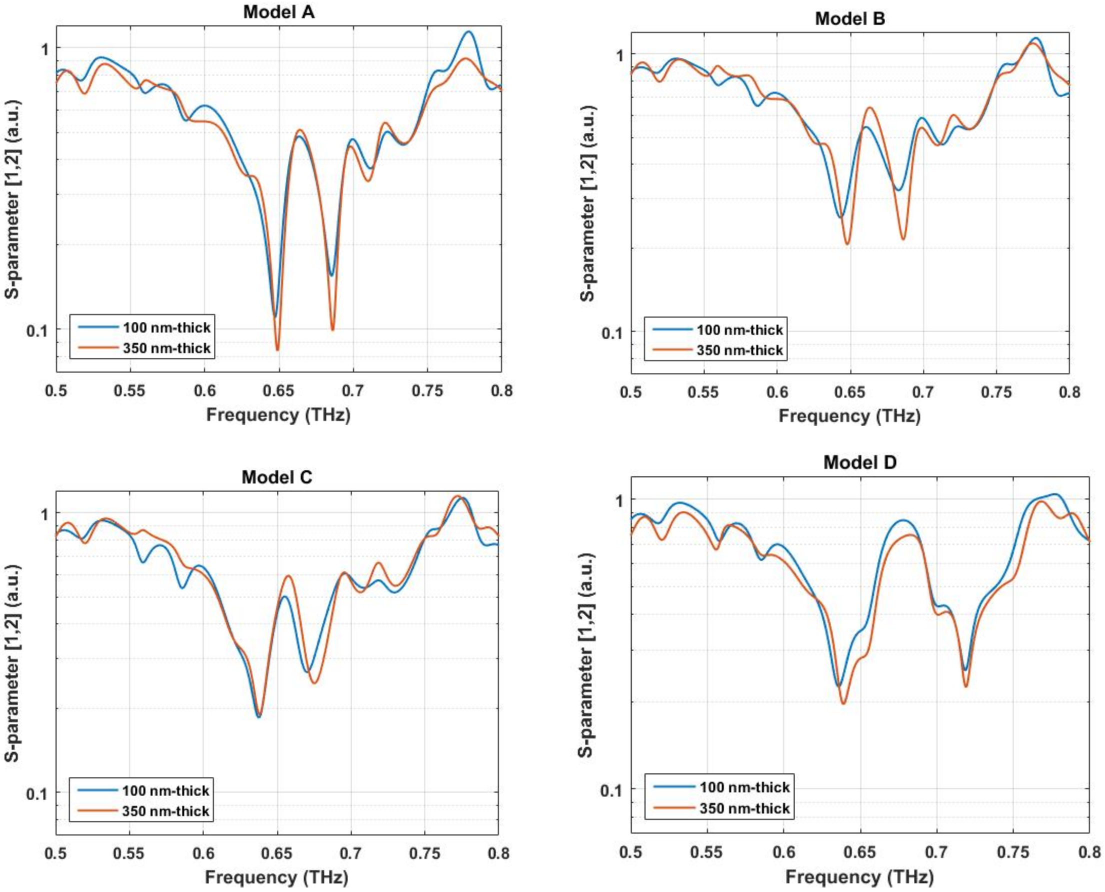

Figure 7-7 Experimental transmission frequency response for metamaterials A, B, C and D with 100 and 350 nm-thick gold resonators. (A. $L_1$= 180μm, $L_2$=170μm, α=80˚, d=10μm, B. $L_1$= 180μm, $L_2$=170μm, α=70˚, d=5μm, C. $L_1$= 180μm, $L_2$=170μm, α=80˚, d=5μm, D. $L_1$= 180μm, $L_2$=160μm, α=80˚, d=5μm), where ($L_1$) is the length of the left and ($L_2$) is the length of the right side of the resonator. (α) is the angle between the arms and (d) is the width of the arms of the resonator, portrayed in Figure 5.7.

According to Table 7-1, overall, model A and C have the highest quality factors of ≈50 consistent with both thickness of the resonators.

Model A, having resonators with wider arms, agrees with the simulation results of Section **Error! eference source not found.** and shows more steepness of the resonances compared to the model C with thinner arms. Model A has a much sharper resonance as a result of lower resistance of the structure, due to the fact that the width of the structure is larger and resistance is inversely proportional to the cross section of the conductor.

Model D, which is the model with the largest asymmetry, has the lowest quality factor. This is due to the fact that as the asymmetry is large, the two halves of the resonators, do not resonate at frequencies close to one another. As a result, the trapped-mode becomes wider and wider by increasing the difference between the two asymmetric sides. This is also confirmed by simulation results in Figure 7-8.

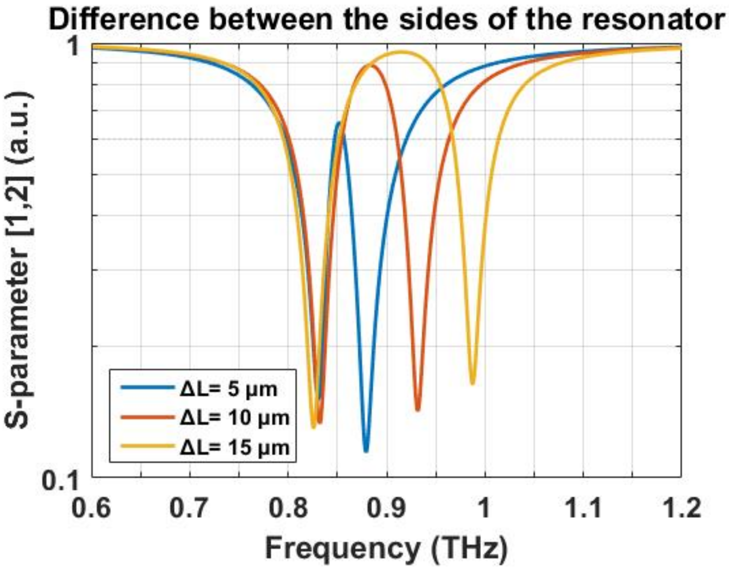

Figure 7-8 Transmission frequency response for different size of asymmetry in the resonator structure. Increasing the asymmetry from 5 to 15 μm.

The effect of the large asymmetry in the structure can introduce unpredicted couplings from the adjacent resonators (the larger side of a neighbouring resonator, overpowering the smaller part of the other X-resonator), resulting in weakening the resonance from each side of the X-resonator. This could introduce disorders in the structure and be the explanation for the irregular shapes of resonances in Model D (Figure 7-7). These kind of unpredicted modes in metamaterials resulting in weak frequency responses, due to disorders, have been studied and reported by *Papasimakis et al.* [94].

## 7.2 Comparison to the Simulation results

To compare the experimental results with the simulation results, the transmittance frequency response for each metamaterial model is plotted in Figure 7-9 and Figure 7-10.

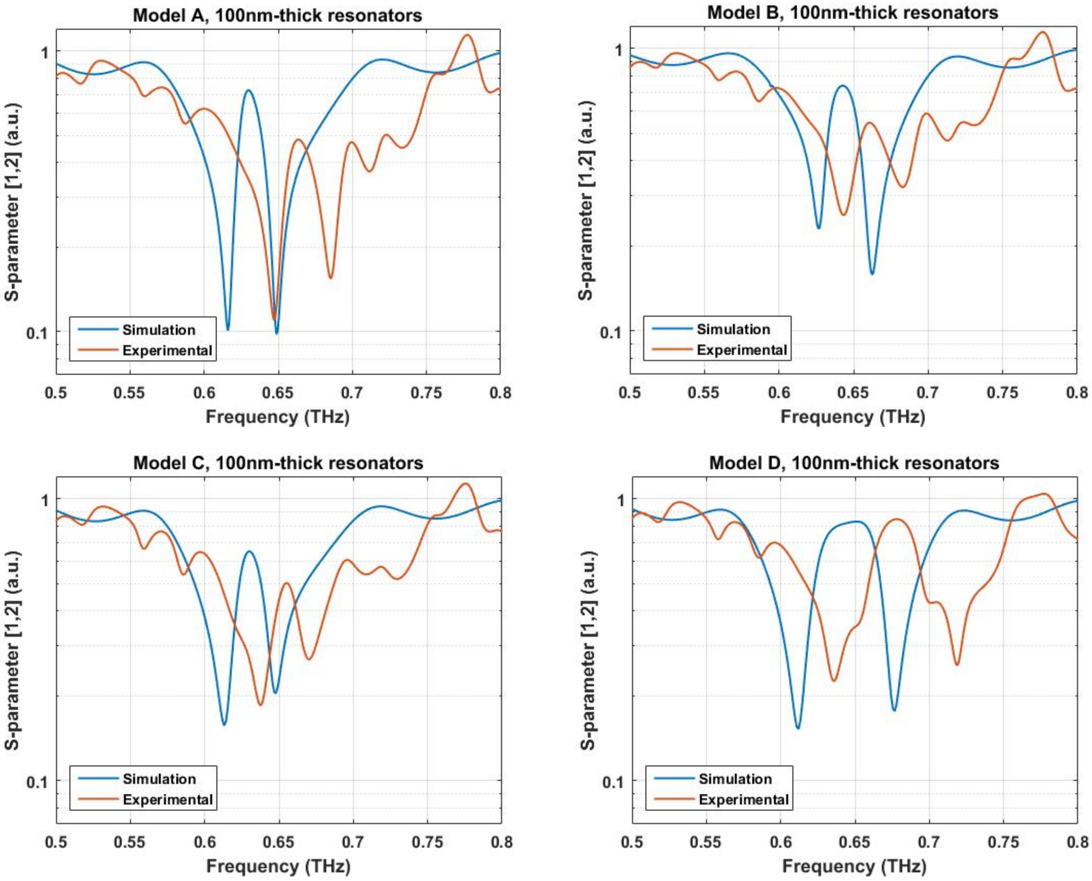

Figure 7-9 Experimental and simulation frequency responses for A, B, C and D models with 100 nm-thick resonators

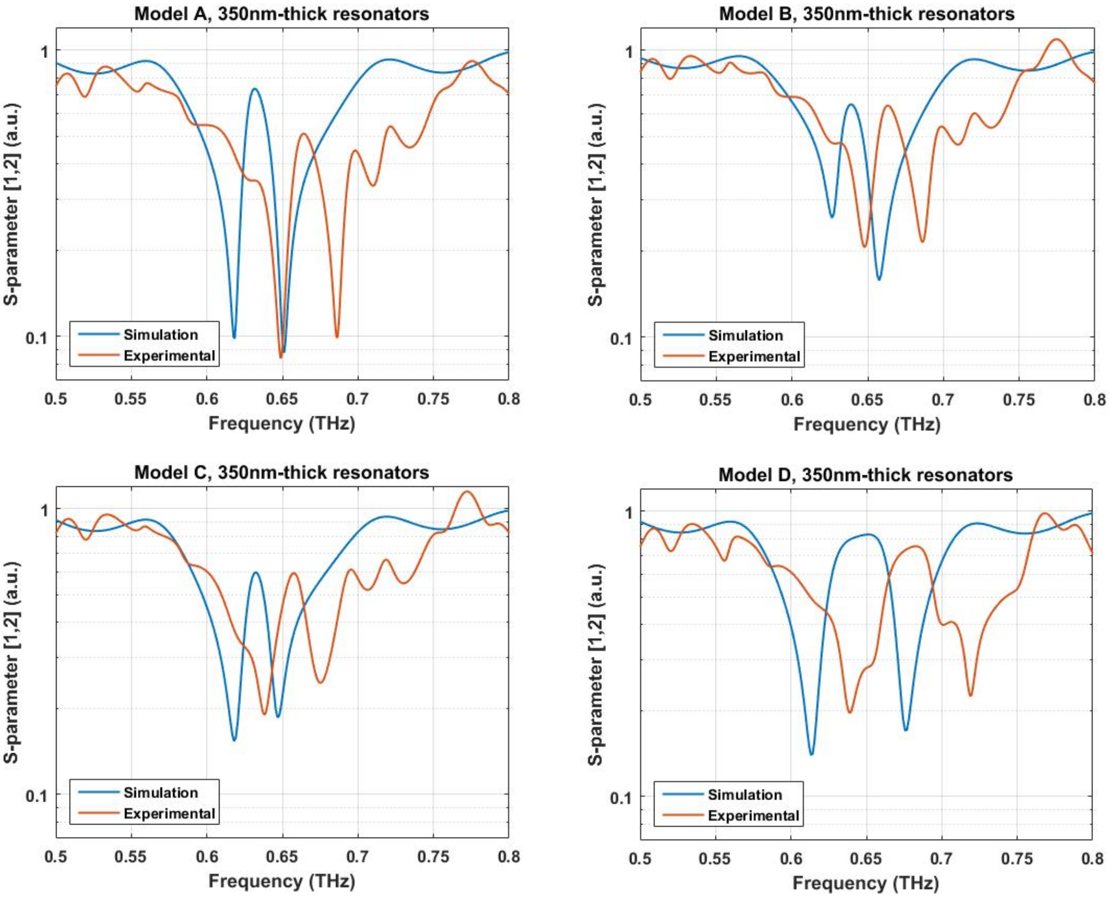

Figure 7-10 Experimental and simulation frequency responses for A, B, C and D models with 350 nm-thick gold resonators

The oscillations seen on the frequency response, are because of the etalon produced by the setup, causing infinite reflections of the theoretical transfer function.

For samples A and B, the first resonance in experimental results is steeper than the second one. However in simulation results, the second resonance is steeper than the first one. This result is consistent with multiple measurements of the same sample, and also when photoresist is introduced as the analyte in Chapter 8. Some of these effects are due to the dispersion model of the material used in the simulation that can be different from reality. The simulation data was tried to be fitted with the measurement, by experimentally extracting the complex refractive index from the materials. Still the calculations might not be the exact mirror of the reality.

Table 7-2 Simulation quality factor and resonant frequency of the trapped-mode resonance of metamaterials, A, B, C and D.

| **Metamaterial model** | | **A** | **B** | **C** | **D** |
|---|---|---|---|---|---|
| **100nm-thick resonators** | *$f_r$ (THz)* | 0.624 | 0.636 | 0.628 | 0.6516 |
| | Q-factor | 46.94 | 38.49 | 46.51 | 16.41 |
| **350nm-thick resonators** | $f_r$ (THz) | 0.626 | 0.6394 | 0.632 | 0.6516 |
| | Q-factor | 46.868 | 40.62 | 47.2 | 17.07 |

To be able to compare the simulation and experimental results, the quality factor and resonant frequency of the simulation models was calculated (Table 7-2).

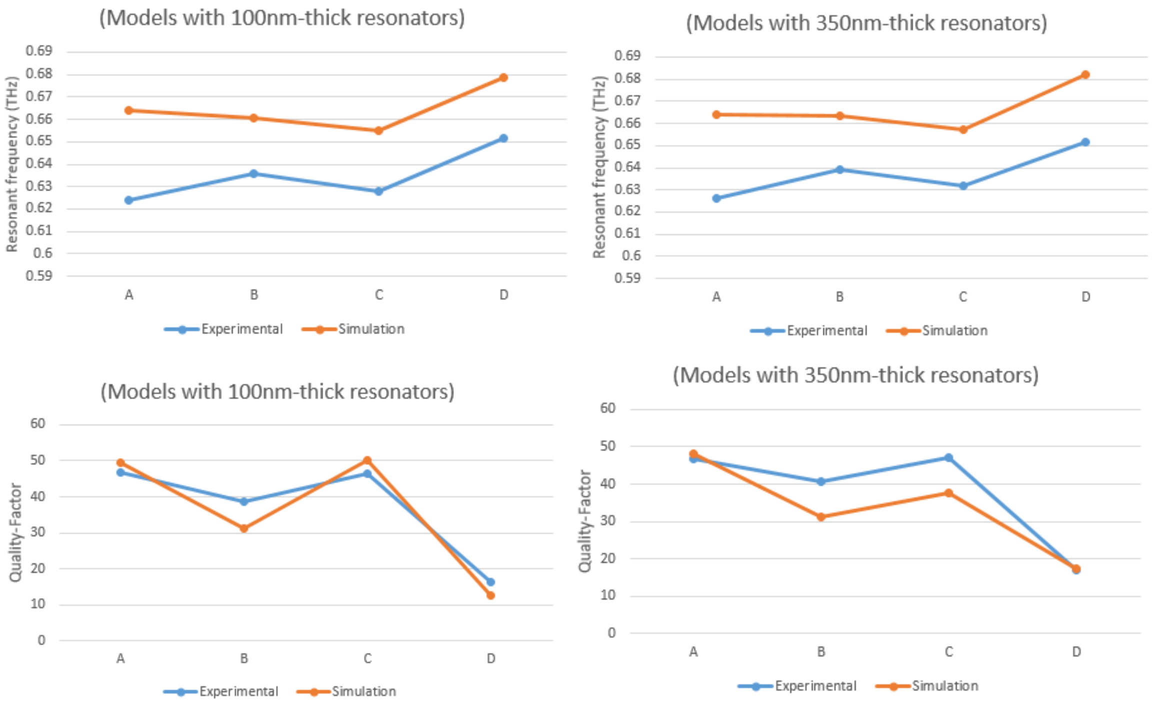

Figure 7-11 The line charts compare the Resonant frequency and Quality factor of A, B, C and D metamaterials for experimental and simulation results.

The resonant frequency and Quality factor for experimental and simulation results is shown in Figure 7-11.

The resonant frequency of the experimental results is roughly 0.03 THz higher than the resonant frequency for simulation results, consistent for all the samples, which could be due to inaccurate simulate material properties.

Regarding the quality factors, in simulation and experimental results, a consistency is seen; quality factor being the highest for A and C, and lowest for B and D models.

Where there is a change in the dielectric properties of a material, or in this case dielectric change in the whole structure, the resonant frequency would have a small shift [40]. The results suggest that, the dielectric properties of the simulated model are slightly out of tune with the dielectric properties of the experimental results. This is mainly because the fabricated X-resonators were 3% smaller than the simulated X-resonators.  This can be corrected by tuning the real part of the complex permittivity of simulation by the experimental which would result in simulation outcome, closer to real life results.

The dielectric losses for the simulation and experimental seems to be very close (seen from the quality factors) so the imaginary part of the permittivity is closer to the experimental data.

To tune the resonant response of the simulation with the experimental results, the size of the simulated structure was decreased by 3%. This way, the complex permittivity of the model decreases and the trapped-mode resonance shifts from 0.626 THz to 0.664 THz. The simulation was repeated for Metamaterial A with 350 µm-thick resonators, Figure 7-12.

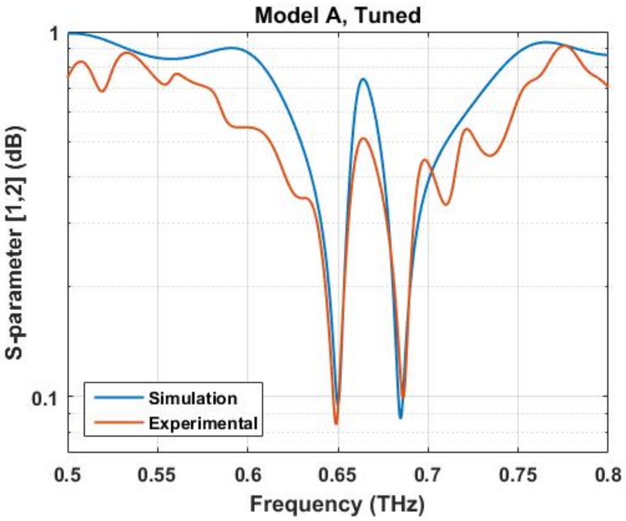

Figure 7-12 Transmittance frequency responses for metamaterial A with 350 nm-thick resonators, when the simulation results tuned to the experimental data

The transmittance frequency response in Figure 7-12, confirms that by tuning the dielectric properties of materials in simulation (by changing the size of the metamaterial), a response much closer to that of experimental results is achievable, without compromising the quality factor or physical properties of the resonance curve.

## 7.3 **Dynamic Range and Signal to Noise Ratio (SNR):**

The THz data is a relative magnitude to the reference sample and therefore the dynamic range is seen as the signal to noise ratio. Here, the amplitude of the metamaterial is compared to the magnitude of the reference scan over the measured frequency. The noise is ~$10^5$ intensity units. Because the absorption peak of the resonance for the metamaterial (around 0.6 THz) is above this value by an order of magnitude, the resonance peak absorption can be accurately resolved, showing an SNR of ~50 dB.

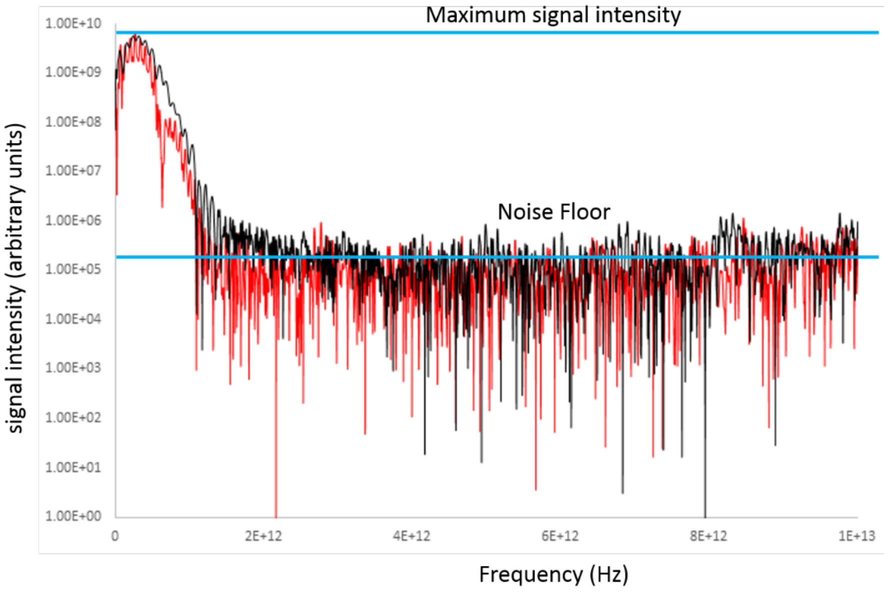

Figure 7-13 the amplitude of the metamaterial is compared to the magnitude of the reference scan over the measured frequency, showing the noise floor and maximum signal intensity

## 7.4 Conclusion

In this chapter, the measurement results of the fabricated metamaterial samples were explained. In the fabrication process of the metamaterials, there will be unavoidable inaccuracy in the structural dimensions due to limitations of the fabrication technology. These inaccuracies can be errors in the thickness and width of the metal film or the roughness of the metal surface relative to the theoretically designed structure. All these structural size deviations would lead to property changes of the metamaterials with respect to the originally designed ones.

However, the transmittance frequency response for the fabricated metamaterials is in agreement with the simulation results. For each metamaterial almost an equal shift is observed for the frequency of resonances between experimental and simulation frequency response, which is tunable by shrinking the modelled metamaterial by 3%.

Also, the shape of the resonances and the quality factors between simulation and experimental results are similar. And by tuning the dielectric properties of the substrate from simulations, the resonant frequency matches, the resonant frequency of practical results.

Furthermore, by comparing the transmittance of each fabricated sample it was shown that, if the asymmetry is too large in the inclusions, the trapped-mode can become weak and the single resonators can become wider and noisy.

*Fedotov et al. [17]* presented metamaterials with copper asymmetric double split ring resonators. The inclusions were in millimetres range on an IS620 PCB (printed circuit board) substrate. Their results showed a quality factor of ≈20 for the trapped-mode resonance.

Similarly, *Lahiri et al. [18]* showed a quality factor of ≈11, for gold double split ring resonator metamaterials on a silica substrate, with inclusions approximately a hundred times smaller than the structures presented in this work.

Compared to the quality factors shown in these studies, the quality factor in this study, being as high as ~50 is almost 3 times larger than what they achieved. The higher quality factor is an important aspect here, because it is easier to detect the shift in a sharp shift compared to a gentle slope.

# Chapter 8 **Operating as a biosensor**

## 8.1 Introduction

One of the anticipated outcomes of the biosensor under study is to distinguish between different types of RNA and DNA by comparing the natural resonance of their backbone structure. However, in simulation, it is almost impossible to replicate the exact frequency response of a specific DNA/RNA with the complete range of natural resonances present. Instead, using the dielectric properties of two RNA samples from the literature [95], dielectric blocks ( imitating the RNA samples), were modelled. The shift in the frequency response and change in the power of the resonance is reported for each sample.

Next, in 8.7 to be able to replicate these results in fabrication, a layer of photoresist was applied on top of the resonators acting as a dielectric layer mimicking the analyte.

## 8.2 RNA samples

To study the model capability of detecting RNA/DNA backbone frequencies and distinguishing between them, the dielectric data for two artificial RNAs was extracted from the literature [95] and was used to make a dispersion model for the RNA samples in CST software. The two RNA samples are polyadenylic acid (Poly-A) and polycytidylic acid (Poly-C). These are commercially manufactured polymer structures and are available in the powder format. Fischer et al. [95], used time domain spectroscopy (TDS) to measure the absorption spectra and the refractive index for poly-A and poly-C.

RNA samples are modelled as a block of dielectric in the simulation using their dielectric properties. The dielectric constant of Poly-A and Poly-C from Fischer et al. [95] around the frequency of interest ( highest backbone frequency) is shown in Table 8-1, (for simplicity of modelling, only the real part of the dielectric constant is used) :

Table 8-1 the dielectric constant for two artificial RNAs, Polyadenylic acid (Poly_A) and Polycytidylic acid (Poly_C) at different frequencies in THz region

| Frequency (THz) | $\varepsilon_r$ (Poly-A) | $\varepsilon_r$ (Poly-C) |
|---|---|---|
| 0.75 | 3.5156 | 4.2884 |
| 0.78125 | 3.469 | 4.2025 |
| 0.84375 | 3.594 | 4.1006 |
| 0.875 | 3.3687 | 4.0683 |
| 0.90625 | 3.361 | 4.117 |
| 0.9375 | 3.3233 | 4.1006 |
| 0.96875 | 3.3233 | 4.1429 |
| 1 | 3.3233 | 4.138 |

## 8.3 Simulation with RNA samples

Initially, the dielectric blocks representing Poly-A and Poly-C RNAs are modelled on top of the X-resonators as rectangles ($30 * 15\mu m^2$ with 0.5µm thickness).

The mesh for the X-structure is the same as explained in Chapter 5. For the RNA samples, the maximum mesh width is set to 1 µm in X and 10 µm in Y direction. However, to be able to discretize the thickness of RNA samples more accurately, the minimum width is reduced to 0.2 µm in the Z direction (Figure 8-1).

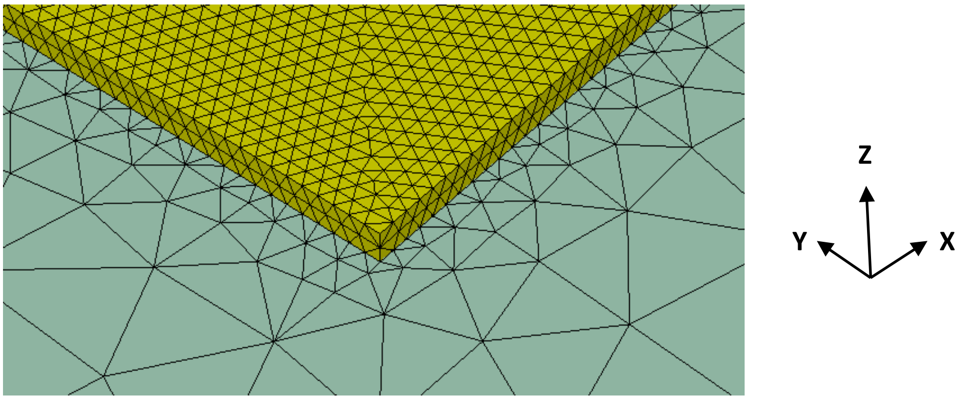

Figure 8-1 Tetrahedral mesh for the edge of the RNA sample

Samples are fixated on the either ends of the two shorter arms of the X-structure (Figure 8-2). The substrate in these analysis is a 0.2 mm-thick COC film. The dimensions for the X-resonators are $L_1$= 180 µm, $L_2$=170µm, α=80µm, d=5µm (according to Figure 5-6).

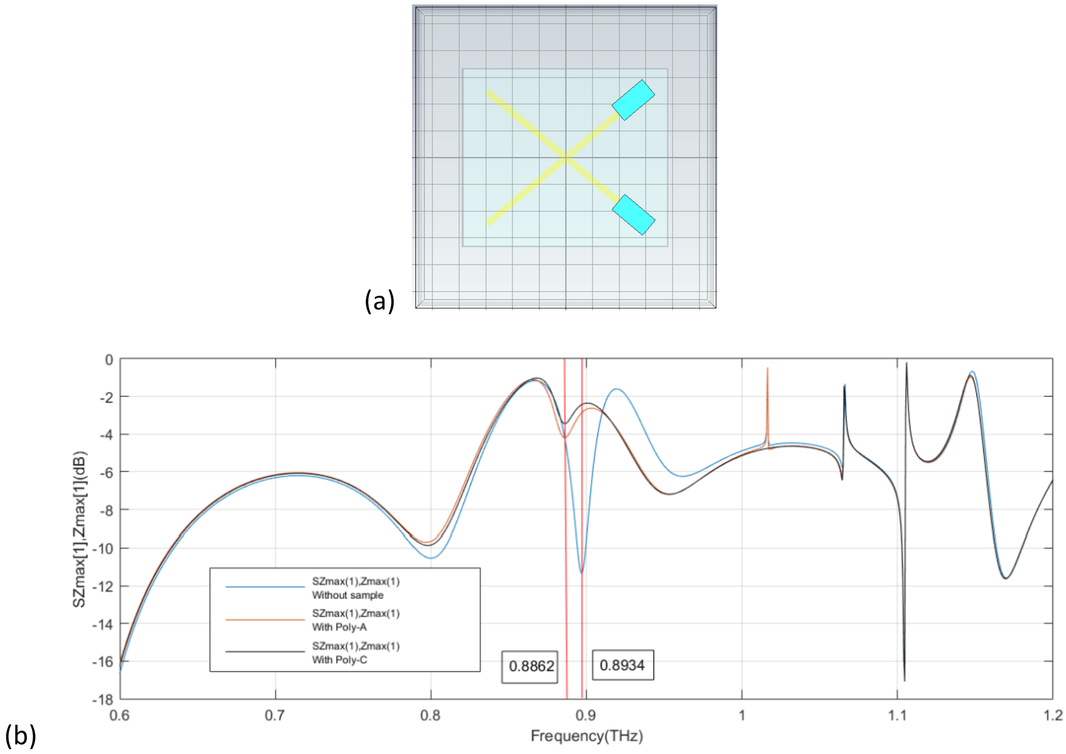

Figure 8-2 (a) the dielectric blocks representing RNA samples are placed at the either ends of the two shorter arms of the X-structure. The RNA blocks are $(30 * 15 * 0.5\ \mu m^3)$ cuboids. (b) the frequency response for the model with and without Poly-A and Poly-C is plotted. The trapped mode for the model without any samples happens at $F = 0.8934\ THz$ and for the model with the Poly_A and Poly_C samples happen at $F = 0.8862\ THz$

The S-parameter graph for he models with and without Poly-A and Poly-C samples, is shown in (Figure 8-2 (b)).

To make sure that the resonance observed from adding the analytes is indeed the trapped-mode resonance of the X-structure, the induced currents at the arms of the resonator was checked at their resonant frequency ($f = 0.8862\,THz$). The surface current before, at and after the frequencies that the trapped-mode resonance is happening is shown in Figure 8-3. The induced currents on top of the X-resonator show that this is the trapped mode from the resonating structure.

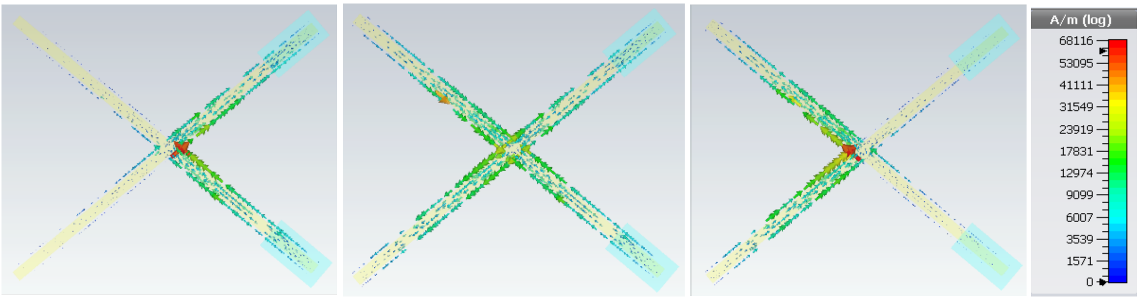

$F = 0.865\,THz$ $F = 0.8862\,THz$ $F = 0.8991\,THz$

Figure 8-3 for the 375µm quartz substrate with Poly-A, Induced currents at the arms of the resonator, before ($0.865\,THz$,), at ($0.8862\,THz$) and after ($0.8991\,THz$) the trapped mode resonance are presented.

By adding the Poly-A or Poly-C block on top of the X-resonator arms, the frequency response shifts, which can be observed in Figure 8-2. The trapped mode magnitude and resonant frequency both change, which is due to damping as a result of adding the RNA blocks. Comparing Poly-A and Poly-C, it is noticeable that their trapped mode resonant mode happen at the same frequency with only differing in the magnitude of their trapped mode.

The difference between the graphs with and without Poly-A blocks is plotted in Figure 8-4, which will be useful in analysing and comparing the results when the position of the analyte on the X-resonator changes.

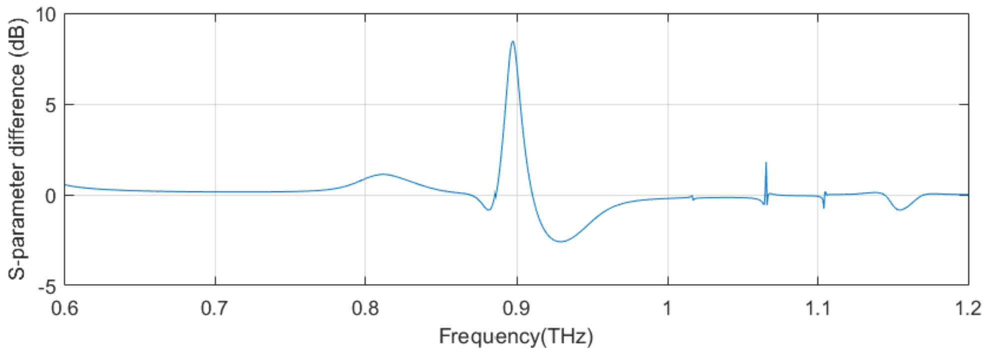

Figure 8-4 The difference between the frequency response of the model with and without Poly-A

## 8.4 Different sizes of RNA

Initially, the RNA samples were modelled as blocks of $(30 * 15 * 0.5\ \mu\mathrm{m}^3)$ dimensions on either arms of the X-structure on the shorter side.

Here, the simulation is repeated with different length and thickness of the Poly-A blocks. Which is done to visualise the difference that it makes buy changing the position and the size of the RNA samples on the X-resonator.

## 8.5 Different thicknesses of RNA

Thirty different samples of the Poly-A blocks are modelled with the thicknesses ranging from 0.2 to 0.5 $\mu\mathrm{m}$, keeping the Length of the sample constant $(30\ \mu\mathrm{m})$.

The Frequency response for each one of the samples is modelled. For the sake of comparison the frequency responses are presented on one plot in Figure 8-5:

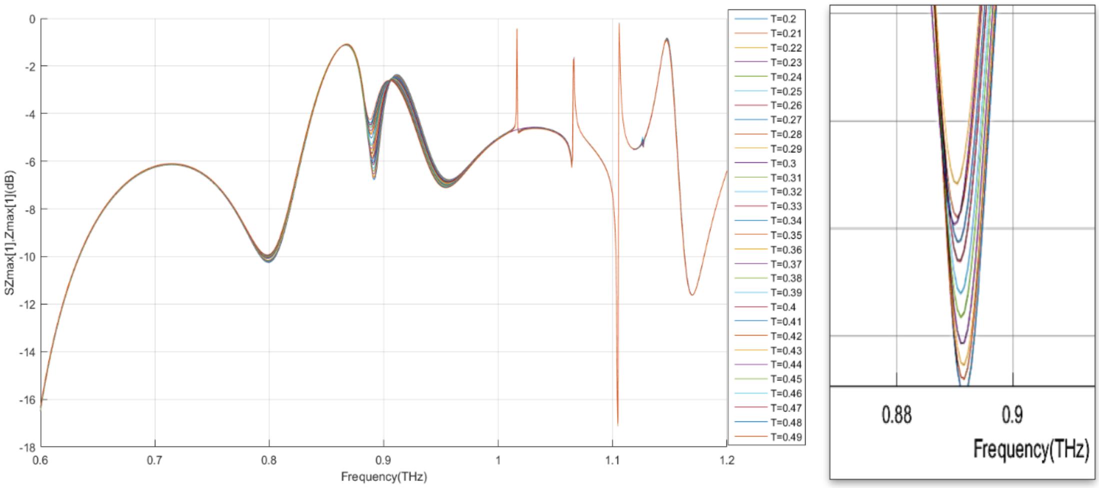

Figure 8-5 Frequency response of poly-A sample with different thicknesses $(0.2\mu m < \boldsymbol{T} < 0.5\mu m)$. The trapped modes are shown in a close-up format for a better visualisation.

Increasing the thickness of the RNA sample expectantly decreases the amplitude of the trapped-mode resonance and subsequently the quality factor. To study how the changing of the thickness affects the frequency where the trapped-mode happens, the trapped-mode frequency of each sample is extracted and shown in Figure 8-6.

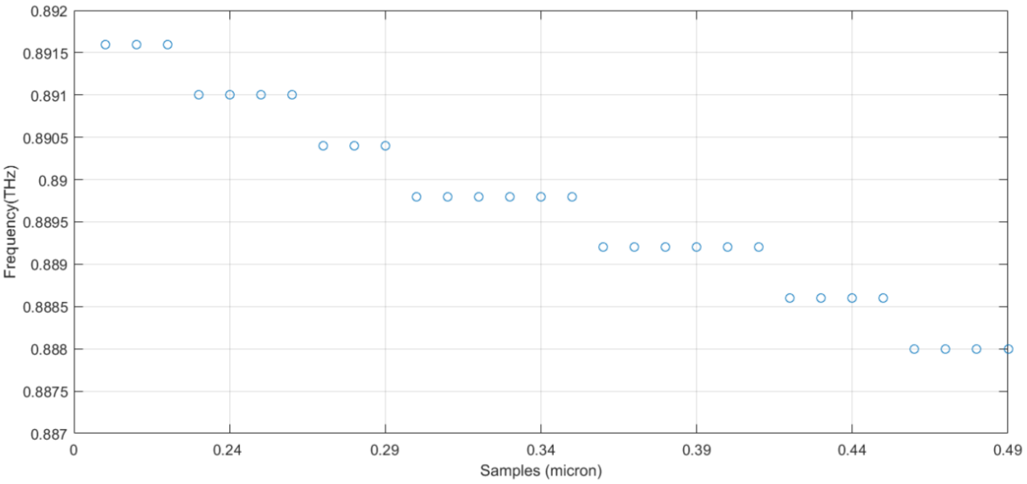

Figure 8-6 Frequency of the magnitude of the trapped-mode for each thickness ($0.2\mu m < \boldsymbol{T} < 0.5\mu m$)

The trapped-mode frequency decreases by increasing the frequency which means the trapped-mode shifts to the left by increasing the thickness of the sample on the resonator. This means that change in the thickness makes a difference in the frequency response. The thicknesses close to each other (For example T= 0.21, 0.22 and 0.23 microns) seem to shift the frequency of the trapped mode equally. Which is due to the mesh not being fine enough to change with the slight increase in the thickness of the analytes. However, it is expected to see a linear frequency shift in experimental trials.

To get a better understanding of the results, the difference between the model without sample and each of results from different thicknesses of the RNA sample is plotted in Figure 8-7.

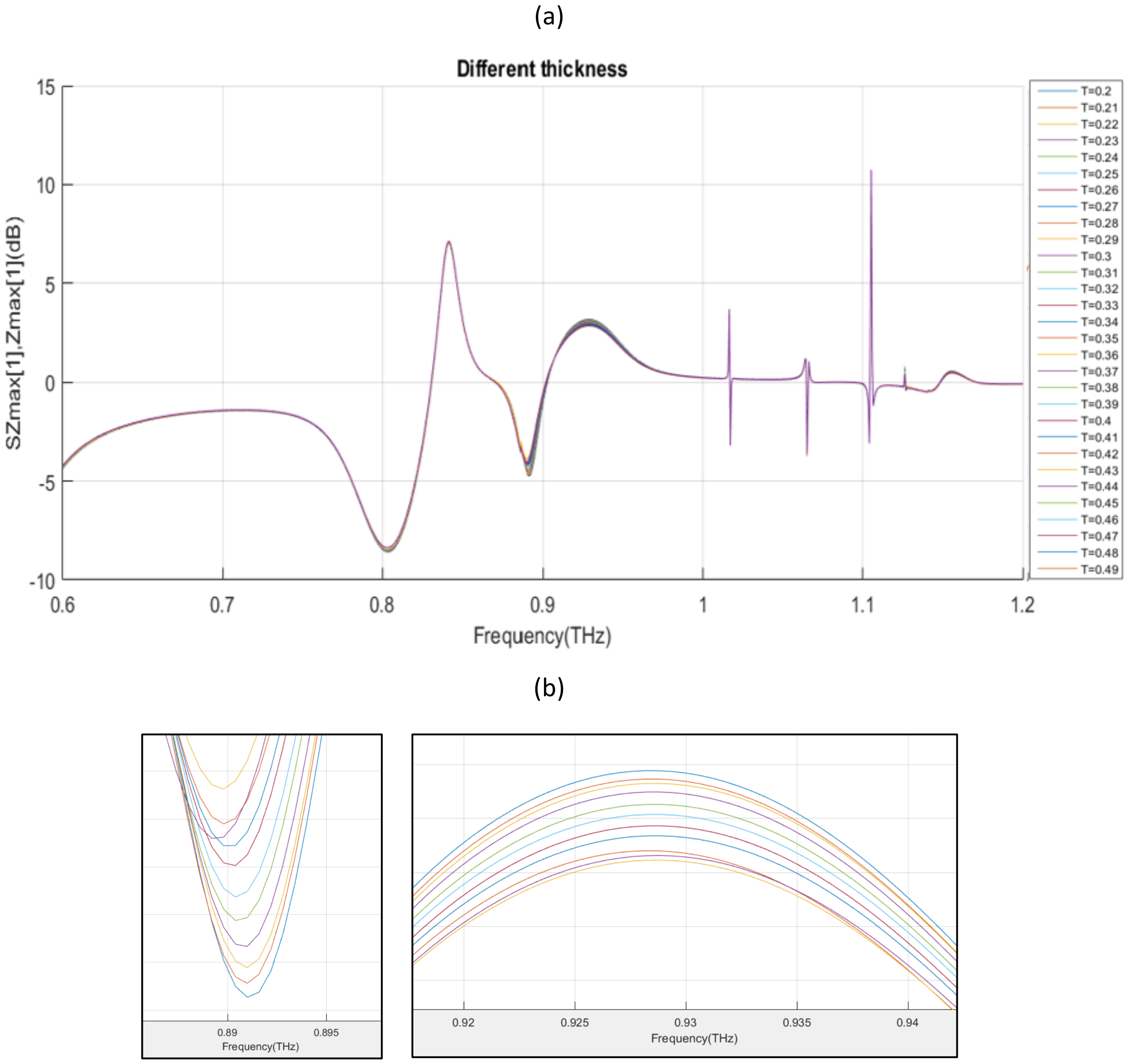

Figure 8-7 (a) The magnitude difference between the model without any Poly-A sample and the models with the Poly-A samples of different thicknesses are plotted (b) The close up of the curves

The difference between the plots shows a smooth decrease in the frequency response. The only curve that seems to not to follow the pattern along with others is the sample with T=0.47 μm (visible in Figure 8-7 (b)), which is most likely due to the finite element and convergence error.

## 8.6 Different lengths of the RNA samples

Twenty different Poly-A samples were models with their length extending from 25 to 90 $(\mu\text{m})$, (Figure 8-8) keeping the thickness and the width of the samples constant at 0.5 μm and 15 μm respectively.

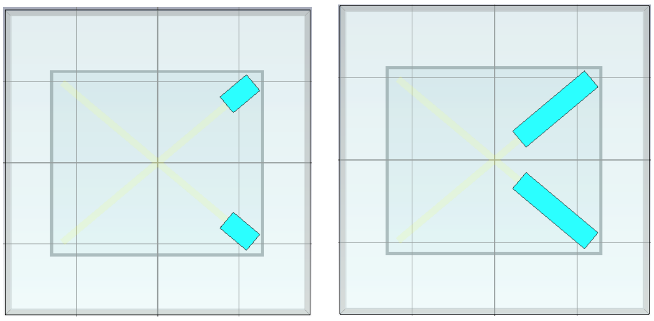

Figure 8-8 Different length of RNA samples. The length extends from 25 $\mu m$ (the figure on the left) to 67 $\mu m$ (the figure on the right).

The Frequency response for each one of the samples is modelled (Figure 8-9):

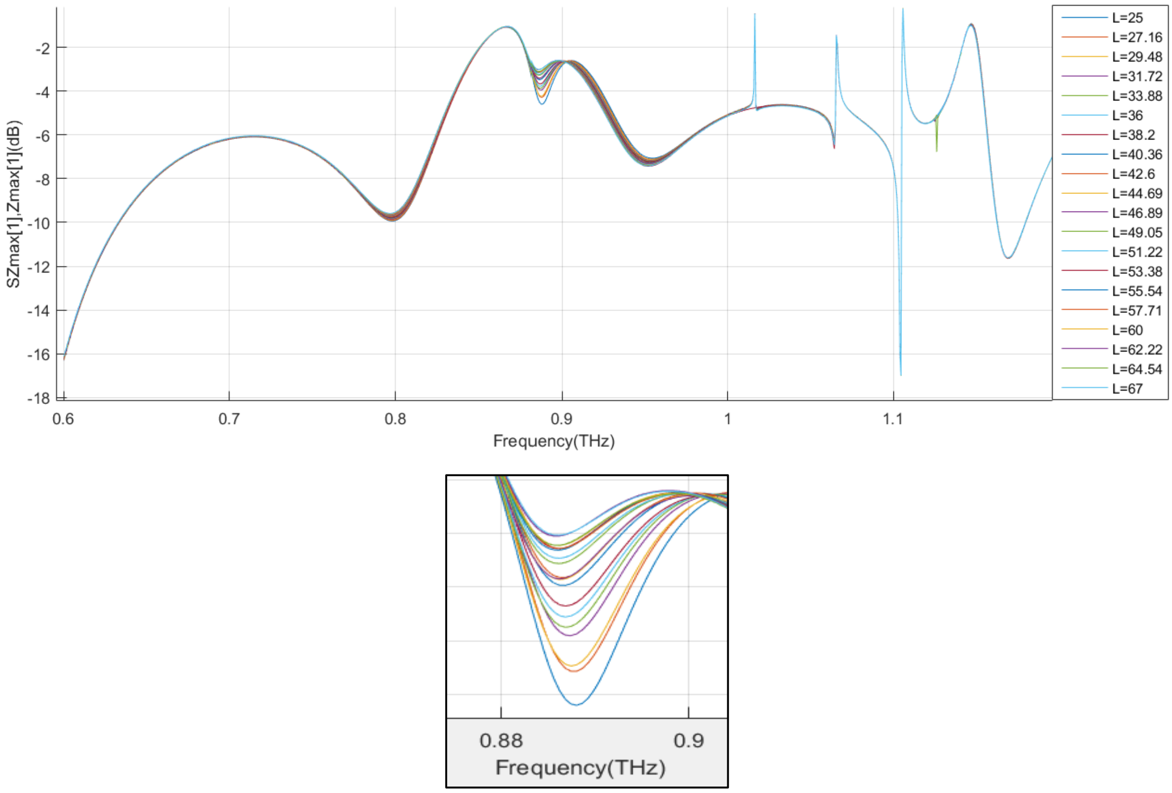

Figure 8-9 Frequency response of poly-A samples with different lengths ($25\mu m < \boldsymbol{L} < 67\mu m$). The trapped-modes are shown in a close-up.

As it is shown in Figure 8-9, increasing the length of the RNA samples evidently reduces the magnitude of the trapped-mode resonance and subsequently the quality factor of the resonant mode.

Like the previous section, to see how varying the length of the analyte, changes the frequency where the trapped-mode happens, the trapped mode frequency of each sample is shown in Figure 8-10.

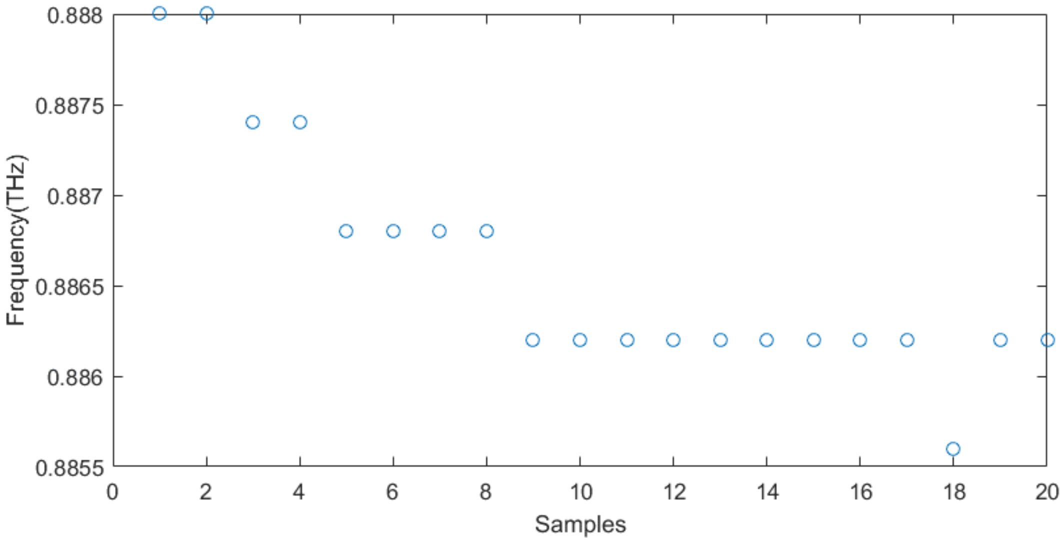

Figure 8-10 Frequency of the highest point of the trapped mode for each thickness ($25\mu m < \boldsymbol{L} < 67\mu m$).

The frequency of the trapped-mode resonance decreases by increasing the length of the RNA sample in a consistent fashion. The only sample that does not follow the pattern is that of $L = 62.22\ \mu\text{m}$, which is due to a convergence error.

It is apparent that if the length of the sample is increased, the trapped-mode resonance decreases. However, the frequency of the trapped-mode appears to follow a linear pattern. For the analytes with lengths very close to one another the frequency response seems to be the same which is mostly due to lack of fine meshing. This is expected to be resolved with lowering the maximum mesh step width, lower than 0.2 µm.

## 8.7 Photoresist samples

For experimental purposes of this study, and to be able to check the device sensitivity as a sensor, photoresist was used as the analyte. For this, a 1µm-thick layer of S1813 photoresist is modelled on top of the X-resonators (covering the whole surface of each resonator). The dielectric constant of S1813 ($\varepsilon_r$=3.5) was obtained using THz-TDS, and was used for the material properties.

By observing the shift in the frequency and the magnitude of the resonance, the sensitivity of the metamaterial to the S1813 analyte can be obtained. The substrate used in this section is the same as the one used in fabrication (1mm-thick COC wafer from microfluidic ChipShop (© 2005-2018 microfluidic ChipShop GmbH)). The dimensions for the X-resonators are the same as in 8.3 section for RNA samples.

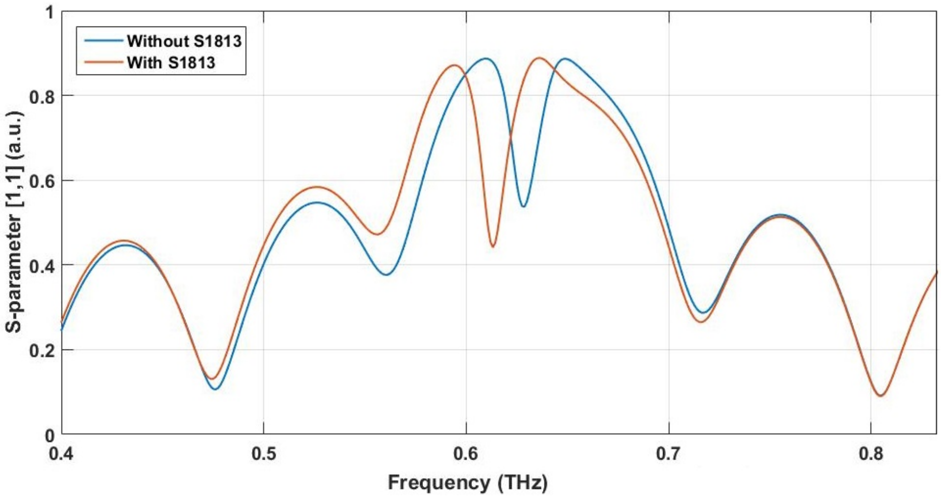

Figure 8-11 Reflection frequency response for the metamaterial-base sensor, with and without S1813 as the analyte.

The results from Figure 8-11 show a shift in the frequency of resonance of the metamaterial. These results is used in the next section, to be compared with the fabrication results of the same model.

Next, to test the metamaterial as a sensor, a 1µm-thick layer of photoresist (S1813) was applied on the top of the resonators to act as dielectric blocks, representing the possible analytes.

Dr Vasilis Apostolopoulos and his team in THz group, University of Southampton, carried out the measurements of the sensors, using Terahertz time-domain Spectroscopy (THz-TDS).

## 8.8 **Fabrication**

A COC wafer with 350 nm-thick gold resonators was prepared, comprising 4 different metamaterials. The fabrication process is the same as explained in Chapter 6 with additional steps to add the positive photoresist (S1813) on top of the resonators to act as analytes.

To achieve this, after the lift-off process, a layer of S1813 was spun on the COC wafer for 30 seconds with 6000 rpm speed. Afterwards, the resist baking was done at 110 ° C for 180 seconds. Following the soft-bake, photolithography was done using EVG620TB mask aligner, exposing the photoresist to UV rays for 6.5 seconds using the same photomask as before (hard contact). Subsequently, the pattern on the mask was developed by merging the wafer in MF319 for 30 seconds, followed by rinsing with DI water and spin drying.

As, S1813 is a positive resist, after exposure to UV rays using a bright field photomask, and development, the patterns on the mask will stay on the wafer, and the other parts of the resist will dissolve. This way, an X-shaped 1µm-thick layer of S1813 was patterned on top of each gold resonator (Figure 8-12).

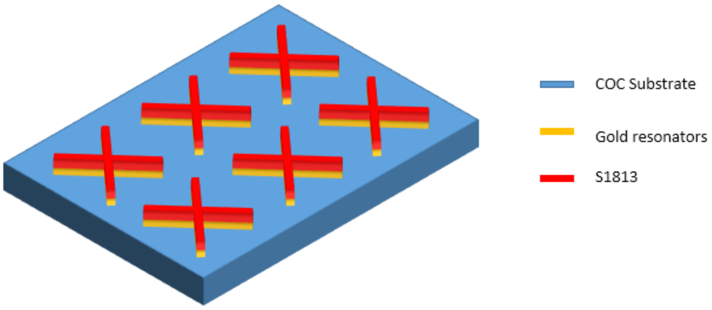

Figure 8-12 Illustration of a section of the fabricated metamaterial with S1813 as analytes

## 8.9 Measuring refractive index of S1813

The transmitted power of a clean COC wafer with a 1 µm-thick S1813 was measured to determine the complex refractive index of S1813 in THz, Figure 8-13. The complex refractive index of S1813 is used to build the dielectric dispersion model of the material in the simulation. There are also oscillations seen in the refractive index plot, which is a result of the etalon produced by the setup. Other than that, the real part of the refractive index is almost consistent throughout the 1 THz frequency range at 1.6. Assuming that the relative permeability is 1, the real part of the permittivity would be 2.56. Also, the average for the imaginary part of the complex refractive index of S1813 is close to 0.

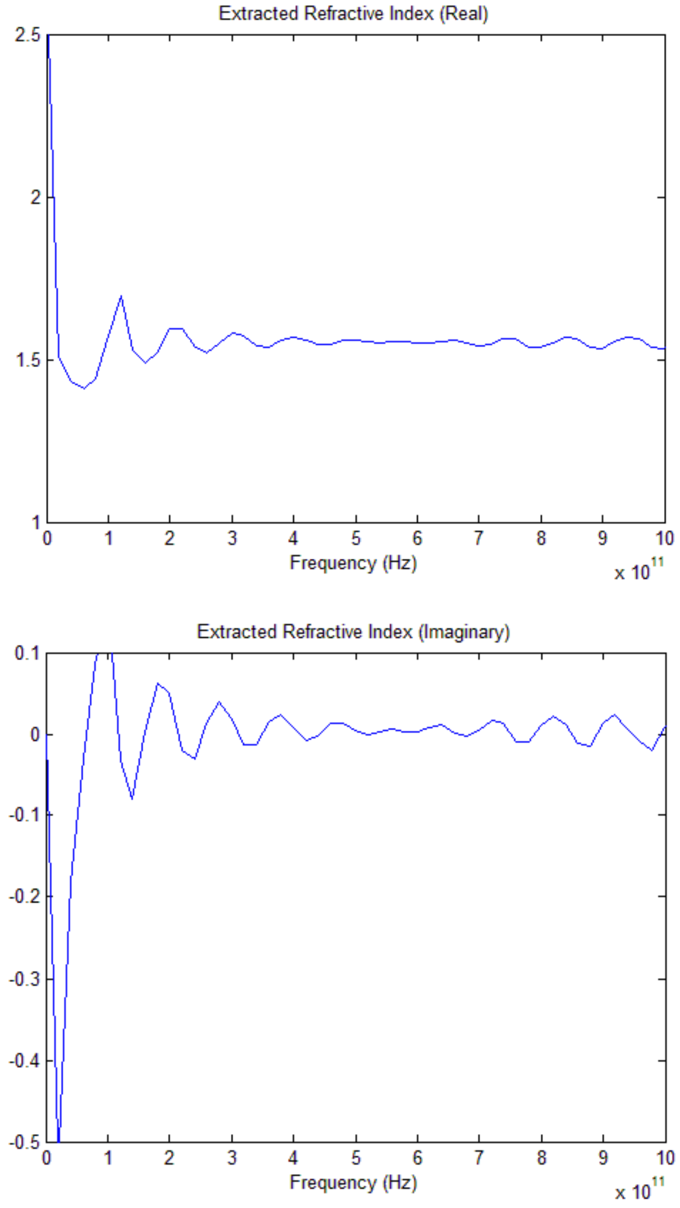

Figure 8-13 Complex refractive index for a 1 µm-thick S1813 determined experimentally

## 8.10 Measurement

Four different metamaterials were prepared, with different dimensions for the X-resonator, each with a 1µm-thick layer of photoresist on top of the X-resonators.

All the measurements were taken with the same setup as the measurements in Chapter 7.The experimental setup uses a Titanium Sapphire femtosecond (fs) laser with a continuous wave power of approximately 1.2 W. The data is measured over a 50 picosecond range (Time domain) and converted to frequency domain using Fourier Transform.

To increase the accuracy, these measurements were taken back to back (at the same time) with the measurements of Chapter 7. This way the time difference in the measurements would not affect the data by introducing fluctuations to the intensity.

The SNR is ~50 dB. The scan frequency resolution ($f_s$) is 0.02 THz and is artificially increased to 0.0003 THz, same as for the measurements for the metamaterials without the analyte present.

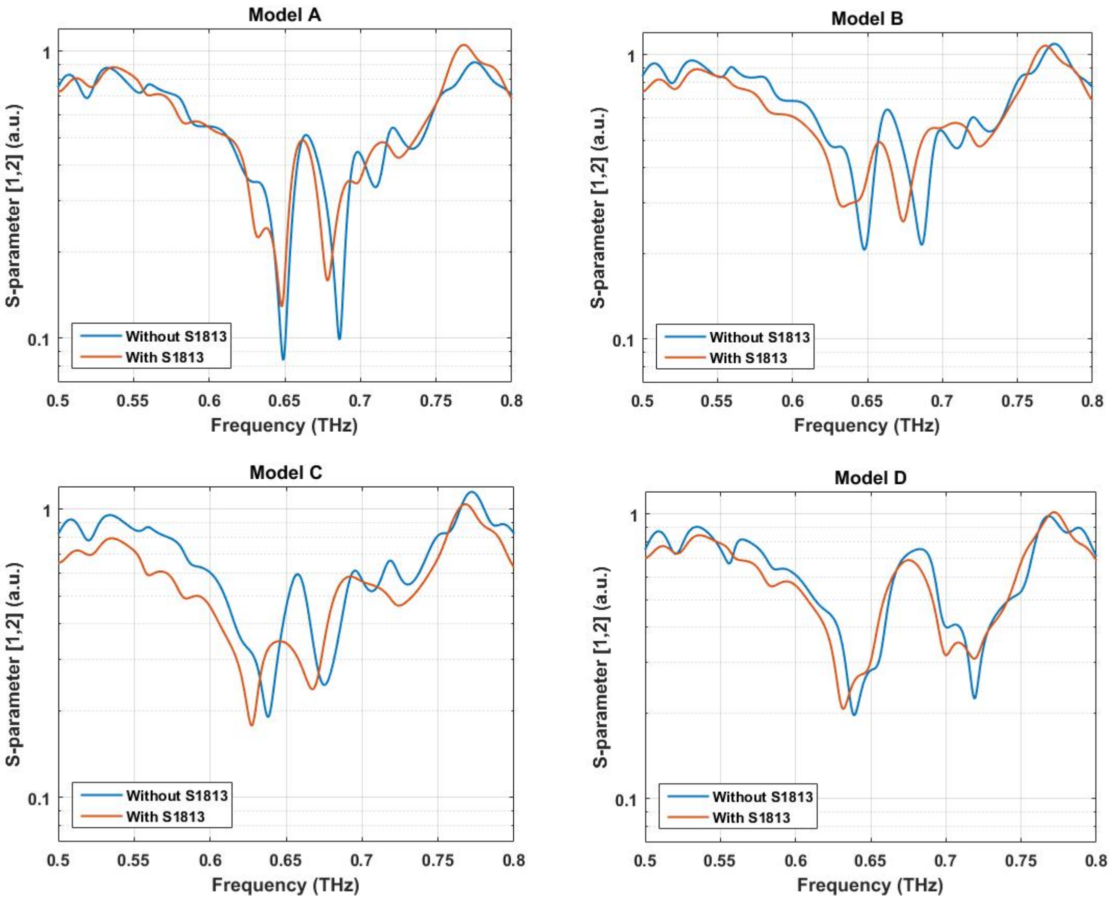

Figure 8-14 Experimental transmission frequency response for metamaterials A, B, C and D with 1µm-thick S1813 as analyte.

Figure 8-14, shows the comparison between the metamaterials with and without the analyte (S1813). In all the models, when the S1813 is added on the resonators, the frequency of resonance has dropped by an average of ~0.03THz. This happens as a result of changing the relative permittivity of the whole structure, due to adding the photo resist layer on top of the gold resonators.

Table 8-2 Experimental quality factor and resonant frequency of the trapped-mode resonance of metamaterials, A, B, C and D, when S11813 analyte is present.

| | **Model A** | **Model B** | **Model C** | **Model D** |
|---|---|---|---|---|
| ***$f_r$ (THz)*** | 0.6619 | 0.6578 | 0.6456 | 0.688 |
| **Q-factor** | 54.25 | 45.7 | _ | 17.24 |

THz. This happens as a result of changing the relative permittivity of the whole structure, due to adding the photo resist layer on top of the gold resonators.

Table 8-2, shows the quality factor and resonant frequencies for the metamaterials with S1813. Quality factor for each metamaterial follows the same trend (Figure 8-15), when the analyte is added compared to the models without the analyte. Apart from the quality factor for the model C. The quality factor for Model C is not applicable, as magnitude of the trapped-mode resonant is too low. This is suspected to be due being smoothed out as a result of noise suppression.

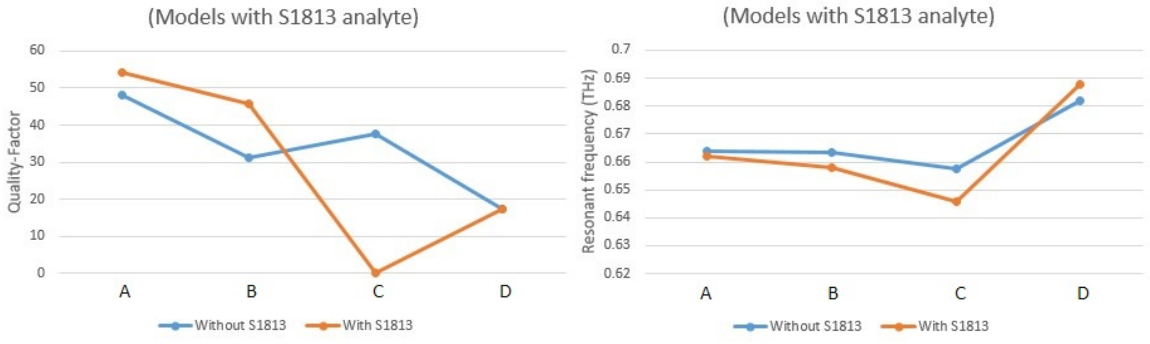

Figure 8-15 Quality factor and resonant frequency of the trapped-mode resonance of fabricated metamaterials, A, B, C and D, when S11813 analyte is present compared to when S1813 is not present.

## 8.11 Comparison to simulation

Metamaterials A, B, C and D were simulated with a 1µm thick S1813 on top of the X-resonators, with the same specifications as part 8.7.

Figure 8-16, shows the comparison between the Experimental and simulation results, when the analyte (S1813) is present.

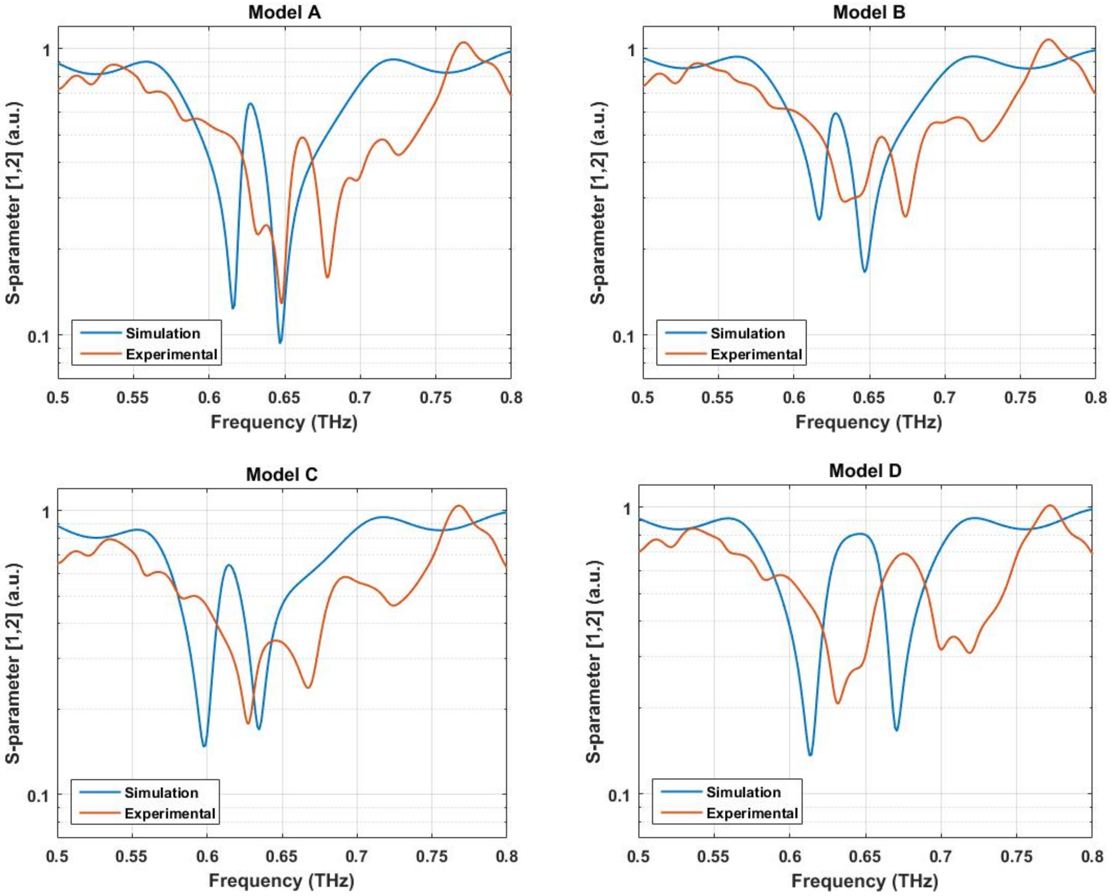

Figure 8-16 Experimental and simulation frequency responses for A, B, C and D models with 1 µm-thick S1813 analyte

Table 8-3 Simulation; Quality factor and resonant frequency of the trapped-mode resonance of metamaterials, A, B, C and D, when S11813 analyte is present.

| | **Model A** | **Model B** | **Model C** | **Model D** |
|---|---|---|---|---|
| **$f_r$ *(THz)*** | 0.6276 | 0.6276 | 0.6144 | 0.6456 |
| **Q-factor** | 43.6 | 41.2 | 34.13 | 15.8 |

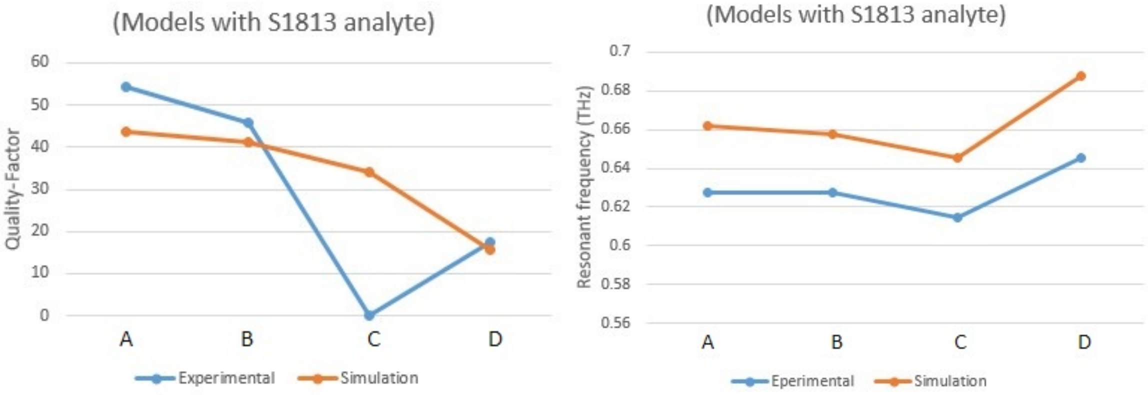

Figure 8-17 Quality factor and resonant frequency of the trapped-mode resonance of experimental and simulated metamaterials, A, B, C and D, with S11813 analyte.

Table 8-3, shows the quality factor and resonant frequencies for the metamaterials with S1813, followed by Figure 8-17 that shows the comparison between the quality factors of experimental and simulation data.

The quality factors, for the experimental results is higher than that of the simulation, apart from model C, which as explained, is possibly due to a measurement inaccuracy.

Compared to the simulation results the experimental results of samples with S1813 show a decrease in the resonant frequency (~0.035 THz), following an almost perfect trend from model A to model D. As this difference is repeated for all the metamaterials at almost the same rate, it suggests that the model, is a reliable recreation of the reality. The difference between the resonant frequency of simulation and experimental metamaterials, is due to the fabricated resonators being 3% smaller than the simulated resonators.

To resolve this, and to fit the simulation result to the experimental results, the modelled metamaterial A with S1813 was shrunk by 3%, the frequency response is shown in Figure 8-18. The frequency response shows that by tuning the dielectric properties of the simulation to the experimental models, the trapped-mode resonance of the simulation shifts from 0.6276 THz to 0.66 THz, which is an almost match to the practical results.

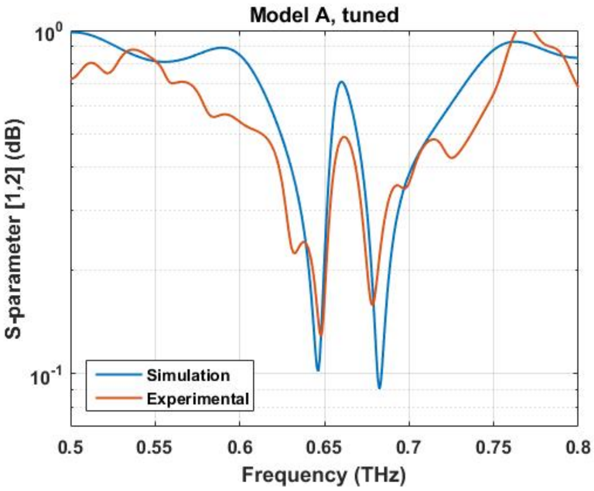

Figure 8-18 Transmittance frequency responses for metamaterial A with 350 nm-thick resonators and 1 µm-thick S1813 analyte, when the simulation results tuned to the experimental data

## 8.12 Conclusion

In this section the use of the model as a biosensor was investigated. For this reason, the dielectric data for two RNA samples where extracted from the literature and their representatives were modelled in the simulation as dielectric blocks.

To explore the ability of the device to detect the RNA sample on its surface, a block of Poly-A ($30 * 15 * 0.5\ \mu^3 m$) was modelled on the top of X-structure. The model showed a shift in the frequency response and quality factor which is useful for detection purposes. Again the same simulation was done using Poly-C samples which showed the same frequency shift as Poly-A with a different quality factor.

Subsequently, to get a wider picture of how the size of the sample can affect the frequency response, Poly-A samples with different thicknesses and lengths were simulated.

The results showed that changing the thickness or length of the samples shifts the frequency response in a linear fashion for the specific analyte. These shifts can be predefined in the device. So, when the samples with different thicknesses and lengths are introduced to the device, the device would compare the result and match them to the predefined data. Or else, the binding of the analyte can be done in a way that the device accepts only certain length and thickness of the sample for the consistency of the analysis.

Next, the metamaterial samples with S1813 as the analyte were fabricated and their frequency response was measured using THz-TDS. The transmittance frequency response of the fabricated metamaterials with and without the photoresist analyte were compared. The frequency of resonance decreases by ~0.03THz, for all the metamaterials. This is the main factor of these metamaterials working as sensors by observing the shift in the resonance frequency, when an analyte is added to the sensor.

The results were also compared to the simulation, were for each metamaterial almost an equal shift of ~0.035 THz in the frequency of resonances was observed, which is tunable by decreasing the size of the modelled metamaterial by 3%, without compromising the quality factor. Also, the shape of the resonances and the quality factors between simulation and experimental results are similar. With the highest quality factor being 54.25 for the metamaterial type A.

# Chapter 9 Summary, Conclusion and Future work

## 9.1 Summary and Conclusion

In this study, a metamaterial-based sensor for sensing micro-scale biological samples is proposed. The metamaterial is made of inclusions with X-shaped resonators on a COC substrate. The metamaterial cells show a strong localization of the field and a high quality factor, in comparison to sensors with single resonators. This happens due to the inclusions being much smaller than the wavelength of the incident electromagnetic wave. Also compared to the metamaterials using split ring resonators for inclusions [18], the trapped-mode resonance is narrower, which results in more sensitivity to shifts in the resonant frequency.

This type of metamaterial can be engineered to act as a label-free sensor in different regions of the electromagnetic spectrum, owing to the tunability of metamaterials [96, 97]. However, for this study, as the analyte of interest was DNA and as DNA shows some natural frequencies in the THz region [5, 6, 85], THz was chosen for the region of operation.

Recent studies [17] show that by introducing asymmetry to the structure of the metamaterial inclusions, a trapped-mode resonance can be achieved, with a high quality factor.

In this study, for the metamaterial, to achieve a steeper resonance peak, asymmetry was introduced to the model. The asymmetry was achieved by creating two unequal sides to the X-resonator. This way, two antisymmetric currents are induced on the two unequal sides of the structure, being almost equal in amplitude and 180 degree out of phase. These currents produce two resonances close to one another on the frequency spectrum, giving rise to a steep trapped-mode resonance. By adding an analyte to the top of the resonators, the model is able to detect the shift in the frequency response and identify the analyte.

The primary X-resonator was modelled with $L_1$=180 μm, $L_2$=170 μm, α=80˚, d=5 μm and h=0.4 μm dimensions, where $L_{1\text{ and}}$ $L_2$ are the sizes of the two halves of the resonator, α is the separation angle between the arms of each half, d is the width of the arms and h is the thickness of the resonators (based on Figure 5-6).

To find the best composition and physical properties for the X-resonator and to produce the narrowest peak of resonance in the target frequency range, different compositions of the physical characteristics of the resonator were modelled. For this, different angles between the arms, different length of the arms, different width of the arms, different asymmetry sizes and different thickness of the arms of the resonators were modelled. The results showed that wider resonators produce steeper resonances. Also, resonators with larger degrees of asymmetry proved to result in

weaker trapped-mode resonances, due to the fact that the two resonances that contribute to the trapped-mode would occur further apart on the frequency spectrum.
From the outcome of these simulations, four different metamaterials with four different X-resonators as inclusions were picked for fabrication. For each X-resonator only one of the physical properties of the primary X-resonator was varied, to be able to quantify the simulation results through experimental data.

Next, for experimental purposes, different types of substrates were modelled underneath the metamaterial, to find the best fit. One of the challenging aspects of a metamaterial sensor functioning in THz region compared to optical ranges, is to find a suitable substrate, with low refractive index that would not attenuate the frequency response of the material. For this reason, different types of substrate materials, such as silicon, glass and polymer were simulated to find a substrate with the most transparency in THz.

Silicon has a high refractive index and absorption in THz region, so the frequency response of the simulated metamaterial on top of silicon was highly attenuated by the standing waves occurring due to the substrate. Same results were seen with quartz, but the nodes of the standing waves were further apart as the refractive index of quartz is much lower than silicon in THz. Lastly, the metamaterial was simulated on a COC substrate, which proved to be less interfering with the resonance response of the metamaterial owing to its low refractive index (~1.52) in THz.

As a result, COC being the most compatible substrate, for these metamaterials was chosen for fabrication. The metamaterial inclusions were fabricated on a 1 mm-thick COC substrate, which has a higher level of transparency in the THz region compared to silicon or silica substrates.

The frequency response of the fabricated metamaterials were measured using THz-TDS. The results from the fabricated metamaterials reflect a good match to the simulated models and show quality factors as high as ~50 for the trapped-mode resonance. In comparison to other label-free biosensors [17, 18], A higher quality factor is achieved with this model, which shows that this metamaterial has the possibility of achieving a higher sensitivity and selectivity as a sensor.

The experimental results agree with the simulation results for all four fabricated metamaterials in terms of quality factor of the trapped-mode resonance and the shape of the resonance. However an almost identical shift in the resonant frequency is seen among all the metamaterials, comparing the experimental and simulated data. This is due the discrepancy between the size of the fabricated and simulated resonators. As the shift is uniform in all the results, by shrinking the simulated model by 3%, the simulated data was tuned to the experimental data.

Lastly, to study the possibility of the structure to act as a sensor, two RNA blocks were simulated on top of the X-resonators. The results showed that the structure can distinguish between the two different analytes. Also, by varying the size and the thickness of the analyte, the resonant frequency shifted, which is an indication of the structure being sensitive to the amount of analyte used.

For fabrication, a 1 µm-thick layer of photoresist (S1813) was added uniformly on top of the X-resonators. Terahertz time domain spectroscopy, showed a distinct shift in the trapped-mode resonance, encouraging the ability of the structure to act as a sensor. There was a good match of the quality factor between the experimental and the simulated metamaterial with S1813. Again, there was a discrepancy between the resonant frequency of the experimental and simulated models, which was tuned by shrinking the simulated structure to 97% of its original size.

## 9.2 Future work

In this study, the possibility of producing a metamaterial that would exceed the sensing properties of the conventional sensors was explored. Both in the simulation and fabrication stages further studies can be done to expand the possibilities of these sensor and also improve their performance.

Some of these future possibilities are explained below.

### 9.2.1 Biosensing

At this stage, we successfully observed the ability of the fabricated metamaterials to act as a sensor. In future, we hope to achieve biosensing by adding DNA analyte to the metamaterial, to quantify the capability of the sensor in distinguishing between different types of DNA and identifying a certain one. Also, This study can be advanced for sensing other biological elements like proteins [98], which have several vibrational modes, located in the THz band.

Also, the effects of water content of DNA on the measurements should be studied. And if we opt for dehydrating the DNA sample, the change in the resonance frequency must be considered. *Markelz et al.* [7] studied the effects of water content of DNA on sensitivity. They confirm that absorbance increases linearly with frequency (agreeing with the *Beer-Lambert law*); however, the denatured DNA (with relative humidity of <5%) has lower transmission at lower frequencies.

Another future work for biosensing aspects of this work, would be to build a dielectric model for the biomolecules at THz, based on qualitative measurements, different concentrations, different bindings, etc. Also, it would be helpful to have models for the resonance of a single molecule, or several molecule aligned in a certain direction, for specific sensing purposes.

### 9.2.2 Ideal spectroscopy

A possible advancement to this study, is measuring the frequency response in a chamber with controlled humidity, temperature and pressure, being continuously purged with dry nitrogen gas. Humidity can alter the frequency response in THz-TDS. Studies [99] show intense transitions in water molecules in THz region, which results in attenuation on resonant peaks at specific frequencies. In comparison, nitrogen, shows no electric dipole moment, and does not absorb THz radiation.

This way the experimental results can be more reliable by ignoring the noise from varying environmental factors and the comparison between the simulated sensor and the fabricated sensor would be more direct.

Also, by using other types of THz-TDS (such as Z-omega time domain spectrometer) the reliability of the measured data can be quantified.

### 9.2.3 Scaling to other frequency ranges

As it was mentioned before, the inclusions of this metamaterial can be scaled to operate in different frequency regions to target analytes (either biological or non-biological) that have natural resonances in other parts of the electromagnetic spectrum. For instance, to detect the natural resonances of certain types of explosives [82, 100] or illegal drugs. This can be achieved by either downsizing or upsizing the size of the inclusions and periodicity to produce the trapped-mode resonance in different frequency regions.

### 9.2.4 Data fitting algorithm

In this study, the experimental results showed a difference in the resonant frequency compared to the simulated metamaterial. This difference is mainly due to the fabricated inclusions being 3% smaller than the simulated ones. As the difference was consistent and linear for all the models and because the materials were homogenous, the simulation results was tuned to the experimental results by uniformly shrinking the simulated metamaterial to 97% of its original size.

In future, an extensive study must be carried out, to see if this linearly tuning technique is always successful and possibly design a data fitting algorithm to fit all the problems.

### 9.2.5 Manufacturability

Fabrication of the metamaterial using substrates that are more common than COC can be explored in future, without compromising the quality factor and the steepness of the resonance. This way, a more degree of manufacturability in the long run will be achieved. A way to accomplish this was discussed in Chapter 5, by etching cuboids in the back of each inclusion and reducing the material overall permittivity of common substrates.

Also the binding agents for binding bio-analytes to the surface of the resonators should be explored and study on the implications of binding on the design and behaviour of the sensor must be carried out. Also, the effect of transferring the analyte sample on the whole surface of the sensor should be studied rather than patterning the analyte only on the resonators.

Furthermore, other possible resonant structures to further improve the sensitivity of the sensors and structures that will allow easy contact with the samples should be tested.

# Appendix A Q-factor of different parameters for X-resonator Configuration (Reflection)

| **Different degrees between each arms of X-resonator halves [deg]** | **$\Delta f$ (Bandwidth at 3dB ) [THz]** | **$f_0$(Peak of resonance) [THz]** | **Q-Factor** |
|---|---|---|---|
| 2_14 | _ | _ | _ |
| 16 | 0.0198 | 1.1316 | 57.1515 |
| 18 | 0.0198 | 1.0908 | 55.0909 |
| 20 | 0.0186 | 1.0548 | 56.7097 |
| 22 | 0.0180 | 1.035 | 57.5000 |
| 24 | 0.0168 | 1.011 | 60.1786 |
| 26 | 0.0162 | 0.996 | 61.4815 |
| 28 | 0.0156 | 0.9756 | 62.53846 |
| 30 | 0.0156 | 0.9624 | 61.6923 |
| 32 | 0.0144 | 0.9558 | 66.3750 |
| 34 | 0.0144 | 0.9462 | 65.7083 |
| 36 | 0.0138 | 0.9378 | 67.9565 |
| 38 | 0.0132 | 0.9288 | 70.3636 |
| 40 | 0.0132 | 0.9210 | 69.7727 |
| 42 | 0.0126 | 0.9144 | 72.5714 |

| | | | |
|---|---|---|---|
| 44 | 0.0126 | 0.9066 | 71.9524 |
| 46 | 0.0120 | 0.9012 | 75.0100 |
| 48 | 0.0120 | 0.8970 | 74.7500 |
| 50 | 0.0120 | 0.8898 | 74.1500 |
| 52 | 0.0114 | 0.8856 | 77.6842 |
| 54 | 0.0114 | 0.8814 | 77.3158 |
| 56 | 0.0114 | 0.8796 | 77.1579 |
| 58 | 0.0114 | 0.8748 | 76.7368 |
| 60 | 0.0114 | 0.8718 | 76.4737 |
| 62 | 0.0114 | 0.8682 | 76.15790 |
| 64 | 0.0114 | 0.8652 | 75.8947 |
| 66 | 0.0108 | 0.8622 | 79.8333 |
| 68 | 0.0108 | 0.8598 | 79.6111 |
| 70 | 0.0108 | 0.8574 | 79.3889 |
| 72 | 0.0108 | 0.8562 | 79.2778 |
| 74 | 0.0114 | 0.8556 | 75.0526 |
| 76 | 0.0114 | 0.8520 | 74.7368 |
| 78 | 0.0108 | 0.8538 | 79.0556 |
| 80 | 0.0108 | 0.8508 | 78.7778 |
| 82 | 0.0108 | 0.8514 | 78.8333 |
| 84 | 0.0114 | 0.8496 | 74.5263 |
| 86 | 0.0108 | 0.8490 | 78.6111 |
| 88 | 0.0114 | 0.8490 | 74.4737 |

| | | | |
|---|---|---|---|
| 90 | 0.0114 | 0.8490 | 74.4737 |
| 92 | 0.0120 | 0.8490 | 70.7500 |
| 94 | 0.0120 | 0.8496 | 70.8000 |
| 96 | 0.0120 | 0.8496 | 70.8000 |
| 98 | 0.0126 | 0.8508 | 67.5238 |
| 100 | 0.0126 | 0.8526 | 67.6667 |
| 102 | 0.0132 | 0.8514 | 64.5000 |
| 104 | 0.0132 | 0.8544 | 64.7273 |
| 106 | 0.0144 | 0.8562 | 59.4583 |
| 108 | 0.0138 | 0.8562 | 62.0435 |
| 110 | 0.0150 | 0.8580 | 57.2000 |
| 112 | 0.0168 | 0.8604 | 51.2143 |
| 114 | 0.0168 | 0.8622 | 51.3214 |
| 116 | 0.0192 | 0.8658 | 45.0938 |
| 118 | 0.0192 | 0.8688 | 45.2500 |
| 120 | 0.0210 | 0.8706 | 41.4571 |
| 122-179 | _ | _ | _ |

| **Difference between Length of halves (ΔL) [µm]** | **$\Delta f$ (Bandwidth at 3dB ) [THz]** | **$f_0$(Peak of resonance) [THz]** | **Q-Factor** |
|---|---|---|---|
| 2_6 | _ | _ | _ |
| 8 | 0.0126 | 0.8466 | 67.1905 |
| 10 | 0.0108 | 0.8508 | 78.7 |

| | | | |
|---|---|---|---|
| 12 | 0.0102 | 0.8574 | 84.0588 |
| 14 | 0.0102 | 0.864 | 84.7059 |
| 16 | 0.0102 | 0.87 | 85.2941 |
| 18 | 0.0102 | 0.8766 | 85.94118 |
| 20 | 0.0096 | 0.8838 | 92.0625 |
| 22 | 0.0102 | 0.8868 | 86.9412 |
| 24 | 0.0102 | 0.8958 | 87.8235 |
| 26 | 0.0102 | 0.903 | 88.5294 |
| 28 | 0.0102 | 0.9114 | 89.35297 |
| 30 | 0.0102 | 0.9174 | 89.9411 |
| 32 | 0.0102 | 0.9276 | 90.9412 |
| 34 | 0.0102 | 0.9342 | 91.5882 |
| 36 | 0.0108 | 0.9384 | 86.8889 |
| 38 | 0.0108 | 0.9486 | 87.8333 |
| 40 | 0.0108 | 0.957 | 88.6111 |
| 42 | 0.0114 | 0.9684 | 84.9474 |
| 44 | 0.0108 | 0.9798 | 90.72 |
| 46 | 0.0108 | 0.9906 | 91.72 |
| 48 | 0.0108 | 1.0008 | 92.7 |
| 50 | 0.0108 | 1.0134 | 93.83 |
| 52 | 0.0102 | 1.029 | 100.8824 |
| 54 | 0.0096 | 1.0452 | 108.875 |
| 56 | 0.0102 | 1.0584 | 103.7647 |

| | | | |
|---|---|---|---|
| 58 | 0.0102 | 1.071 | 105.0 |
| 60 | 0.0096 | 1.0848 | 113.0 |
| 62 | 0.0102 | 1.0992 | 107.7647 |
| 64 | 0.0096 | 1.1124 | 115.875 |
| 66 | 0.0096 | 1.1262 | 117.3125 |
| 68 | 0.0096 | 1.14 | 118.75 |
| 70 | 0.0102 | 1.1526 | 113.0 |
| 72 | 0.0096 | 1.1664 | 121.5 |
| 74 | 0.0096 | 1.1814 | 123.0625 |

| **Length of half of the X (L) [um]** | **$\Delta f$ (Bandwidth at 3dB ) [THz]** | **$f_0$(Peak of resonance) [THz]** | **Q-Factor** |
|---|---|---|---|
| 1_128 | – | – | – |
| 130 | 0.0114 | 1.1796 | 103.4737 |
| 132 | 0.0108 | 1.1634 | 107.72 |
| 134 | 0.0114 | 1.1466 | 100.5789 |
| 136 | 0.012 | 1.1298 | 94.15 |
| 138 | 0.0114 | 1.1148 | 97.78945 |
| 140 | 0.0126 | 1.0914 | 86.619 |
| 142 | 0.012 | 1.0782 | 89.85 |

| | | | |
|---|---|---|---|
| 144 | 0.012 | 1.0614 | 88.45 |
| 146 | 0.0114 | 1.053 | 92.3684 |
| 148 | 0.012 | 1.0326 | 86.05 |
| 150 | 0.0114 | 1.0254 | 89.9474 |
| 152 | 0.0114 | 1.0116 | 88.7368 |
| 154 | 0.0114 | 1.0002 | 87.7368 |
| 156 | 0.012 | 0.9858 | 82.15 |
| 158 | 0.0114 | 0.9732 | 85.3684 |
| 160 | 0.0114 | 0.96 | 84.2105 |
| 162 | 0.0114 | 0.9492 | 83.2632 |
| 164 | 0.0114 | 0.9372 | 82.2105 |
| 166 | 0.0114 | 0.9264 | 81.26316 |
| 168 | 0.0114 | 0.915 | 80.26316 |
| 170 | 0.0108 | 0.9048 | 83.78 |
| 172 | 0.0114 | 0.894 | 78.4211 |
| 174 | 0.0108 | 0.8832 | 81.78 |
| 176 | 0.0108 | 0.873 | 80.83 |
| 178 | 0.0114 | 0.8616 | 75.5789 |
| 180 | 0.0108 | 0.8508 | 78.78 |

| | | | |
|---|---|---|---|
| 182 | 0.0108 | 0.8412 | 77.9 |
| 184 | 0.0108 | 0.8328 | 77.1 |
| 186 | 0.0114 | 0.8214 | 72.05 |
| 188 | 0.0108 | 0.813 | 75.27 |
| 190 | 0.0108 | 0.804 | 74.4 |
| 192 | 0.0108 | 0.7938 | 73.5 |
| 194 | 0.0108 | 0.7842 | 72.61 |
| 196 | 0.0108 | 0.7752 | 71.7 |
| 198 | 0.0108 | 0.765 | 70.83 |
| 200 | 0.0114 | 0.7584 | 66.5263 |
| 202 | 0.0102 | 0.7494 | 73.4706 |
| 204 | 0.0114 | 0.741 | 65.0 |
| 206 | 0.0108 | 0.7344 | 68.0 |
| 208 | 0.0114 | 0.726 | 63.68420 |
| 210 | 0.0114 | 0.7182 | 63.0 |
| 212 | 0.0102 | 0.708 | 69.4118 |
| 214 | 0.0114 | 0.702 | 61.579 |
| 216 | 0.0108 | 0.696 | 64.4 |
| 218 | 0.0114 | 0.6888 | 60.4211 |

| | | | |
|---|---|---|---|
| 220 | 0.0108 | 0.6798 | 62.95 |
| 222 | 0.012 | 0.6738 | 56.15 |
| 224 | 0.0114 | 0.669 | 58.684 |
| 226 | 0.0126 | 0.66 | 52.381 |
| 228 | 0.0126 | 0.6546 | 51.9524 |
| 230 | 0.0120 | 0.6468 | 53.900 |
| 232 | 0.0126 | 0.6414 | 50.9048 |
| 234 | 0.0114 | 0.6348 | 55.68421 |
| 236 | 0.0120 | 0.6282 | 52.3500 |
| 238 | 0.0120 | 0.6228 | 51.900 |
| 240 | 0.0138 | 0.6156 | 44.6087 |
| 240> | – | – | – |

| **Width of the half of the X (D) [um]** | **$\Delta f$ (Bandwidth at 3dB ) [THz]** | **$f_0$(Peak of resonance) [THz]** | **Q-Factor** |
|---|---|---|---|
| 2 | 0.0174 | 0.8484 | 48.7586 |
| 3 | 0.0138 | 0.8526 | 61.7826 |
| 4 | 0.012 | 0.8556 | 71.3 |
| 5 | 0.0108 | 0.8574 | 79.39 |
| 6 | 0.0096 | 0.8586 | 89.4375 |

| | | | |
|---|---|---|---|
| 7 | 0.009 | 0.8598 | 95.53 |
| 8 | 0.0084 | 0.8622 | 102.643 |
| 9 | 0.0078 | 0.8634 | 110.69 |
| 10 | 0.0072 | 0.8646 | 120.083 |
| 11 | 0.0072 | 0.8658 | 120.25 |
| 12 | 0.0066 | 0.8676 | 131.455 |
| 13 | 0.006 | 0.8694 | 144.9 |
| 14 | 0.006 | 0.8706 | 145.1 |
| 15 | 0.006 | 0.8718 | 145.3 |
| 16 | 0.006 | 0.8736 | 145.6 |
| 17 | 0.0054 | 0.8748 | 162 |
| 18 | 0.006 | 0.8766 | 146.1 |
| 19 | 0.0054 | 0.8778 | 162.5 |
| 20 | 0.0054 | 0.8796 | 162.89 |
| 21 | 0.0054 | 0.881 | 163.1 |
| 22 | 0.0054 | 0.883 | 163.4 |
| 23 | 0.0048 | 0.8844 | 184.25 |
| 24 | 0.0048 | 0.8862 | 184.625 |
| 25 | 0.0048 | 0.888 | 185 |
| 26 | 0.0048 | 0.8898 | 185.375 |
| 27 | 0.0048 | 0.8916 | 185.75 |
| 28 | 0.0042 | 0.8934 | 212.7143 |
| 29 | 0.0042 | 0.8952 | 213.143 |
| 30 | 0.0042 | 0.897 | 213.57143 |
| 31 | 0.0048 | 0.8988 | 187.25 |
| 32 | 0.0048 | 0.9006 | 187.625 |

| | | | |
|---|---|---|---|
| 33 | 0.0042 | 0.903 | 215 |
| 34 | 0.0042 | 0.9054 | 215.572 |
| 35 | 0.0042 | 0.9072 | 216 |
| 36 | 0.0042 | 0.9096 | 216.57 |
| 37 | 0.0042 | 0.911 | 217 |
| 38 | 0.0042 | 0.9138 | 217.57 |
| 39 | 0.0042 | 0.9162 | 218.143 |
| 40 | 0.0042 | 0.9186 | 218.714 |
| 41 | 0.0042 | 0.9204 | 219.143 |
| 42 | 0.0042 | 0.9228 | 219.714 |
| 43 | 0.0042 | 0.9252 | 220.286 |
| 44 | 0.0042 | 0.9276 | 220.857 |
| 45 | 0.0042 | 0.93 | 221.4286 |
| 46 | 0.0042 | 0.9324 | 222 |
| 47 | 0.0042 | 0.9348 | 222.571 |
| 48 | 0.0042 | 0.9372 | 223.1429 |
| 49 | 0.0036 | 0.9396 | 261 |
| 50 | 0.0042 | 0.9426 | 224.4286 |
| 51 | 0.0042 | 0.945 | 225 |
| 52 | 0.0042 | 0.948 | 225.7143 |
| 53 | 0.0036 | 0.9504 | 264 |
| 54 | 0.0036 | 0.9528 | 264.66 |
| 55 | 0.0036 | 0.9558 | 265.45 |
| 56 | 0.0036 | 0.9588 | 266.33 |
| 57 | 0.0036 | 0.9612 | 267 |
| 58 | 0.0036 | 0.9642 | 267.833 |

| | | | |
|---|---|---|---|
| 59 | 0.0042 | 0.9696 | 230.857 |
| 60 | 0.0042 | 0.9726 | 231.57 |
| 62 | 0.0042 | 0.9786 | 233 |
| 64 | 0.0042 | 0.9846 | 234.4286 |
| 66 | 0.0042 | 0.99 | 235.7143 |
| 68 | 0.0042 | 0.9966 | 237.2857 |
| 70 | 0.0042 | 1.0032 | 238.857 |
| 72 | 0.0024 | 1.0068 | 419.5 |
| 74 | 0.0042 | 1.0164 | 242 |
| 76 | 0.0042 | 1.0236 | 243.7143 |
| 78 | 0.0042 | 1.0302 | 245.286 |
| 80 | 0.0042 | 1.0374 | 247 |
| 82 | 0.0048 | 1.0446 | 217.625 |
| 84 | 0.0048 | 1.0524 | 219.25 |
| 86 | 0.0054 | 1.059 | 196.1 |
| 88 | 0.0054 | 1.0662 | 197.5 |
| 90 | 0.006 | 1.074 | 179 |
| 92 | 0.0066 | 1.0818 | 163.91 |
| 94 | 0.0072 | 1.089 | 151.25 |
| 96 | 0.0072 | 1.0968 | 152.33 |
| 98 | 0.0084 | 1.1046 | 131.5 |
| 100 | 0.0114 | 1.1118 | 97.526 |
| 102 | 0.0132 | 1.1196 | 84.818 |
| 104 | 0.0192 | 1.1274 | 58.7187 |
| 106 | 0.0342 | 1.1352 | 33.193 |

| **Thickness of the X (h) [um]** | **$\Delta f$ (Bandwidth at 3dB ) [THz]** | **$f_0$(Peak of resonance) [THz]** | **Q-Factor** |
|---|---|---|---|
| 0.01 | 0.0132 | 0.846 | 64.1 |
| 0.06 | 0.0132 | 0.849 | 64.3182 |
| 0.11 | 0.0126 | 0.8502 | 67.4762 |
| 0.16 | 0.012 | 0.849 | 70.75 |
| 0.21 | 0.012 | 0.852 | 71 |
| 0.26 | 0.0114 | 0.8514 | 74.6842 |
| 0.31 | 0.0114 | 0.849 | 74.4737 |
| 0.36 | 0.0108 | 0.8514 | 78.83 |
| 0.41 | 0.0108 | 0.8526 | 78.95 |
| 0.46 | 0.0108 | 0.8526 | 78.95 |
| 0.51 | 0.0102 | 0.852 | 83.5294 |
| 0.02 | 0.0138 | 0.846 | 61.3043 |
| 0.03 | 0.0126 | 0.8472 | 67.2381 |
| 0.04 | 0.0132 | 0.8466 | 64.13636 |
| 0.05 | 0.0132 | 0.8496 | 64.3636 |
| 0.07 | 0.0126 | 0.8472 | 67.2381 |
| 0.08 | 0.012 | 0.8496 | 67.4286 |
| 0.09 | 0.012 | 0.8478 | 70.65 |
| 0.1 | 0.012 | 0.8496 | 70.8 |
| 0.12 | 0.0132 | 0.8496 | 64.3636 |
| 0.13 | 0.012 | 0.849 | 70.75 |
| 0.14 | 0.0126 | 0.8502 | 67.476 |
| 0.15 | 0.012 | 0.8496 | 70.8 |

| | | | |
|---|---|---|---|
| 0.17 | 0.012 | 0.8502 | 70.85 |
| 0.18 | 0.0126 | 0.8502 | 67.4762 |
| 0.19 | 0.012 | 0.8502 | 70.85 |
| 0.2 | 0.012 | 0.8502 | 70.85 |
| 0.22 | 0.0114 | 0.8496 | 74.5263 |
| 0.23 | 0.012 | 0.8496 | 70.8 |
| 0.24 | 0.0114 | 0.8508 | 74.6316 |
| 0.25 | 0.0114 | 0.8496 | 74.5263 |
| 0.27 | 0.0114 | 0.8514 | 74.6842 |
| 0.28 | 0.0114 | 0.852 | 74.7368 |
| 0.29 | 0.0114 | 0.8514 | 74.6842 |
| 0.3 | 0.0114 | 0.8508 | 74.6316 |
| 0.32 | 0.0114 | 0.852 | 74.73684 |
| 0.33 | 0.0108 | 0.8514 | 78.83 |
| 0.34 | 0.0114 | 0.8526 | 74.78947 |
| 0.35 | 0.0108 | 0.8508 | 78.7 |
| 0.37 | 0.0108 | 0.8526 | 78.94 |
| 0.38 | 0.0108 | 0.8514 | 78.83 |
| 0.39 | 0.0108 | 0.852 | 78.8 |
| 0.4 | 0.0114 | 0.852 | 74.7368 |
| 0.42 | 0.0114 | 0.8496 | 74.5263 |
| 0.43 | 0.0108 | 0.8526 | 78.94 |
| 0.44 | 0.0102 | 0.8508 | 83.4118 |
| 0.45 | 0.0108 | 0.8508 | 78.7 |
| 0.47 | 0.0108 | 0.852 | 78.8 |
| 0.48 | 0.0108 | 0.8508 | 78.77 |

| | | | |
|---|---|---|---|
| 0.49 | 0.0108 | 0.8526 | 78.94 |
| 0.5 | 0.0102 | 0.8526 | 83.5882 |

# Bibliography

[1] J. Li, and Y. Huang, *Time-domain finite element methods for Maxwell's equations in metamaterials*: Springer Science & Business Media, 2012.

[2] B. D. Malhotra, and A. Turner, *Advances in biosensors: Perspectives in biosensors*: Elsevier, 2003.

[3] M. Brucherseifer, M. Nagel, P. H. Bolivar, H. Kurz, A. Bosserhoff, and R. Büttner, "Label-free probing of the binding state of DNA by time-domain terahertz sensing," *Applied Physics Letters,* vol. 77, no. 24, pp. 4049-4051, 2000.

[4] M. Chee, R. Yang, E. Hubbell, A. Berno, X. C. Huang, D. Stern, J. Winkler, D. J. Lockhart, M. S. Morris, and S. P. A. Fodor, "Accessing Genetic Information with High-Density DNA Arrays," *Science,* vol. 274, no. 5287, pp. 610-614, October 25, 1996, 1996.

[5] L. Van Zandt, and V. Saxena, "Millimeter-microwave spectrum of DNA: six predictions for spectroscopy," *Physical Review A,* vol. 39, no. 5, pp. 2672, 1989.

[6] W. Zhuang, Y. Feng, and E. Prohofsky, "Self-consistent calculation of localized DNA vibrational properties at a double-helix–single-strand junction with anharmonic potential," *Physical Review A,* vol. 41, no. 12, pp. 7033, 1990.

[7] A. G. Markelz, A. Roitberg, and E. J. Heilweil, "Pulsed terahertz spectroscopy of DNA, bovine serum albumin and collagen between 0.1 and 2.0 THz," *Chemical Physics Letters,* vol. 320, no. 1–2, pp. 42-48, 3/31/, 2000.

[8] H.-J. Lee, and J.-G. Yook, "Biosensing using split-ring resonators at microwave regime," *Applied Physics Letters,* vol. 92, no. 25, pp. 254103-254103-3, 2008.

[9] S. RoyChoudhury, V. Rawat, A. H. Jalal, S. Kale, and S. Bhansali, "Recent advances in metamaterial split-ring-resonator circuits as biosensors and therapeutic agents," *Biosensors and Bioelectronics,* vol. 86, pp. 595-608, 2016.

[10] B. Lahiri, A. Z. Khokhar, M. Richard, S. G. McMeekin, and N. P. Johnson, "Asymmetric split ring resonators for optical sensing of organic materials," *Optics express,* vol. 17, no. 2, pp. 1107-1115, 2009.

[11] W. Xu, L. Xie, and Y. Ying, "Mechanisms and applications of terahertz metamaterial sensing: a review," *Nanoscale,* vol. 9, no. 37, pp. 13864-13878, 2017.

[12] C. Debus, and P. H. Bolívar, "Terahertz biosensors based on double split ring arrays." p. 69870U.

[13] C. Debus, and P. H. Bolivar, "Frequency selective surfaces for high sensitivity terahertz sensing," *Applied Physics Letters,* vol. 91, no. 18, pp. 184102, 2007.

[14] S. Park, S. Cha, G. Shin, and Y. Ahn, "Sensing viruses using terahertz nano-gap metamaterials," *Biomedical optics express,* vol. 8, no. 8, pp. 3551-3558, 2017.

[15] S. Park, J. Hong, S. Choi, H. Kim, W. Park, S. Han, J. Park, S. Lee, D. Kim, and Y. Ahn, "Detection of microorganisms using terahertz metamaterials," *Scientific reports,* vol. 4, pp. 4988, 2014.

[16] M. Nagel, M. Först, and H. Kurz, "THz biosensing devices: fundamentals and technology," *Journal of Physics: Condensed Matter,* vol. 18, no. 18, pp. S601, 2006.

[17] V. Fedotov, M. Rose, S. Prosvirnin, N. Papasimakis, and N. Zheludev, “Sharp trapped-mode resonances in planar metamaterials with a broken structural symmetry,” *Physical review letters,* vol. 99, no. 14, pp. 147401, 2007.

[18] B. Lahiri, “Split ring resonator (srr) based metamaterials,” University of Glasgow, 2010.

[19] S. J. Park, and Y. H. Ahn, “Accurate Measurement of THz Dielectric Constant Using Metamaterials on a Quartz Substrate,” *Current Optics and Photonics,* vol. 1, no. 6, pp. 637-641, 2017.

[20] M. D. Rotaru, and J. K. Sykulski, “Improved Sensitivity of Terahertz Label Free Bio-Sensing Application Through Trapped-Mode Resonances in Planar Resonators,” *Magnetics, IEEE Transactions on,* vol. 47, no. 5, pp. 1026-1029, 2011.

[21] W. R. Heineman, and W. B. Jensen, “Leland C. Clark Jr. (1918–2005),” *Biosensors and Bioelectronics,* vol. 21, no. 8, pp. 1403-1404, 2/15/, 2006.

[22] E. N. Marieb, *Essentials of human anatomy & physiology*, 10th ed. ed., Boston, [Mass.]

London: Benjamin Cummings, 2012.

[23] i. The McGraw-Hill Companies. "DNA structure," http://www.mhhe.com/biosci/esp/2001_gbio/folder_structure/ge/m4/s1/.

[24] R. R. Sinden, *DNA structure and function*: Elsevier, 2012.

[25] B. Fischer, M. Hoffmann, H. Helm, G. Modjesch, and P. U. Jepsen, “Chemical recognition in terahertz time-domain spectroscopy and imaging,” *Semiconductor Science and Technology,* vol. 20, no. 7, pp. S246, 2005.

[26] J. F. Federici, B. Schulkin, F. Huang, D. Gary, R. Barat, F. Oliveira, and D. Zimdars, “THz imaging and sensing for security applications—explosives, weapons and drugs,” *Semiconductor Science and Technology,* vol. 20, no. 7, pp. S266, 2005.

[27] T. Chen, S. Li, and H. Sun, “Metamaterials Application in Sensing,” *Sensors (Basel, Switzerland),* vol. 12, no. 3, pp. 2742-2765,

, 2012.

[28] D. L. Woolard, W. R. Loerop, and M. Shur, *Terahertz Sensing Technology: Emerging scientific applications and novel device concepts*: World Scientific, 2003.

[29] M. Brucherseifer, M. Nagel, P. Haring Bolivar, H. Kurz, A. Bosserhoff, and R. Büttner, “Label-free probing of the binding state of DNA by time-domain terahertz sensing,” *Applied Physics Letters,* vol. 77, no. 24, pp. 4049-4051, 2000.

[30] P. H. Bolívar, M. Nagel, F. Richter, M. Brucherseifer, H. Kurz, A. Bosserhoff, and R. Büttner, “Label–free THz sensing of genetic sequences: towards ‘THz biochips’,” *Philosophical Transactions of the Royal Society of London A: Mathematical, Physical and Engineering Sciences,* vol. 362, no. 1815, pp. 323-335, 2004.

[31] J. N. Anker, W. P. Hall, O. Lyandres, N. C. Shah, J. Zhao, and R. P. Van Duyne, “Biosensing with plasmonic nanosensors,” *Nature materials,* vol. 7, no. 6, pp. 442-453, 2008.

[32] M. Nagel, P. H. Bolivar, M. Brucherseifer, H. Kurz, A. Bosserhoff, and R. Büttner, “Integrated THz technology for label-free genetic diagnostics,” *Applied Physics Letters,* vol. 80, no. 1, pp. 154-156, 2002.

[33] Z. Jakšić, S. Vuković, J. Matovic, and D. Tanasković, "Negative refractive index metasurfaces for enhanced biosensing," *Materials,* vol. 4, no. 1, pp. 1-36, 2010.

[34] H. Tao, A. C. Strikwerda, M. Liu, J. P. Mondia, E. Ekmekci, K. Fan, D. L. Kaplan, W. J. Padilla, X. Zhang, R. D. Averitt, and F. G. Omenetto, "Performance enhancement of terahertz metamaterials on ultrathin substrates for sensing applications," *Applied Physics Letters,* vol. 97, no. 26, pp. -, 2010.

[35] K.-S. Lee, and M. A. El-Sayed, "Gold and silver nanoparticles in sensing and imaging: sensitivity of plasmon response to size, shape, and metal composition," *The Journal of Physical Chemistry B,* vol. 110, no. 39, pp. 19220-19225, 2006.

[36] J. C. Bose, "On the rotation of plane of polarisation of electric waves by a twisted structure," *Proceedings of the Royal Society of London,* vol. 63, no. 389-400, pp. 146-152, 1898.

[37] N. Engheta, and R. W. Ziolkowski, *Metamaterials: physics and engineering explorations*: Wiley. com, 2006.

[38] W. E. Kock, "Metallic delay lenses," *Bell System Technical Journal,* vol. 27, no. 1, pp. 58-82, 1948.

[39] W. S. Weiglhofer, and A. Lakhtakia, *Introduction to complex mediums for optics and electromagnetics*: SPIE press, 2003.

[40] T. J. Cui, D. R. Smith, and R. Liu, *Metamaterials: theory, design, and applications*: Springer, 2010.

[41] N. I. Zheludev, "The road ahead for metamaterials," *Science,* vol. 328, no. 5978, pp. 582-583, 2010.

[42] J. B. Pendry, D. Schurig, and D. R. Smith, "Controlling electromagnetic fields," *Science,* vol. 312, no. 5781, pp. 1780-1782, 2006.

[43] H. Kind, H. Yan, B. Messer, M. Law, and P. Yang, "Nanowire ultraviolet photodetectors and optical switches," *Advanced Materials,* vol. 14, no. 2, pp. 158, 2002.

[44] Q. Bai, C. Liu, J. Chen, C. Cheng, M. Kang, and H.-T. Wang, "Tunable slow light in semiconductor metamaterial in a broad terahertz regime," *Journal of Applied Physics,* vol. 107, no. 9, pp. 093104, 2010.

[45] M. Wuttig, and N. Yamada, "Phase-change materials for rewriteable data storage," *Nature materials,* vol. 6, no. 11, pp. 824-832, 2007.

[46] W. Cai, U. K. Chettiar, A. V. Kildishev, and V. M. Shalaev, "Optical cloaking with metamaterials," *Nature photonics,* vol. 1, no. 4, pp. 224-227, 2007.

[47] F. Wang, H. Liu, T. Li, Z. Dong, S. Zhu, and X. Zhang, "Metamaterial of rod pairs standing on gold plate and its negative refraction property in the far-infrared frequency regime," *Physical Review E,* vol. 75, no. 1, pp. 016604, 2007.

[48] U. Leonhardt, "Optical metamaterials: Invisibility cup," *Nature Photonics,* vol. 1, no. 4, pp. 207-208, 2007.

[49] D. R. Smith, and J. B. Pendry, "Homogenization of metamaterials by field averaging," *JOSA B,* vol. 23, no. 3, pp. 391-403, 2006.

[50] W. Hansen, and R. Richtmyer, "On resonators suitable for klystron oscillators," *Journal of Applied Physics,* vol. 10, no. 3, pp. 189-199, 1939.

[51] W. Hardy, and L. Whitehead, “Split‐ring resonator for use in magnetic resonance from 200–2000 MHz,” *Review of Scientific Instruments,* vol. 52, no. 2, pp. 213-216, 1981.

[52] J. B. Pendry, A. J. Holden, D. Robbins, and W. Stewart, “Magnetism from conductors and enhanced nonlinear phenomena,” *Microwave Theory and Techniques, IEEE Transactions on,* vol. 47, no. 11, pp. 2075-2084, 1999.

[53] D. R. Smith, W. J. Padilla, D. Vier, S. C. Nemat-Nasser, and S. Schultz, “Composite medium with simultaneously negative permeability and permittivity,” *Physical review letters,* vol. 84, no. 18, pp. 4184, 2000.

[54] L. Solymar, and E. Shamonina, *Waves in metamaterials*: Oxford University Press, 2009.

[55] R. Marqués, F. Medina, and R. Rafii-El-Idrissi, “Role of bianisotropy in negative permeability and left-handed metamaterials,” *Physical Review B,* vol. 65, no. 14, pp. 144440, 2002.

[56] M. Durán-Sindreu, J. Naqui, F. Paredes, J. Bonache, and F. Martín, “Electrically small resonators for planar metamaterial, microwave circuit and antenna design: A comparative analysis,” *Applied Sciences,* vol. 2, no. 2, pp. 375-395, 2012.

[57] A. Alu, and N. Engheta, “Dielectric sensing in ϵ-near-zero narrow waveguide channels,” *Physical Review B,* vol. 78, no. 4, pp. 045102, 2008.

[58] M. Huang, and J. Yang, “Microwave sensor using metamaterials,” *Wave Propagation*, pp. 13-36, 2011.

[59] N. Papasimakis, Z. Luo, Z. X. Shen, F. De Angelis, E. Di Fabrizio, A. E. Nikolaenko, and N. I. Zheludev, “Graphene in a photonic metamaterial,” *Optics express,* vol. 18, no. 8, pp. 8353-8359, 2010.

[60] X. C. Zhang, and J. Xu, *Introduction to THz Wave Photonics*, 2010.

[61] T.-J. Yen, W. Padilla, N. Fang, D. Vier, D. Smith, J. Pendry, D. Basov, and X. Zhang, “Terahertz magnetic response from artificial materials,” *Science,* vol. 303, no. 5663, pp. 1494-1496, 2004.

[62] H. Yoshida, Y. Ogawa, Y. Kawai, S. Hayashi, A. Hayashi, C. Otani, E. Kato, F. Miyamaru, and K. Kawase, “Terahertz sensing method for protein detection using a thin metallic mesh,” *Applied physics letters,* vol. 91, no. 25, pp. 253901, 2007.

[63] C. M. Bingham, H. Tao, X. Liu, R. D. Averitt, X. Zhang, and W. J. Padilla, “Planar wallpaper group metamaterials for novel terahertz applications,” *Optics Express,* vol. 16, no. 23, pp. 18565-18575, 2008.

[64] T. Hasebe, S. Kawabe, H. Matsui, and H. Tabata, “Metallic mesh-based terahertz biosensing of single-and double-stranded DNA,” *Journal of Applied Physics,* vol. 112, no. 9, pp. 094702, 2012.

[65] S. Park, B. Son, S. Choi, H. Kim, and Y. Ahn, “Sensitive detection of yeast using terahertz slot antennas,” *Optics Express,* vol. 22, no. 25, pp. 30467-30472, 2014.

[66] S. Park, S. Jun, A. Kim, and Y. Ahn, “Terahertz metamaterial sensing on polystyrene microbeads: shape dependence,” *Optical materials express,* vol. 5, no. 10, pp. 2150-2155, 2015.

[67] C. Zhang, L. Liang, L. Ding, B. Jin, Y. Hou, C. Li, L. Jiang, W. Liu, W. Hu, and Y. Lu, “Label-free measurements on cell apoptosis using a terahertz metamaterial-based biosensor,” *Applied Physics Letters,* vol. 108, no. 24, pp. 241105, 2016.

[68] T. Hasebe, Y. Yamada, and H. Tabata, "Label-free THz sensing of living body-related molecular binding using a metallic mesh," *Biochemical and biophysical research communications,* vol. 414, no. 1, pp. 192-198, 2011.

[69] H. Tao, L. R. Chieffo, M. A. Brenckle, S. M. Siebert, M. Liu, A. C. Strikwerda, K. Fan, D. L. Kaplan, X. Zhang, R. D. Averitt, and F. G. Omenetto, "Metamaterials on Paper as a Sensing Platform," *Advanced Materials,* vol. 23, no. 28, pp. 3197-3201, 2011.

[70] W. Wang, F. Yan, S. Tan, H. Zhou, and Y. Hou, "Ultrasensitive terahertz metamaterial sensor based on vertical split ring resonators," *Photonics Research,* vol. 5, no. 6, pp. 571-577, 2017.

[71] T. Rylander, P. Ingelström, and A. Bondeson, *Computational electromagnetics*: Springer Science & Business Media, 2012.

[72] C. M. STUDIO®, "CST MICROWAVE STUDIO," 2015.

[73] D. M. Pozar, *Microwave engineering*: John Wiley & Sons, 2009.

[74] R. Yadava, *Antenna and wave propagation*: PHI Learning Pvt. Ltd., 2011.

[75] J. Yuan, *Numerical Simulation of Hysteresis Effects in Ferromagnetic Material with the Finite Integration Technique*: Cuvillier Verlag, 2005.

[76] G. Ciuprina, and D. Ioan, *Scientific Computing in Electrical Engineering*: Springer Science & Business Media, 2007.

[77] Y. Hao, and R. Mittra, *FDTD modeling of metamaterials: Theory and applications*: Artech house, 2008.

[78] P. Drude, "Zur elektronentheorie der metalle," *Annalen der Physik,* vol. 306, no. 3, pp. 566-613, 1900.

[79] H. A. Lorentz, *Le mouvement des électrons dans les métaux*, 1905.

[80] F. Cardarelli, *Materials handbook: a concise desktop reference*: Springer, 2008.

[81] H. Yasuda, and I. Hosako, "Measurement of terahertz refractive index of metal with terahertz time-domain spectroscopy," *Japanese Journal of Applied Physics,* vol. 47, no. 3R, pp. 1632, 2008.

[82] M. Koch, "Terahertz communications: A 2020 vision," *Terahertz Frequency Detection and Identification of Materials and Objects*, pp. 325-338: Springer, 2007.

[83] S. L. Dexheimer, *Terahertz spectroscopy: principles and applications*: CRC press, 2007.

[84] A. L. Chung, "Material parameter extraction in terahertz time domain spectroscopy," University of Southampton, 2012.

[85] A. Markelz, A. Roitberg, and E. J. Heilweil, "Pulsed terahertz spectroscopy of DNA, bovine serum albumin and collagen between 0.1 and 2.0 THz," *Chemical Physics Letters,* vol. 320, no. 1, pp. 42-48, 2000.

[86] P. A. Laplante, *Comprehensive dictionary of electrical engineering*: CRC Press, 2005.

[87] D. C. Harris, *Materials for infrared windows and domes: properties and performance*: SPIE press, 1999.

[88] Mi-Net. "

Silicon Wafers," 30/11/2015, 2015; http://www.mi-net.co.uk/Semiconductor-Materials/silicon-wafers.php.

[89] Tydex. "

Quartz Glass for Optics," 10/August/2015; http://www.tydexoptics.com/pdf/Quartz_glass.pdf.

[90] W. Wang, and S. A. Soper, *Bio-MEMS: technologies and applications*: CRC press, 2006.

[91] P. D. Cunningham, N. N. Valdes, F. A. Vallejo, L. M. Hayden, B. Polishak, X.-H. Zhou, J. Luo, A. K.-Y. Jen, J. C. Williams, and R. J. Twieg, "Broadband terahertz characterization of the refractive index and absorption of some important polymeric and organic electro-optic materials," *Journal of Applied Physics,* vol. 109, no. 4, pp. 043505-043505-5, 2011.

[92] I. Maestrojuan, I. Palacios, I. Ederra, and R. Gonzalo, "Use of low loss substrate for developing sub-millimeter-wave mixers." pp. 2650-2652.

[93] S. Franssila, *Introduction to microfabrication*: John Wiley & Sons, 2010.

[94] N. Papasimakis, V. A. Fedotov, Y. H. Fu, D. P. Tsai, and N. I. Zheludev, "Coherent and incoherent metamaterials and order-disorder transitions," *Physical Review B,* vol. 80, no. 4, pp. 041102, 2009.

[95] B. Fischer, M. Hoffmann, H. Helm, R. Wilk, F. Rutz, T. Kleine-Ostmann, M. Koch, and P. Jepsen, "Terahertz time-domain spectroscopy and imaging of artificial RNA," *Optics Express,* vol. 13, no. 14, pp. 5205-5215, 2005/07/11, 2005.

[96] S. Linden, C. Enkrich, M. Wegener, J. Zhou, T. Koschny, and C. M. Soukoulis, "Magnetic response of metamaterials at 100 terahertz," *Science,* vol. 306, no. 5700, pp. 1351-1353, 2004.

[97] V. M. Shalaev, "Optical negative-index metamaterials," *Nature photonics,* vol. 1, no. 1, pp. 41, 2007.

[98] A. Lawrence, J. McDaniel, D. Chang, and R. Birge, "The nature of phonons and solitary waves in alpha-helical proteins," *Biophysical journal,* vol. 51, no. 5, pp. 785-793, 1987.

[99] A. Danylov, "THz laboratory measurements of atmospheric absorption between 6% and 52% relative humidity," *Submillimeter-Wave Technology Laboratory University of Massachusetts Lowell,* vol. 175, 2006.

[100] Y. Shen, T. Lo, P. Taday, B. Cole, W. Tribe, and M. Kemp, "Detection and identification of explosives using terahertz pulsed spectroscopic imaging," *Applied Physics Letters,* vol. 86, no. 24, pp. 241116, 2005.